Development of Impact Localisation and Force Reconstruction Structural Health Monitoring techniques for Aerospace components

De Simone, Mario Emanuele

Award date:
2019

Awarding institution:
University of Bath

Development of Impact Localisation and Force Reconstruction Structural Health Monitoring techniques for Aerospace components

De Simone, Mario Emanuele

Award date:
2019

Awarding institution:
University of Bath

Development of Impact Localisation and Force Reconstruction Structural Health Monitoring techniques for Aerospace components

Mario Emanuele De Simone

Department of Mechanical Engineering

University of Bath

Thesis submitted for the degree of
Doctor of Philosophy

September 2019

Copyright

To my special family, Antonella, Armando and Rosa, that with immense love always supported me

To my lovely and precious fiancée Rita, my life and future

In loving memory of my grandparents, watching over me from above

"Three Rules of Work:

1. Out of clutter find simplicity
2. From discord find harmony
3. In the middle of difficulty lies opportunity."

Albert Einstein (1879 – 1955), Physicist & Nobel Laureate

Acknowledgements

This thesis work represents the “final chapter” of one of the greatest experiences in my life, indeed it coincides also with the conclusion of three wonderful years spent in Bath. Despite the work difficulties, I was lucky to find an entire team of amazing people that helped me to move on not only in the research field, but in life with their support and friendship.

First of all, I would like to express my gratitude to Prof. Michele Meo, superb guidance in my academic path, for the encouragements and suggestions he furnished me, for his willingness and for the confidence he has always had in my person. I am sure that what I learned from him will be fundamental in future.

I am truly grateful toward my supervisors and friends, Francesco Ciampa and Fulvio Pinto, able to support me in each moment with their experience and competence. I owe so many small and big achievements to them, included this thesis work. Moreover, it is important to highlight the true honour that to continue the Francesco’s academic research represented for me.

A special acknowledgement is for the numerous persons that contributed to the realisation of this work, with their skills and friendship. They are not just colleagues, neither simply friends, but my second family; I am talking about my “brothers” Fabrizio and Salvatore, then Francesco Rizzo, Francesco Flora, Marco, Mario, Gian Piero, Christos. A special good luck is for my friend Stefano Cuomo, that was able to start his PhD continuing my research work with great passion and sacrifice.

In addition, I would also like to thank other friends with which I spent amazing moments during my PhD period in Bath, as Mattia and Anna, Milena, Erika, Davide, Andrea, Tommaso, Enrico, Francesca, Becky, Antonietta, Yanexy, Sara.

It is impossible to not remember all the people and teachers whose lessons formed and furnished me, as man, student and engineer before PhD, at high school "Emilio Segrè" (Professors Romano and Fabbricatore inter alios), military school "Nunziatella" (Professors Russo, Ranucci, de Simone, Giusti and Grifoni inter alios and the Army Officers Zampa, Pisapia and Bertazzo), University of Naples "FedericoII" (it is not possible to remember all the incredible Professors I met), Thales Alenia Space (Drs. Campolo, Catastini and Menzione) and MBDA (Drs. Pizzingrilli and Capoleoni).

I am truly grateful to my extraordinary family, my parents, Antonella and Armando, and my sister Rosa, for their constant support and love not only during my time life in Bath but during all my life. I am sure I would not have been able to complete my PhD without their confidence, concern and strength, despite the huge difficulties due to the absence and distance among us.

I am also grateful to my other family members who have supported me along the way, that are my uncles Giuliano, Lucrezia, Mariapia and Domenico, my cousins Vittorio, Cristina, Michele and Gabriele, my grandmothers Cristina and Rosa, my grandfathers Michele e Mario, my in-laws Luigi and Annamaria and my brother-in-law Paolo.

A great thank is for all the friends and people that during my life, and especially during PhD period, always encouraged me, despite of the distance. Among all, I would like to say thank you to Raffaele Di Leva, Dario Abete, Marco Cappa, Caterina Caianiello, Enzo Adaldo, Carlo Fruttaldo, Mario Agliata, Gaetano Agliata, Maurizio Arena, Annachiara Loffredo, Federico Cavaliere, Mauro Zarrelli, Mario Hubler, Marco Currao, Vincenzo Tescione, Gianfrancesco De Vita, Domenico Alvino, Costanza Caianiello and Father Giovanni.

My gratitude is also for Domenico Lanzo, the President of Netcom Group, the amazing company in Naples where I started to work after the conclusion of my PhD

period in Bath, for the regard and the confidence he always demonstrated for me and my work.
Lastly, but not least, I would like to thank my lovely fiancée Rita, my huge love, my strength, my future wife, certainly one of the most important and precious people in my life. The sacrifices we sustained for three years are well-known, but our immense love gave us the strength and the patience for overcoming the difficulties we encountered on the way. The only wish I have is that the love between us will increase for the rest of our lives, together and forever.

A sincere thank you to everyone, from the depths of my heart!

Mariuele

Abstract

Over the last decade, acoustic emission localisation has become an important tool for structural health monitoring and non-destructive inspection applications, particularly for the aerospace field. Acoustic source localisation consists of identifying in space and time the source of acoustic waves, by recording the propagating acoustic signals using several receiving sensors. In this work, the impact between a foreign object and a component was considered as the source of acoustic emissions.

The main topic of this thesis was, therefore, the creation of structural health monitoring systems for the localisation of impact events and the reconstruction of impact loads on both isotropic and composite aerospace components. Innovative acoustic emission identification methods and algorithms were here developed and presented. These include: (i) the linearisation of the nonlinear system of equations for the localisation of impact events, (ii) the creation of a new signal power algorithm for impact localisation, (iii) the development of a novel ultrasonic data interpolation algorithm by using hierarchical radial basis functions and (iv) the creation of the first impact load reconstruction algorithm using time reversal, which does not require prior information of the mechanical properties of the host component. Furthermore, some of the presented techniques were also combined in order to provide a proof of concept for the estimation of direction and velocity of space debris by using a small composite detector.

The proposed algorithms and methods were validated by performing experimental tests on different metallic and composite aerospace structures, as plates and real wings. The considered structural components were arranged with different typologies and configurations of acoustic emission transducers, either fixed to the specimen surface or embedded into the structure. These tests demonstrated that results were achieved with a high level of accuracy, identified by a negligible difference (often less than 2-3%) between true and calculated values/functions. Therefore, the proposed structural health monitoring algorithms presented in this research work have the potential to provide a reliable and sensitive tool for the in-service inspection of aerospace components.

Contents

List of Figures

Chapter 1. Introduction

Chapter 2. Background on impact localisation

Chapter 3. Linearised impact localisation method

List of Tables

Chapter 1

Introduction

1.1 Structural Health Monitoring Systems

Structural health monitoring (SHM) aims to give, at every moment during the component lifetime, a diagnosis of the "state" of the constituent materials, of different parts, and of the full assembly of these parts constituting the structure as a whole [1]. Emphasising its "diagnostic" function, SHM can be considered not only as a mean to make acoustic/ultrasonic non-destructive testing and evaluation (NDT&E) methods applicable for in-service use, but also as a process able to determine the design and the full management of a structure, interpreted as an isolated system or as a part of a wider system, thanks to integration of sensors, smart material and data transmission. The organisation of a typical SHM system is reported in Figure 1. A damaged sample is the monitored structure under investigation and a set of sensors are deputed to send and collected signals containing information, able to determine the diagnosis (SHM), the prognosis (evolution of damage, residual life, etc.) and the health management of the structure (organisation of maintenance, repair operations, etc.). Supposing the monitored structure as a part of a more complex system, it could be possible to achieve the health management of the full system as the last step.

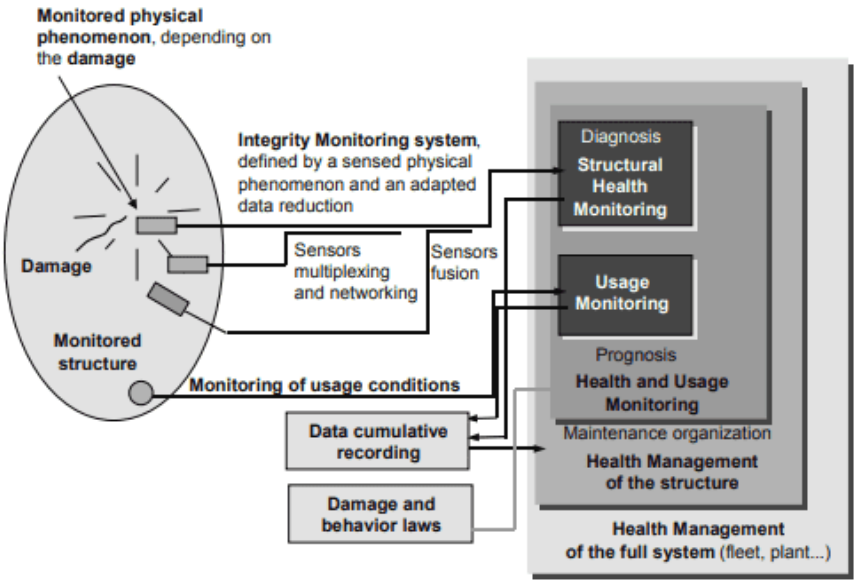

Figure 1. Principle and organisation of a SHM system, from [1].

Recently, advanced composite structures have been widely used in aerospace and civil applications due to their desirable characteristics such as high strength, stiffness and low weight [2]. In order for composite materials to be used more extensively in aircraft structures, they have to be maintained in a safe and economical manner by a rapid scanning of large areas without removal of individual components. As reported in [1], the use of smart monitoring systems on a modern fighter aircraft featuring both metal and composite structure can lead to a saving of more than 40% on the total inspection time. This concept is showed in Table 1.

Table 1. Estimated time saved on inspection operations by the use of SHM, from [1].

Inspection type	Current inspection time (% of total)	Estimated potential for smart systems	Time saved (% of total)
Flight line	16	0.40	6.5
Scheduled	31	0.45	14.0
Unscheduled	16	0.10	1.5
Service instructions	37	0.60	22.0
	100		44.0

The safety of a structure can be assured by a constant structural monitoring able to determine not only the presence of a damage, but also the cause generating it. In the case of composite structures, the most commonly encountered type of damage is caused by low-velocity impacts due to foreign objects, such as hailstones, dropped tools, runway debris during take-off and landing, bird strikes, etc. An extensive damage (Figure 2a) can be easily localised and it is possible to act instantly, whilst a barely visible damage, such as sub-surface delamination, matrix cracking, fibre debonding or fracture, etc. (Figure 2b), caused by the reported impact events could be very dangerous if not immediately identified, because it may lead to a significant reduction of the structure's strength and fatigue life.

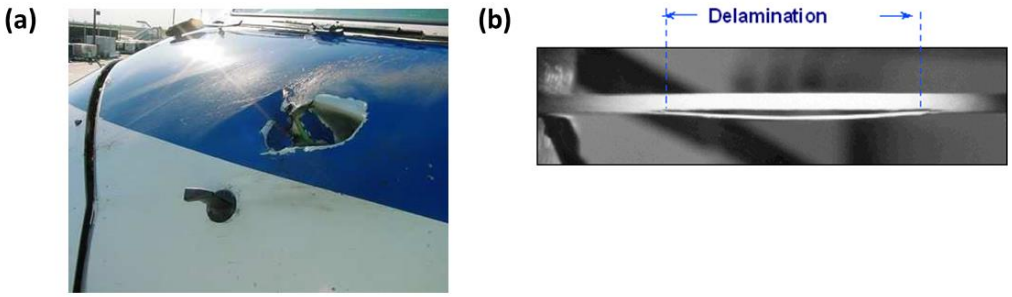

Figure 2. Example of: extensive impact damage (a) and barely visible damage (b).

For this reason, in the last decades numerous SHM and NDE techniques have been developed for the localisation of low-velocity impacts in metallic and composite components (Figure 3). From a physical point of view, an impact can be considered as an "acoustic source" (the same is for crack formation and structural element failure), because the peculiar characteristic of impact events is the generation of acoustic waves. Therefore, it is possible to refer to them as "acoustic emission (AE) sources". In this research work, the "impact" is the acoustic source of interest (Figure 4).

Figure 3. Examples of SHM and NDE techniques applications in aerospace field.

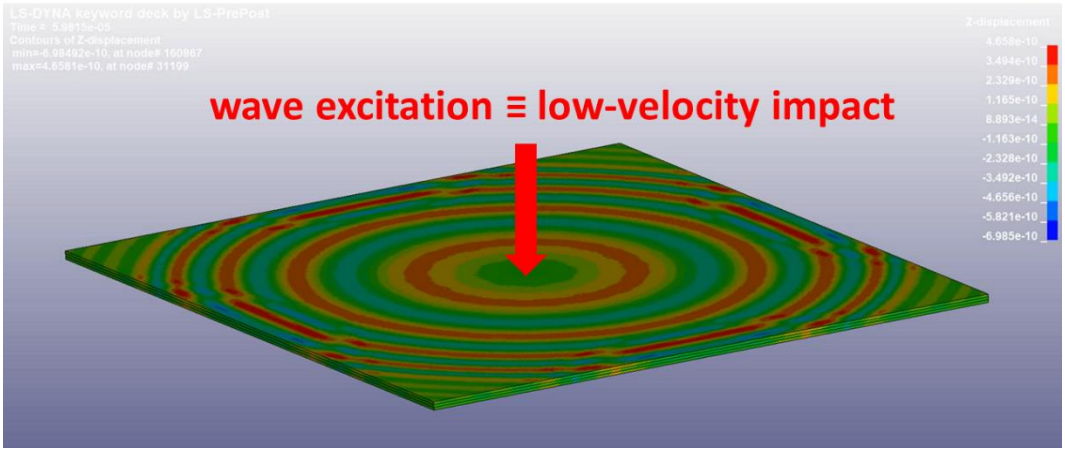

Figure 4. Low-velocity impact identified as an acoustic emission source.

1.2 Objectives and overview

The principal aim of the present research work is to show the developed SHM techniques, suitable for both metallic and composite components, able to furnish the real-time knowledge of two fundamental features:

- the localisation of the impact event;
- the determination of the impact load.

The first crucial information consists of the identification of the spatial coordinates of the impact event, while the second one can be obtained by reconstructing the shape of the impact force history in time domain.

It should be underlined that components and materials typically used in the aerospace field are considered in this work, consisting largely of aluminium or carbon fibre reinforced plastic (CFRP) composite thin plates or real and complex aeronautical structures, such as wing stringer-skin panels.

Three methods able to achieve the localisation of an impact event are investigated in this research works:

- the linearised algorithm;
- the time reversal method;
- the signal power method.

In all these methods one or an array of piezoelectric receiving transducers, fixed to the specimen surface or embedded into the structure, are employed for the detection of the acoustic waves generated by the impact, then producing an electric signal recoded by a PC. These are the characteristics of the "passive SHM techniques".

The main difference between these methods and the so-called "active SHM techniques", generally used to detect and evaluate damages, is that in the second approach the acoustic waves are generated by an actuator transducer integrated on the structure. It should be noted that this research work does not consider the "active SHM techniques", described in detail in [3].

The first localisation method considered in this thesis is able to determine the impact coordinates with reasonable accuracy (maximum error in the estimation of the impact location coordinates less than 6 mm), by using an optimal configuration of only four closely spaced surface-bonded piezoelectric transducers, without a-priori knowledge of the mechanical properties of the material. The localisation algorithm is based on:

- the time of arrival estimation of the elastic waves generated by the impact source using Akaike information criterion (AIC);
- the linearisation of the well-known nonlinear system of equations for the estimation of the impact location.

The second localisation method is based on the time reversal approach, which is able to determine the impact location by a cross-correlation between a set of stored structural responses due to an initial impact calibration process, and the impulsive response due to the unknown impact event. The obtained results confirm that time reversal is one of the most accurate localisation methods, with a maximum location error less than 3 mm.

The third approach provides the impact localisation on a generic composite plate, embedded with a sparse array of embedded piezo-transducers, without a-priori knowledge of the mechanical properties nor the speed of propagating waves. In the presented condition, none of the previous methods is suitable, indeed transducers are far away for using the linearised impact localisation algorithm and no baseline is provided for the application of the time reversal method.

The method is able to furnish the impact coordinates thanks to the calculation of signal power of the recorded signals by the transducers and a radial basis function (RBF) interpolation approach.

As aforementioned, another principal topic of this thesis consists of reconstructing the impact force in the time domain, which is achieved downstream of the time reversal method. Indeed, the data obtained during the calibration process (impact histories and structural responses) and the calculated impact coordinates are the inputs of the impact force reconstruction algorithm. In this new approach, a suitable interpolation technique based on the hierarchical radial basis functions (RBFs) is used to identify the transfer function at the impact location and the impact force by the knowledge of the structural response.

A final topic of this research work consisted of monitoring the space debris by the calculation of their direction and speed, by using a device named SCODD (“Smart Composite Orbital Debris Detector”) and developed by the author. In a space environment different types of impacts should be considered, commonly referred

as “hypervelocity impacts”, where the speeds of impacting debris are typically around 7-10 km/s. In our case, the feature behaviour, subjected to low-velocity impacts, represents only a proof of concept for future hypervelocity tests.
The detector consists of two thin parallel CFRP composite plates, instrumented with a set of piezoelectric sensors. Time reversal for the impact localisation and time of arrival estimation by using AIC were involved in the algorithm. The wave velocity calibration process for both the plates was also performed.
It should be highlighted that all the algorithms developed for the described methods and approaches were implemented by using MATLAB [4] programming language.

1.3 Outline of the Thesis

The outline of the thesis is the following: in Chapter 2 a detailed literature review is presented, where a number of research work related to the thesis arguments are described, while from Chapter 3 to Chapter 7 the thesis topics will be exposed in a number of published papers. Each publication is introduced by a brief description, in which the motivation, the summary and the results of the paper topics are summarised.
In Chapter 3 the impact localisation method based on the time of arrival estimation by using Akaike information criterion (AIC) and the linearisation of the classical nonlinear system of equations is presented. The method is suitable for both isotropic and composite components and its accuracy is highlighted by the results (maximum location error small than 6 mm).
Chapter 4 describes the different impact localisation method based on the time reversal method. In this case an initial calibration process is necessary, furthermore for the reconstruction of the impact load in time domain. An interpolation method based on the radial basis functions (RBFs) and a suitable method for the calculation of the structural transfer functions are developed and applied in order to achieve a negligible difference (less than 2% in performed experimental tests) between the actual impact time histories and the reconstructed ones.

In Chapter 5, the time reversal and the impact force reconstruction are applied on a complex aeronautical structure (a composite wing stringer-skin panel). Moreover, two impactors with different hardness, a steel and a rubber one, impacting the sample with unknown energy levels, were investigated in the experimental tests. In the paper it is demonstrated that also in these conditions the algorithm is able to furnish a good localisation of the impact event and an accurate reconstruction of the impact force.

Chapter 6 concerns the description of the "Smart Composite Orbital Debris Detector", a feature able to detect the direction and the velocity of space debris. Numerous methods analysed in the previous publications are used in this chapter, as the Akaike information criterion and the time reversal.

Chapter 7 presents the signal power impact localisation method, suitable for composite components when the previous techniques are not applicable. The algorithm is based on the signal power calculation of the recorded signals due to the impact and the radial basis functions, also in this case fundamental for the interpolation of sparse known information.

The conclusions of the thesis, with some future works ideas and a summary of the PhD activities are reported in Chapter 8.

Chapter 2

Background on impact localisation

In this Chapter, an overview on some research works present in literature and related to the principal topic of the thesis, that is the impact localisation, will be presented.

The information reported in this section can be integrated with the Introduction sections of the publications inserted in the next Chapters, in order to have a wider and more detailed idea about the arguments, including their advantages and limitations.

2.1 Acoustic emission source localisation

Several studies concerning the detection and location of an acoustic emission (AE) source are present in literature [5], many of them based on the triangulation technique, also known as “Tobias algorithm” [6], wherein the impact point is identified as the intersection of three circumferences, whose centres are the sensor locations (Figure 1). This method can be used for isotropic and homogeneous structures, because it is necessary to know accurately the wave velocity.

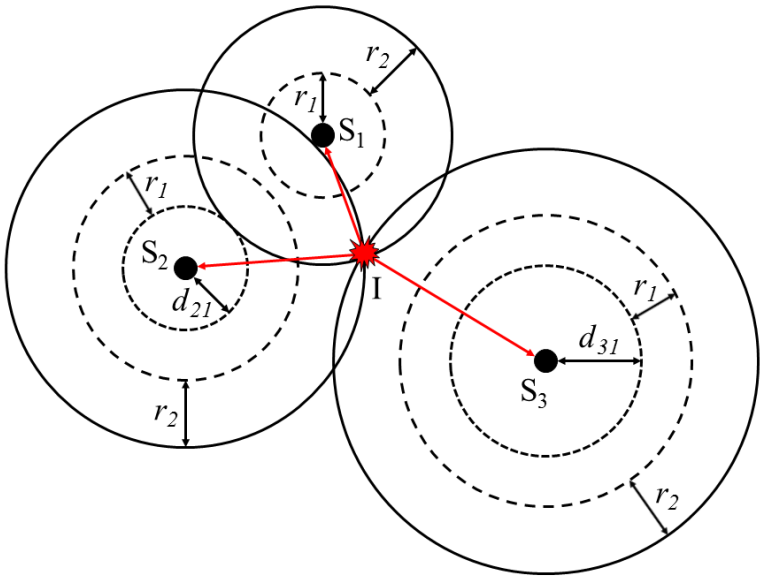

Figure 1. Triangulation technique. Three sensors placed at positions 1, 2 and 3 receive the acoustic waves generated by the source at position I. Radius of each circle corresponds to the distance travelled by the wave from the source to the sensor.

Another approach based on the assumption that wave velocity is constant in all directions is the beamforming technique, introduced by McLaskey et al. [7] and used by He et al. [8]. This method is based on the using of a small array of sensors (from four to eight sensing elements) and on the delay-and-sum algorithm. In Figure 2 there are four transducers, receiving acoustic signals generated by an impact.

Considering $\vec{r}$ as the distance of a reference point, called "focal point", from the first sensor, indicated as S_1, it is possible to define the individual time delay $\Delta_i(\vec{r})$ for the i^{th} sensor as:

$$\Delta_i(\vec{r}) = \frac{|\vec{r}| - |\vec{r} - \vec{r}_i|}{c}, \tag{1}$$

where c indicates the wave propagation velocity.

The N recorded signals generate the array $b(\vec{r}, t)$, after applying time delays $\Delta_i(\vec{r})$ to the recorded signals and multiplying them with the weight factor w_i as shown below:

$$b(\vec{r},t) = \frac{1}{N}\sum_{i=1}^{N} w_i\, x_i\big(t - \Delta_i(\vec{r})\big)\,, \qquad (2)$$

where $x_i(t)$ is the signal acquired by the i^{th} transducer.

When the focal point and the impact coincide, the delay-and-sum algorithm of Eq. (2) gives the maximum value of b. In this case, the recorded signals are added in phase and all weight factors w_i can be taken as 1. The principal advantage of beamforming technique is that the exact time of arrival of a specific wave mode is not necessary, so it is possible to consider Gaussian white noisy signals too.

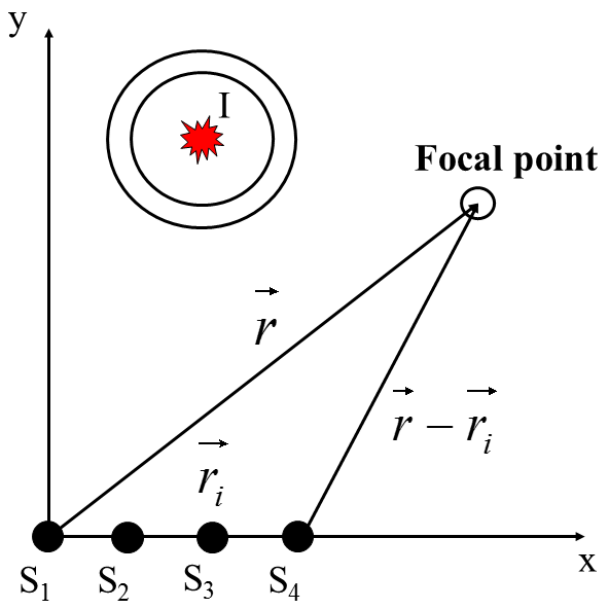

Figure 2. Visualisation of the beamforming technique. The b parameter (Eq. (2)) is maximum when the focal point coincides with the impact point.

The strong limitation of the two described methods is that they are suitable only for isotropic or quasi-isotropic media, in which the wave velocity is known and remains the same in all directions. The basic equation for the impact model in isotropic case is:

$$d_i = \sqrt{(x_i - x_I)^2 + (y_i - y_I)^2} = c\, t_i\,, \qquad i = 1, \ldots, N\,, \qquad (3)$$

where d_i is the distance between the i^{th} receiving sensor, whose Cartesian coordinates on the sample surface are (x_i, y_i), and the impact source, whose Cartesian coordinates on the sample surface are (x_I, y_I), c is the propagation velocity of the stress wave reaching the i^{th} transducer, t_i are the times of detection of the acoustic emission signals, N represents the number of receivers.

Several approaches were developed for isotropic plates with unknown wave velocity, such as a different triangulation technique [9], where a system of nonlinear equations must be solved to locate the acoustic source. It is called "triangulation" only because three sensors that form a triangle are necessary.

The previous hypothesis about wave velocity in isotropic specimen cannot be respected if anisotropic and inhomogeneous materials are considered, as well as for dispersive guided waves in which the wave velocity is not constant, but it is a function of the frequency.

The basic equation for the impact model in anisotropic case is:

$$d_i = \sqrt{(x_i - x_I)^2 + (y_i - y_I)^2} = c(\theta_i)\, t_i\,, \qquad i = 1, \dots, N\,, \tag{4}$$

where the propagation velocity is dependent on propagation direction/angle, represented by θ.

Kundu et al. [10, 11] developed an approach in which the wave velocity is unknown and it is not necessary to solve a system of nonlinear equations, suitable for isotropic and anisotropic plates. They presented a general formulation for source localisation in anisotropic plates, based on the minimisation of an error function, or "objective function". The algorithm is able to determine three unknowns, the mentioned coordinates of the impact event and the wave velocity, by using four sensors.

Meo et al. [12] investigated the use of an impact detection algorithm to locate a potentially damaging impact on an orthotropic plate by detecting the stress waves generated by such an event. The proposed localisation algorithm was developed by Salehian [13] and involved only three sensors. Differently from isotropic material, the changing values of the wave velocity due to the propagation direction needed to be taken into account. It was evaluated in an initial calculation process. Two

equations with only two variables, representing two of the three θ angles reported in Figure 3, were the results of the impact localisation algorithm.

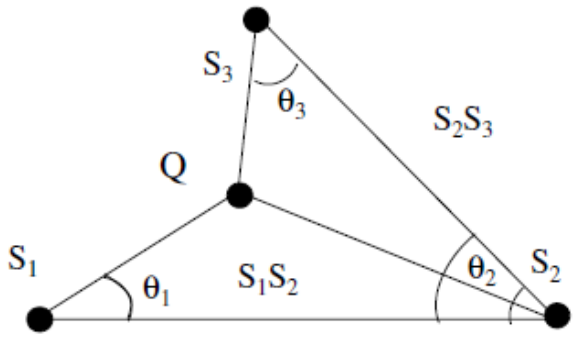

Figure 3. Visualisation of the Meo and Salehian technique for the impact localisation with three acoustic sensors on an orthotropic plate, from [12] and [13].

The mentioned techniques for anisotropic structures are limited by the knowledge of the direction dependent profile in the anisotropic plate for source localisation. Kundu et al. [14, 15] developed a particular approach where it is possible to localise an acoustic source in an anisotropic plate by using only six receiving sensors without knowing velocity information and without solving a system of nonlinear equations (Figure 4). The technique was verified also for plates made of isotropic material (requiring four sensors). Acoustic source can be localised from the intersection point of two direction lines generated by two clusters of sensors by solving a system of two linear equations with the two impact coordinates as unknowns. A third cluster can be used to investigate if the third direction line also goes through the intersection point of the other two lines to reconfirm the prediction.

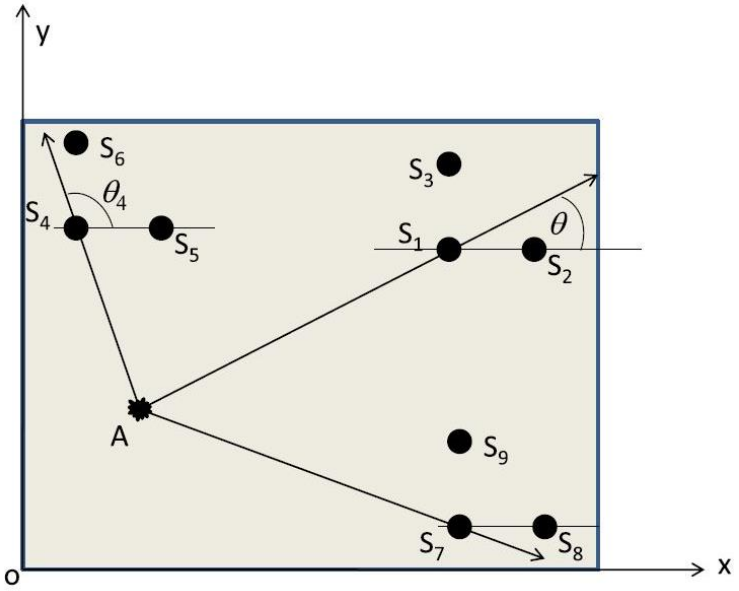

Figure 4. Visualisation of the Kundu technique for the impact localisation with three sets of acoustic sensors on a plate, from [15].

Ciampa and Meo developed an algorithm for the impact source localisation in their works on aluminium [16], anisotropic [17] and composite [18] structures.

In [16] it is possible to consider a plate with dimensions L, length, and W, width, with the origin of the Cartesian reference frame at its left bottom corner, and four receiving sensors in the plane of the plate $x - y$, as shown in Figure 5. The impact source point is indicated with I, at unknown coordinates (x_I, y_I). The four transducers are located at distance d_i $(i = 1, \dots, 4)$ from the source.

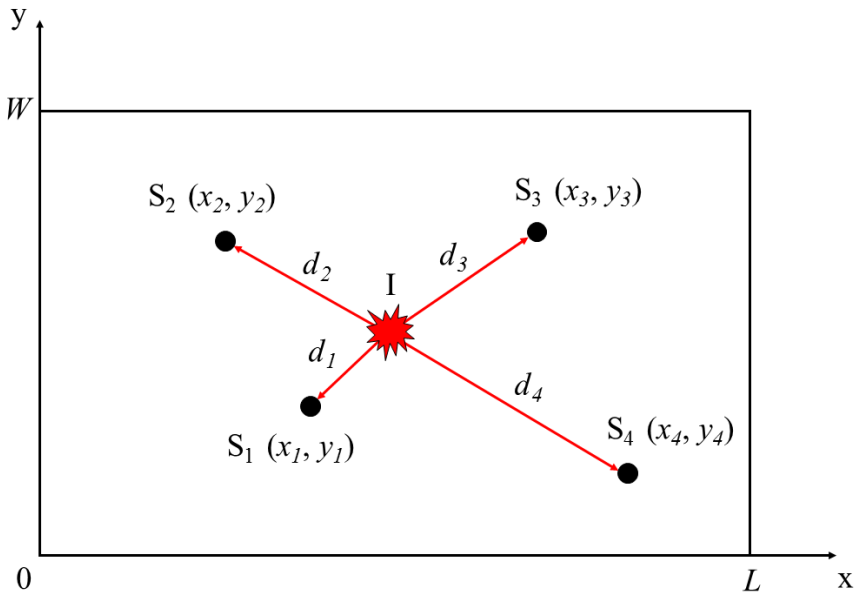

Figure 5. Sensor arrangement in Ciampa's work [16].

The coordinates of the impact source can be determined by solving the following general system of nonlinear equations [16]:

$$\begin{cases} \|d_i\|^2 = (x_i - x_I)^2 + (y_i - y_I)^2 \\ t_i = \dfrac{\|d_i\|}{V_g} \end{cases}, \qquad i = 1, \dots, 4\,, \tag{5}$$

where V_g is the unique but unknown wave speed, t_i are the times of detection of the AE signals and (x_i, y_i) are the coordinates of the i^{th} sensor.

Combining both terms of (5) it is possible to obtain four equations in the form of (3):

$$(x_i - x_I)^2 + (y_i - y_I)^2 - \left(t_i V_g\right)^2 = 0\,, \qquad i = 1, \dots, 4\,, \tag{6}$$

which represent the equations of four circumferences with radius ${r_i}^2 = \left(t_i\, V_g\right)^2$.

Considering one of the sensor as "reference sensor" (e.g. the sensor 1) it is possible to relate the travel time required to reach this sensor, t_{ref}, and the time differences of arrival between other sensors and the reference one, $\Delta t_{ref,j}$, obtaining an expression for the time of arrival concerning the j^{th}, sensor:

$$t_j = t_{ref} \pm \Delta t_{ref,j}\,, \qquad j = 2, \dots, 4\,. \tag{7}$$

Substituting (7) into (6), system (6) becomes:

$$\begin{cases} \left(x_j - x_I\right)^2 + \left(y_j - y_I\right)^2 = \left[\left(t_1 \pm \Delta t_{1,j}\right) V_g\right]^2 \\ \left(x_1 - x_I\right)^2 + \left(y_1 - y_I\right)^2 = \left(t_1\, V_g\right)^2 \end{cases}. \tag{8}$$

$$j = 2, \dots, 4$$

System (8) consists of four nonlinear equations for four unknowns, $x_I,\ y_I,\ t_1,\ V_g$. Numerous research works present in literature offer methods and algorithms able to furnish the time differences of arrival (TDOAs), that are the three $\Delta t_{1,j}$ reported in system (8) for our case. Ziola et al. [19], Kosel et al. [20] and Kundu et al. [14, 15] used the cross-correlation technique, in order to calculate directly the TDOAs, whilst Ciampa et al. [16] calculated the TDOAs as simple differences between the time of arrivals of the signals, obtained by using the magnitude of the squared modulus of continuous Wavelet transform (CWT), described also in Section 2.2. The system (8) is then solved by using a combination of both local (Newton's) and global (unconstrained optimisation) methods.

A similar approach for the impact localisation was developed by Ciampa and Meo for anisotropic [17] and composite [18] specimens. The used sensor arrangement is shown in Figure 6 and the motivation for this particular configuration with six receiving sensors will be explained as follows.

Because of an anisotropic/composite plate is considered, system (8) is modified according to Eq. (3):

$$\begin{cases} \left(x_j - x_I\right)^2 + \left(y_j - y_I\right)^2 = \left[\left(t_1 \pm \Delta t_{1,j}\right) V_{g,j}\right]^2 \\ \left(x_1 - x_I\right)^2 + \left(y_1 - y_I\right)^2 = \left(t_1\, V_{g,1}\right)^2 \end{cases}. \tag{9}$$

$$j = 2, \dots, 6$$

System (9) consists of six nonlinear equations for nine unknowns, $x_I,\ y_I,\ t_1,\ V_{g,j}$, and cannot be solved yet since the number of variables is still bigger than the number of equations. To overcome this issue, an optimal sensor configuration is

necessary to solve the system of equations. The sensors are located so that each pair of transducers is relatively close together (Figure 6), in order to experience the same propagation velocity. It is:

$$\begin{aligned} V_{g,1}(\theta) &\approx V_{g,2}(\theta) \\ V_{g,3}(\theta) &\approx V_{g,4}(\theta) \\ V_{g,5}(\theta) &\approx V_{g,6}(\theta) \end{aligned} . \tag{10}$$

Thereby, system (9) can be rewritten as:

$$\begin{cases} (x_j - x_I)^2 + (y_j - y_I)^2 = \left[(t_1 \pm \Delta t_{1,j})\, V_{g,k}\right]^2 \\ (x_1 - x_I)^2 + (y_1 - y_I)^2 = \left(t_1\, V_{g,1}\right)^2 \end{cases} . \tag{11}$$

$$j = 2, \ldots, 6, \qquad k = 1, 3, 5$$

System (11) consists of six nonlinear equations for six unknowns, x_I, y_I, t_1, $V_{g,1}$, $V_{g,3}$, $V_{g,5}$ and it is solved by using the same methods applied in [16].

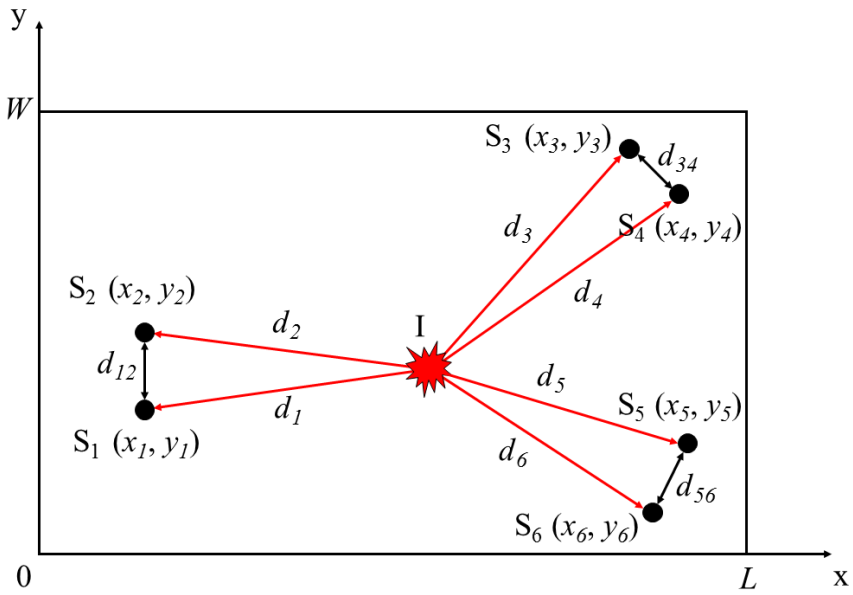

Figure 6. Sensor arrangement in Ciampa's works [17] and [18].

A completely different impact localisation approach is based on the time reversal method and it was applied on aeronautic components by Ciampa et al. in several

research works [21-23]. A detailed description of this method is present also in Chapter 4 and Chapter 5 of this thesis.

2.2 Time of arrival estimation

The principal purpose of this dissertation is to develop an algorithm able to provide the impact coordinates on an aerospace component, without knowing the material properties of the structure.

Some impact localisation approaches require an accurate estimation of the time differences of arrivals (TDOAs) in order to obtain precise values for impact coordinates. The TDOAs calculation could be based on time of arrivals (TOAs) of the acquired signals, so it is crucial to use a method to estimate accurately the TOAs of the signals.

The time of arrival, or "onset time" of transient signals, like acoustic emissions, seismograms or ultrasound signals, can be described as the moment when the first energy of a particular phase arrives at a sensor (phase means e.g. longitudinal, transversal or Lamb wave) and it is usually picked as the point where the first difference between the signal and the noise takes place (see Figure 7).

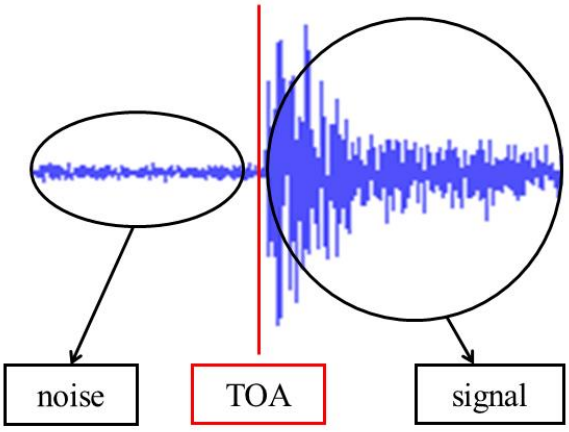

Figure 7. Time of arrival (TOA) visualisation in a signal.

In the past, several approaches were used for automatic TOA estimation, many of them modified from seismology, due to similarity between seismology and acoustic fields.

The simplest method is to use an amplitude threshold picker, where the onset time is determined as the time corresponding a signal value immediately before the signal amplitude exceeds a particular threshold value. A first approach in seismology could be find in [24].

To overcome the limitation of this method (small amplitude signals and/or presence of high noise level), a huge number of algorithms were developed and applied in different fields on totally different specimens. Some of these methods are cited in the Introduction section of the publication reported in Chapter 3.

As aforementioned, Ciampa and Meo used the continuous Wavelet transform (CWT) in their research works [16-18].

The CWT is a linear transform that correlates the harmonic waveform $u(x,t)$ with basic functions consisting in dilatations and translation of a mother wavelet $\psi(t)$, by the continuous convolution of the signal and the scaled or shifted wavelet [25]:

$$WT(x,a,b) = \frac{1}{\sqrt{a}} \int_{-\infty}^{+\infty} u(x,t)\, \psi^*\left(\frac{t-b}{a}\right) dt\,, \tag{12}$$

where $\psi^*(t)$ denotes the complex conjugate of the mother wavelet $\psi(t)$, a is the dilatation or scale parameter defining the support width of the wavelet and b is the translation parameter localising the wavelet in time domain. AE localisation in isotropic and anisotropic structure involved different mother wavelets; in [16-18] the complex Morlet wavelet was employed as it is able to separate amplitude and phase, enabling the measurement of instantaneous frequencies and their temporal evolution. It is expressed by the following equation [26]:

$$\psi(t) = \frac{1}{\sqrt{\pi\, F_b}}\, e^{j\omega_c t}\, e^{-\frac{t^2}{F_b}} = \frac{1}{\sqrt{\pi\, F_b}}\, e^{-\frac{t^2}{F_b}} \left[cos(\omega_c t) + j\ sin(\omega_c t)\right], \tag{13}$$

where $f_c = \omega_c/2\pi$ is the "central frequency" and F_b is the "shape control parameter" (wavelet bandwidth).

The squared modulus of the CWT, also called a "scalogram", indicates the energy density of the signal at each scale at any time, hence, it is able to reveal the highest local energy content of the waveform $u(x,t)$ measured from each transducer. The scalogram can be expressed as:

$$|WT(x,a,b)|^2 = WT(x,a,b) \cdot WT^*(x,a,b)\,. \tag{14}$$

It can be demonstrated that the maximum value of the scalogram coefficients, obtained at the angular frequency of interest ω_0, allows identifying the TOA of the group velocity (Figure 8).

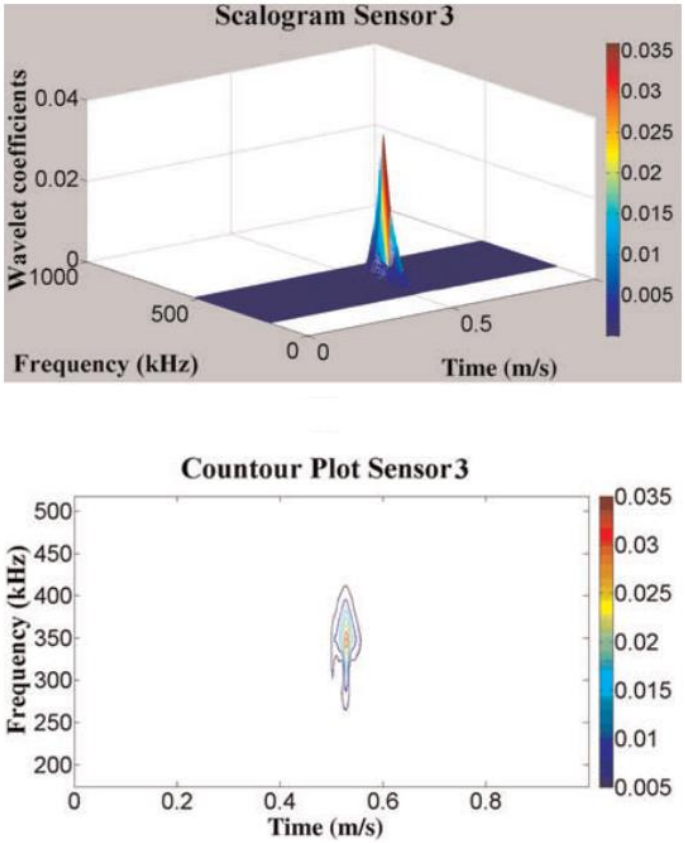

Figure 8. 3D plot (top) of the wavelet scalogram coefficients and associated contour plot (bottom), from [18].

In this dissertation, a different approach for TOA estimation, based on the Akaike Information Criterion (AIC), is used. Several AIC picker algorithms are described in detail in publication reported in Chapter 3.

Chapter 3

Linearised impact localisation method

The principal goal of the publication presented in this Chapter is to overcome the limitations of impact localisation algorithms briefly illustrated in Chapter 2, e.g. the real time knowledge of the mechanical properties of the material, so the propagating wave speed due to a low-velocity impact.

When a structure is not isotropic and homogeneous, techniques as the triangulation "Tobias algorithm" [6] cannot be applicable, and other algorithms are suitable only if the direction dependence of the wave velocity is known [10-13].

There are cases where impact coordinates are calculated with high accuracy (in terms of negligible difference, meaning less than 5 mm, between actual and calculated impact coordinates) in anisotropic [17] and composite [18] structures without a-priori knowledge of wave speed, nevertheless the used approaches lead some mathematical difficulties, as the solving of a nonlinear system of equations by a combination of both local (Newton's) and global (unconstrained optimisation) methods.

In the proposed research work, the developed method achieves the localisation of an impact event in isotropic and not strongly inhomogeneous composites by a suitable linearisation of the cited nonlinear system, able to furnish also an estimation of the propagating wave speed. The performed linearisation is possible

thanks to an optimal configuration of only four closely spaced surface-bonded piezoelectric transducers.

Moreover, two time of arrival techniques, both based on the Akaike information criterion (AIC), are used because of their peculiar characteristic to identify the onset time with high accuracy in the range of microseconds.

Numerous experimental impact tests were performed on two different plates, an aluminium and a CFRP composite one, that confirmed the validity of the developed methodology, able to furnish the expected results with high level of accuracy.

Additionally, a second Appendix, not present in the published paper, is reported at the end of this Chapter, in order to show a comparison among some characteristic functions (CFs) cited in the following publication.

The Statement of Authorship Form and the paper can be found next.

This declaration concerns the article entitled:	
Impact source localisation in Aerospace composite structures	
Publication status (tick one)	
Draft manuscript	
Submitted	
In review	
Accepted	
Published	✓
Candidate's contribution to the paper (detailed, and also given as a percentage)	

The candidate contributed to/ considerably contributed to/predominantly executed the…	
Formulation of ideas:	80% The ideas to linearise the impact nonlinear equations and to use Akaike information criterion as time of arrival estimation algorithms were proposed by me.
Design of methodology:	85% I designed/improved the algorithms that would be used in the localisation method. My supervisors furnished me a first version of time of arrival MATLAB code. I designed the experimental tests, helped by my supervisors.
Experimental work:	90% I conducted all the impact experimental tests, collected all the data, and evaluated all the algorithm outputs. My supervisors helped me in results interpretation.
Presentation of data in journal format:	90% I decided structure, wrote all drafts, prepared all figures. Supervisors provided feedback on drafts and helped with submission, responses to reviews and publication process.

Statement from Candidate			
This paper reports on original research I conducted during the period of my Higher Degree by Research candidature.			
Signed	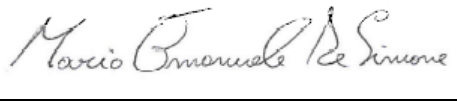	**Date**	26/06/2019

Impact source localisation in Aerospace composite structures

Mario Emanuele DE SIMONE, Francesco CIAMPA, Salvatore BOCCARDI, Michele MEO*

Mechanical Engineering Department, University of Bath, Bath, United Kingdom

* corresponding author: m.meo@bath.ac.uk

Keywords: Impact localisation, composite materials, wave propagation.

ABSTRACT

The most commonly encountered type of damage in aircraft composite structures is caused by low-velocity impacts due to foreign objects such as hail stones, tool drops and bird strikes. Often these events can cause severe internal material damage that is difficult to detect and may lead to a significant reduction of the structure's strength and fatigue life. For this reason, there is an urgent need to develop structural health monitoring systems able to localise low-velocity impacts in both metallic and composite components as they occur.

This article proposes a novel monitoring system for impact localisation in aluminium and composite structures, which is able to determine the impact location in real-time without a-priori knowledge of the mechanical properties of the material. This method relies on an optimal configuration of receiving sensors, which allows linearisation of well-known nonlinear system of equations for the estimation of the impact location. The proposed algorithm is based on the time of arrival identification of the elastic waves generated by the impact source using the Akaike information criterion. The proposed approach was demonstrated successfully on both isotropic and orthotropic materials by using a network of closely spaced surface-bonded piezoelectric transducers. The results obtained show

the validity of the proposed algorithm, since the impact sources were detected with a high level of accuracy. The proposed impact detection system overcomes current limitations of other methods and can be retrofitted easily on existing aerospace structures allowing timely detection of an impact event.

1 INTRODUCTION

In the last few years, both non-destructive evaluation (NDE) and Structural Health Monitoring (SHM) techniques were used for the localisation of acoustic emission (AE) sources due to impact events. Typically, the real-time knowledge of the impact location in metallic and composite materials is achieved through "passive techniques", in which ultrasonic transducers, fixed to the specimen surface or embedded into the structure, can be used to measure the impulsive material response [1].

A number of studies on the detection and localisation of impact sources are well documented in literature, many of them based on the triangulation technique, also known as "Tobias algorithm" [2]. In this methodology, the impact point is identified as the intersection of three circumferences, whose centres are the sensor locations. A triangulation technique can be used for isotropic and homogeneous structures, but it requires the accurate knowledge of the wave velocity that is assumed to be constant in all directions of propagation. Another approach based on the knowledge of the wave speed is the beamforming technique, which was originally introduced by McLaskey et al. [3] and then it was used by He et al [4]. This method is based on the use of a small array of sensors (from four to eight sensing elements) and on the delay-and-sum algorithm. Ciampa and Meo [5] proposed a modification of the triangulation technique in isotropic materials, which did not require the knowledge of the wave speed.

However, the strong limitation of the above mentioned method is that they are not suitable for anisotropic and inhomogeneous materials. Kundu et al. [6, 7] developed an impact localisation technique to locate the impact source in isotropic and anisotropic plates. This algorithm, based on the minimisation of an error function,

or “objective function”, was able to determine the impact coordinates by using four sensors, although the direction dependence of the wave velocity must be known in case of anisotropic media. Nakatani et al. [8] extended the beamforming technique to anisotropic structures with known velocity profile, whilst Seydel and Chang [9, 10] proposed a method based on the minimisation of the difference between the actual and predicted response from piezoelectric sensors. Nevertheless, this technique required the knowledge of the mechanical properties of the medium and a theoretical model for the simulation of dynamic-acoustic behaviour of the structure. Meo et al. [11], Kurokawa et al. [12], developed an algorithm for the impact point identification assuming an elliptical angular-group velocity pattern. This technique can be applied only to quasi-isotropic and unidirectional composite structures.

Since it is generally cumbersome to determine the information on group velocity of propagating waves in geometrically complex components and dispersive media, Ciampa and Meo [13, 14] and Kundu et al. [15, 16], developed impact localisation methods able to localise the acoustic source in an anisotropic plate using only six receiving sensors without the knowledge of the wave velocity. In Ciampa and Meo [13, 14] the impact coordinates and the wave velocities were obtained by solving a set of nonlinear equations through a combination of both local (Newton’s) and global (unconstrained optimisation) methods, whilst in Kundu et al. [15, 16] the acoustic source was localised from the intersection point of two direction lines generated by two clusters of sensors.

Another main issue of impact localisation methods is the estimation of the time of arrival (TOA) with high level of accuracy. The TOA, also called “onset time” of transient signals such as AE, seismograms or ultrasound signals, can be described as the moment when the ballistic wave originated at the impact source reaches one (or more) receiving sensor. The TOA is usually picked as the point where the first difference between the signal and the noise takes place. Several approaches were used in the past for automatic TOA estimation, many of them modified from seismology, due to the similarity between seismology and acoustic fields. The simplest method is to use an amplitude threshold picker, where the onset time is

determined as the time corresponding a signal value immediately before the signal amplitude exceeds a particular threshold value [17]. The magnitude of the squared modulus of the continuous Wavelet transform (CWT) was used by Ciampa and Meo [5, 13, 14] to identify the TOA of the signals and then to calculate the time differences of arrival (TDOAs). However, CWT strongly depends on the selection of the mother wavelet, which may limit its use for structures with complex geometries. Another technique called "Short Term Average (STA) / Long Term Average (LTA)" uses a dynamic threshold to discern the ballistic signal from the level of noise [18]. A number of algorithms based on the STA/LTA method can be found in literature, however its poor accuracy in estimating the TOA was demonstrated in concrete structures [19]. Other techniques for the TOA estimation include cross-correlation [20, 21], energy criterion method, artificial neutral network [22], fractal dimension [23], spectrograms [24] and the Hinkley criterion [25]. Ciampa et al. [26, 27] proposed an alternative technique to the traditional TOA estimation method for acoustic source localisation on composite structures based on the reciprocal time reversal (TR) or inverse filtering (IF) technique. This approach was split into two steps. The first step consisted of recording and storing a set of signals representing a library of impulse responses from a number of excitation points along the plane of the structure using a single surface-bonded receiving transducer. The second step consisted of a correlation between the impulsive transfer function associated with each excitation point and the inversion of the structural response of a new impact of unknown position. The maximum of the IF correlation coefficients corresponded to the impact point. However, this technology required an initial library of impulsive waveforms to be determined during the first step.

This paper starts from the research work of Ciampa and Meo for impact localisation on aluminium [5] and composite structures [13, 14] based on the TOA estimation. The proposed research work uses a different approach for the TOA estimation based on the Akaike information criterion (AIC) that, unlike traditional TOA estimation techniques, it allows identifying the onset time with high accuracy in the range of microseconds. Moreover, the proposed research work provides a linearisation of

the nonlinear system of equations to be solved. This would eliminate the dependence on the guess conditions for the identification of the impact coordinates. At the same time, the aim of this paper is to minimise the number of transducers, thus optimising the sensors configuration. The general assumption is that the composite material is homogeneous and anisotropic at the structural level. In strongly inhomogeneous media, the straight-line propagation path of direct (ballistic) waves from the impact source to the receiver transducer could be interrupted by discontinuities (e.g. surface and subsurface flaws) that may alter the propagation path and generate wave scattering and reflections according to the Snell's law. However, this is not the case of this paper.

The outline of this research work is as follows: in Section 2, the linearised algorithm for the impact localisation is described. In Section 3, the Akaike information criterion is presented, with the description of two AIC pickers able to identify the TOA of a signal. Section 4 shows the set-up used to perform experimental tests, whilst in Section 5, all the impact localisation results are illustrated. The conclusions of this paper are presented in Section 6.

2 IMPACT LOCALISATION ALGORITHM

Let us consider an impact source point I, or a general acoustic emission source, at unknown coordinates (x_I, y_I) in the plane of the plate $x - y$. A number of n receiving transducers, are located at distance d_i $(i = 1, \dots, n)$ from the source. The origin of the Cartesian reference frame was arranged at the left bottom corner of the plate, whose dimensions are L, length, and W, width.

The coordinates of the impact source can be determined by solving the following general system of nonlinear equations [13, 14]:

$$\begin{cases} \|d_i\|^2 = (x_i - x_I)^2 + (y_i - y_I)^2 \\ t_i = \dfrac{\|d_i\|}{V_{g,i}} \end{cases}, \qquad i = 1, \dots, n\,, \tag{1}$$

where $V_{g,i}$ are the velocities of propagation of the stress wave reaching the i^{th} transducer, t_i are the times of detection of the AE signals and (x_i, y_i) are the coordinates of the i^{th} sensor.

Combining both terms of (1) it is possible to obtain a number of n equations in the form of:

$$(x_i - x_I)^2 + (y_i - y_I)^2 - \left(t_i V_{g,i}\right)^2 = 0\,, \qquad i = 1, \dots, n\,, \tag{2}$$

which is the equation of a circumference with radius ${r_i}^2 = \left(t_i V_{g,i}\right)^2$. We have a system of n nonlinear equations for $2(n+1)$ unknowns (i.e. n velocities, n times of arrival and two source coordinates). Considering one of the sensor as "reference sensor", it is possible to relate the travel time required to reach this sensor, t_{ref}, and the time differences of arrival between other sensors and the reference one, $\Delta t_{ref,j}$, obtaining an expression for the time of arrival concerning the j^{th}, sensor:

$$t_j = t_{ref} \pm \Delta t_{ref,j}\,, \qquad j = 1, \dots, n - \{ref\}\,. \tag{3}$$

Substituting (3) into (2), it becomes:

$$\begin{cases} \left(x_j - x_I\right)^2 + \left(y_j - y_I\right)^2 = \left[\left(t_{ref} \pm \Delta t_{ref,j}\right) V_{g,j}\right]^2 \\ \left(x_{ref} - x_I\right)^2 + \left(y_{ref} - y_I\right)^2 = \left(t_{ref} V_{g,ref}\right)^2 \end{cases}. \tag{4}$$

$$j = 1, \dots, n - \{ref\}$$

Considering TDOAs as determined by using an appropriate TOA estimation method, the number of unknowns is equal to $n + 3$ (i.e. n velocities, the time of arrival of the reference sensor and two source coordinates). Our aim is to reduce the number of surface-bonded transducers up four sensors. Since system (4) can only be solved if the number of variables is equal to the number of equations, an optimal sensor configuration is necessary to solve the system of equations. The main idea is to locate the four sensors relatively close together (see Figure 1), so that they experience the same propagation velocity $\left(V_{g,i} = V_g\right)$.

With this assumption system (4) becomes:

$$\begin{cases} (x_j - x_I)^2 + (y_j - y_I)^2 = [(t_{ref} \pm \Delta t_{ref,j})V_g]^2 \\ (x_{ref} - x_I)^2 + (y_{ref} - y_I)^2 = (t_{ref} V_g)^2 \end{cases} . \quad (5)$$

$$j = 1, \dots, 4 - \{ref\}$$

System (5) consists of four equations for four unknowns, $\{\boldsymbol{x}\} = \{x_I, y_I, t_{ref}, V_g\}$ and its resolution, after a suitable linearisation, is the topic of next sub-section.

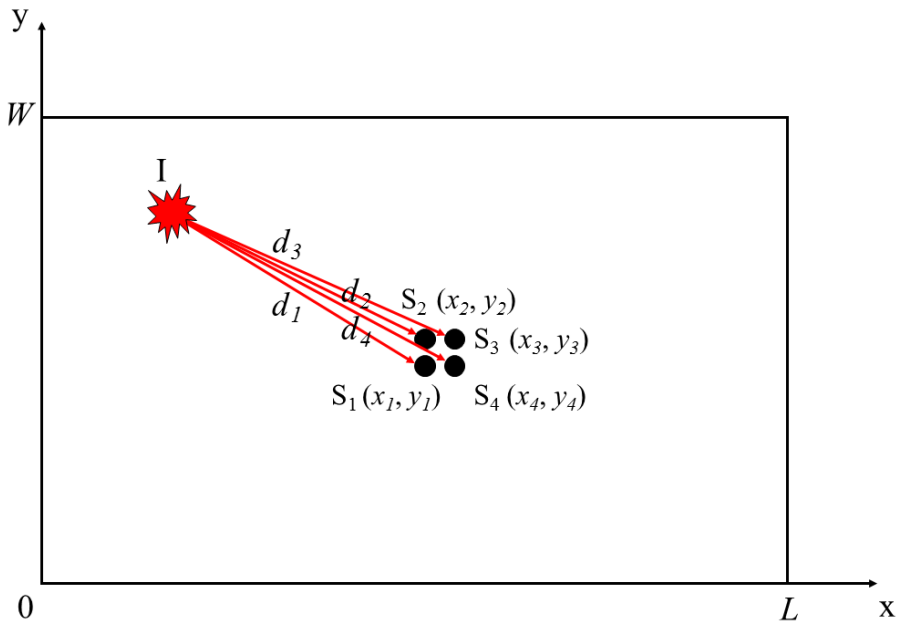

Figure 1. Sensor arrangement for the source location.

2.1 LINEARISATION PROCESS

Subtracting the reference sensor equation from other equations in (5), the following system of equations is obtained:

$$\begin{aligned} {x_j}^2 - {x_{ref}}^2 - 2x_j x_I + 2x_{ref} x_I + {y_j}^2 - {y_{ref}}^2 - 2y_j y_I + 2y_{ref} y_I \\ = {V_g}^2 \Delta t_{ref,j} (2t_{ref} + \Delta t_{ref,j}) . \end{aligned} \quad (6)$$

Considering the known quantities $b_j = \left({x_j}^2 + {y_j}^2\right) - \left({x_{ref}}^2 + {y_{ref}}^2\right)$, equations (6) become:

$$b_j - 2\left[x_I\left(x_j - x_{ref}\right) + y_I\left(y_j - y_{ref}\right)\right] - {V_g}^2\Delta t_{ref,j}\left(2t_{ref} + \Delta t_{ref,j}\right) = 0\,. \tag{7}$$

It is possible to use the following positions for the known differences between sensors coordinates, $x_{ref,j} = x_j - x_{ref}$ and $y_{ref,j} = y_j - y_{ref}$, so that equations (7) can be written as:

$$b_j - 2\left[x_I x_{ref,j} + y_I y_{ref,j}\right] - {V_g}^2\Delta t_{ref,j}\left(2t_{ref} + \Delta t_{ref,j}\right) = 0\,. \tag{8}$$

Rearranging equations (8), they become:

$$x_I x_{ref,j} + y_I y_{ref,j} + {V_g}^2 t_{ref}\Delta t_{ref,j} = \frac{b_j}{2} - {V_g}^2\frac{{\Delta t_{ref,j}}^2}{2}\,, \tag{9}$$

which in matrix form, assuming sensor 1 as the reference sensor, can be expressed as:

$$\begin{bmatrix} x_{1,2} & y_{1,2} & \Delta t_{1,2} \\ x_{1,3} & y_{1,3} & \Delta t_{1,3} \\ x_{1,4} & y_{1,4} & \Delta t_{1,4} \end{bmatrix}\begin{Bmatrix} x_I \\ y_I \\ {V_g}^2 t_1 \end{Bmatrix} = \frac{1}{2}\begin{Bmatrix} b_2 \\ b_3 \\ b_4 \end{Bmatrix} - \frac{{V_g}^2}{2}\begin{Bmatrix} {\Delta t_{1,2}}^2 \\ {\Delta t_{1,3}}^2 \\ {\Delta t_{1,4}}^2 \end{Bmatrix}, \tag{10}$$

or, in general, as reported below:

$$[A]\{\boldsymbol{x}\} = \{B\} - {V_g}^2\{C\}\,. \tag{11}$$

The variables vector is expressed by:

$$\{\boldsymbol{x}\} = [A]^{-1}\{B\} - {V_g}^2[A]^{-1}\{C\}\,. \tag{12}$$

Considering the following positions, $a_k = [A]^{-1}\{B\}|_k$ and $c_k = [A]^{-1}\{C\}|_k$, with $k = 1, 2, 3$, we achieve:

$$\begin{Bmatrix} x_I \\ y_I \\ {V_g}^2 t_1 \end{Bmatrix} = \begin{Bmatrix} a_1 \\ a_2 \\ a_3 \end{Bmatrix} - {V_g}^2\begin{Bmatrix} c_1 \\ c_2 \\ c_3 \end{Bmatrix}. \tag{13}$$

The final expressions for the four unknowns are:

$$\begin{cases} x_I = a_1 - {V_g}^2 c_1 \\ y_I = a_2 - {V_g}^2 c_2 \\ {V_g}^2 t_1 = a_3 - {V_g}^2 c_3 \end{cases} . \quad (14)$$

Substituting expressions (14) in the reference sensor equation in (5) and after some mathematical manipulation, a final third order equation, with reference time of arrival, t_1, as only unknown, is formulated as follows:

$$ {t_1}^3 Z_1 + {t_1}^2 Z_2 + t_1 Z_3 + Z_4 = 0 , \quad (15)$$

where Z_i coefficients are combinations of known quantities that for clarity reasons are reported in the Appendix.

Although (15) admits three possible solutions, only one of them is physically feasible, whereas the other two should be discarded. After obtaining t_1 from (15), the propagation velocity can easily be calculated using the following equation, coming from the third of (14):

$$V_g = \sqrt{\frac{a_3}{t_1 + c_3}} . \quad (16)$$

Finally, it is possible to obtain the values of the impact coordinates substituting (16) in the first two equations in (14).

3 AKAIKE INFORMATION CRITERION METHOD

Since the inputs of the proposed algorithm are the time differences of arrival, a suitable approach for time of arrival estimation needs to be chosen. In this research work the onset time determination is based on the Akaike information criterion [28-31].

The main assumption for AIC is to consider the signal, or a general time series, as divided in two different locally stationary segments [31], each modelled as an autoregressive (AR) process. The first segment is the non-informative part, and it is called “noise”, while the second one is the informative part, and it is called

"signal". These two datasets are separated by the onset time. The AIC, derived by [28], is represented by the following equation:

$$AIC = -2\,ln(L) + 2P\,, \tag{17}$$

where P is the number of parameters in the statistical model, and L is the maximised value of the likelihood function for the estimated model. Originally the optimal order for an AR process fitting a time series was determined by using function (17). When there are several competing models, the minimum AIC estimation (MAICE) is defined by the model which gives the minimum of AIC function [30]. The model is established by a mathematical method illustrated by Kitagawa and Akaike [31].

A time series $\{x_{1,}\, x_{2,}\, \dots, x_n\}$ can be divided into two segments $(j = 1, 2)$, $\{x_{1,}\, x_{2,}\, \dots, x_k\}$ and $\{x_{k+1,}\, x_{2,}\, \dots, x_n\}$ where k indicates the point whose corresponding time is the unknown onset time. Both segments could be expressed by:

$$x_i = \sum_{m=1}^{M} a_m^j\, x_{i-m} + e_i^j\,, \qquad j = 1, 2\,, \tag{18}$$

where M is the order and a_m^j are the coefficients of the AR process used to model the two datasets. Furthermore $i = M + 1, \dots, k$ for interval $j = 1$, and $i = k + 1, \dots, n - M$ for $j = 2$.

Both time series are divided into a deterministic and a non-deterministic part, e_i^j, the second one considered as a Gaussian white noise, with mean zero, variance σ_j^2 and uncorrelated with the deterministic part. The non-deterministic part of the time series in two intervals can be extracted by using the maximum likelihood estimation (MLE).

Considering the previous hypothesis about the noise model, it is possible to express the joint density function of all variables e_i^j, considered as fixed parameters, through the approximate likelihood function L:

$$L(\Theta_j, k, M|x) = \prod_{j=1}^{2} \left(\frac{1}{\sigma_j^2 2\pi}\right)^{n_j/2} exp\left[-\frac{1}{2\sigma_j^2} \sum_{i=p_j}^{q_j} \left(x_i - \sum_{m=1}^{M} a_m^j \, x_{i-m}\right)^2\right], \tag{19}$$

where $\Theta_j = \Theta_j\left(a_1^j, \dots, a_m^j, \sigma_j^2\right)$ represents the model parameters, $p_1 = M + 1$, $p_2 = k + 1$, $q_1 = k$, $n_1 = k - M$, $n_2 = n - k - M$.

By using MLE it is possible to find the values of the model parameters that make the observed results the most probable, the same that maximise the equation (19). Considering the logarithm of equation (19) and searching for the MLE of the model parameters we obtain:

$$\frac{\partial \, ln \, L}{\partial \Theta_j} = 0 \, , \tag{20}$$

whose solution can be expressed as:

$$\sigma_{j,max}^2 = \frac{1}{n_j} \sum_{i=p_j}^{q_j} \left(x_i - \sum_{m=1}^{M} a_m^j \, x_{i-m}\right)^2 \, . \tag{21}$$

It is simple to obtain the maximised logarithmic likelihood function inserting equation (21) into equation (19):

$$ln \, L = -\frac{k - M}{2} \, ln \, \sigma_{1,max}^2 - \frac{n - k - M}{2} \, ln \, \sigma_{2,max}^2 + C_1 \, , \tag{22}$$

where C_1 is a constant. Equation (22) is the basis for equation (17). In the case of fixed M order, as in current application, AIC function is a measure for the model fit. k point where AIC is minimised, or equivalently L is maximised, indicates the optimal separation of the two time series and the corresponding time value is regarded as the onset time of the signal [32, 33].

Considering AIC as function of merging point *k*, we have the AR-AIC picker expressed by the following equation:

$$AIC(k) = (k - M)\, ln\, \sigma_{1,max}^2 + (n - k - M)\, ln\, \sigma_{1,max}^2 + C_2\,, \qquad (23)$$

where C_2 is a constant. It is possible to calculate the AIC function directly from the signal without using the AR coefficients, considered that for the AR-AIC picker the order M of the AR process must be specified by trial and error and the AR coefficients have to be calculated for both intervals. Considering $M \ll n$ and constant C_2 as a negligible quantity if n is large enough, equation (23) is simplified in the Maeda's relation [34]:

$$AIC(k) = k\, ln\big(var(x[1,k])\big) + (n - k - 1)\, ln\big(var(x[k+1,n])\big)\,, \qquad (24)$$

where k represents the range through all points of the signal and $var(\cdot)$ is the sample variance.

AIC function (24) is the basis equation for the methods used in this research work. After computation of AIC function, it is necessary to calculate its global minimum. The relative time value can be considered the time of arrival of the signal. It should be noted that for the TOA calculation only a part of the time series containing the onset time should be considered. The selection of this time window and the signal-to-noise (S/N) ratio determine the accuracy of TOA.

3.1 PREVIOUS AIC PICKERS

Several procedures were presented in literature to manage the two related problems: a proper choice of the time window and the appropriate signal to use in the algorithm, dependent on the S/N ratio of the original signal. They generally depend on the application field: e.g. seismology [32-36] and acoustic [19, 37-40]. There are many similarities between acoustic emissions and seismograms, however a number of differences are present, as the fact that in seismology the signal and the noise are usually located in different frequency range. In this case it is possible to obtain reliable results eliminating the noise through a simple Fourier transform and corresponding filter. AE signal and noise are often in the same frequency range (20-

500 kHz) with a consequent variable signal-to-noise ratio. A signal would be influenced unavoidably after an inadequate filtering, with incorrect time of arrival results as principal consequence [41]. Therefore, it is necessary to diminish the noise as much as possible instead of eliminating it, by using, for example a Butterworth filter, whose characteristics are dependent on considered signal.

In seismology, Zhang et al. [33] applied the AIC picker to detect the *P*-wave arrival using the time window chosen by the discrete wavelet transform, acting to single-components seismograms through a series of sliding time windows. For AE in concrete, Kurz et al. [19] applied an adapted automatic AIC picker based on (24), considering two particular signal-envelopes instead of signal: the complex wavelet transform and Hilbert transform; the time window was chosen after the determination of a first onset, obtained by using a constant threshold value on the squared and normed signal-envelope.

In this research work two different AIC pickers are considered, here referred as "characteristic function AIC picker" [37, 38] and "threshold AIC picker" [39, 40]. They are described in Sections 3.2 and 3.3 respectively.

3.2 CHARACTERISTIC FUNCTION AIC PICKER

3.2.1 Choice of characteristic function

The first considered AIC picker is based on a suitable mathematical function, called "characteristic function" (CF), whose purpose is to improve the resolution level between noise and signal through the enhancement of changes in signal features [42] such as the frequency, the amplitude or both. In correspondence of these changes, it is possible to detect the time of arrival of the signal. For this reason, the performance of the picker highly depends on the chosen characteristic function. Among all characteristic functions used in literature, it is possible to remember the functions that enhances the signal amplitude changes: the absolute value function $CF(i) = |x(i)|$, the square function $CF(i) = x(i)^2$, the envelope of the signal calculated by Hilbert transform and the squared envelope. The principal limitation is that these functions are not sensitive to periodic signal changes, very useful if a

low signal-to-noise ratio signal is considered. To overcome this limitation frequency-sensitive functions need to be chosen, such as the Allen's function, a squared polynomial function used for a seismogram threshold picker [42]:

$$CF(i) = x(i)^2 + R_1\big(x(i) - x(i-1)\big)^2 , \tag{25}$$

where $R_1\big(x(i) - x(i-1)\big)^2$ represents changes in frequency, with R_1 as a weighting constant dependent on the signal. Despite equation (25) is suitable for changes in amplitude and frequency, it can be used effectively for bulk specimens and not for thin plates. Because of it is a square function, it can suppress the amplitude of the first and weaker mode, much lower respect to the amplitude of the second mode if a thin plate is considered. In this research work the following characteristic function, suitable for thin plate, is chosen:

$$CF(i) = |x(i)| + R_2|x(i) - x(i-1)| , \tag{26}$$

where R_2 is a constant set to $R_2 = 4$ for thin-plate specimens in accordance to [37, 38].

3.2.2 AIC picker algorithm

The algorithm is divided into two steps (Figure 2), consisting of a first rough estimation of the onset time during the first step, with a more precise determination of it during the second step. The first step starts with the determination of a shortened time window. The starting time was set at the beginning of the original signal within the noise level and considered a non-informative part. The ending time was set after the global maximum of the characteristic function (26), t_{MAX}, on time $t_{\mathrm{MAX}} + \Delta t_{\mathrm{AM}}$. The time delay Δt_{AM} is a value depending on the tested material, set to 20 μs for our experiment and suitable for thin-plate specimens in accordance to [37, 38]. Maeda's relation (24), with the characteristic function (26) as input, is applied on this time window and the first onset time, t_{MIN}, is determined. The aim of the second step is to increase the accuracy of the AIC picker by focusing on the neighbourhood of the first estimation. A new time window is considered, whose

limits are $t_{\mathrm{MIN}} - \Delta t_{\mathrm{FB}}$ and $t_{\mathrm{MIN}} + \Delta t_{\mathrm{FA}}$, where the setting are $\Delta t_{\mathrm{FB}} = 30$ μs and $\Delta t_{\mathrm{FA}} = 10$ μs, chosen according to [37, 38]. A new application of (24) on this new time window defines the actual time of arrival.

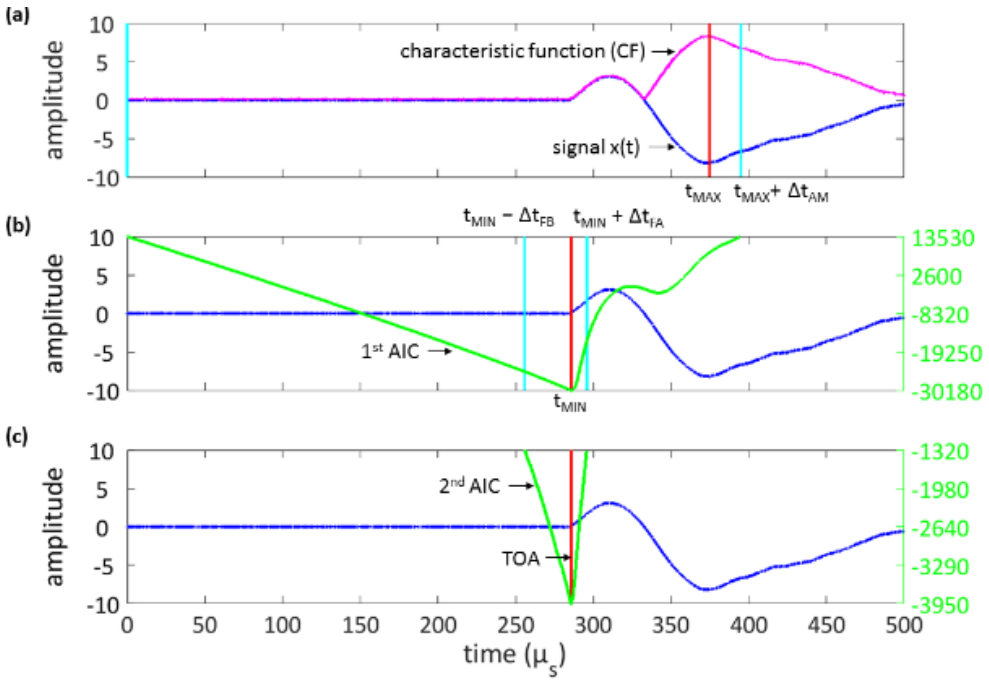

Figure 2. Visual description of CF-AIC picker: determination of the initial time window (a); estimation of the first TOA and determination of the second time window (b); estimation of the final TOA (c).

3.3 THRESHOLD AIC PICKER

The second considered AIC picker is, as the first one, a two-step process (Figure 3). The structure of the steps is very similar to the previous AIC picker, but in this case it is not necessary a characteristic function.

During the first step, Maeda's relation (24), with the original signal as input, is applied on a shortened time window that is determined by using the following threshold amplitude level:

$$\left(\sum_{i=k+1}^{10} |x(i)|\right) \Big/ 10 \geq T \left(\sum_{i=1}^{k} |x(i)|\right) \Big/ k \,, \tag{27}$$

where there is a comparison between the mean amplitude of a shifting set of 10 data [left part of (27)] and the mean amplitude of the interval of the time series ranging from 1 to k multiplied by a constant T depending on the signal [right part of (27)]. The ending of time window is set at the time t_0 corresponding to the first value k_0 that satisfies expression (27). The first estimation of the onset time t_1 is determined considering the interval $[0, t_0]$.

The second step considers a time window centred in t_1 with a length of $2\Delta k$, where Δk depends on the sample frequency. For our purpose, a variant of this method, that considers a length of $2(t_1 - t_0)$ for the second time window, is used [40]. A new application of (24) on this new time window defines the actual time of arrival.

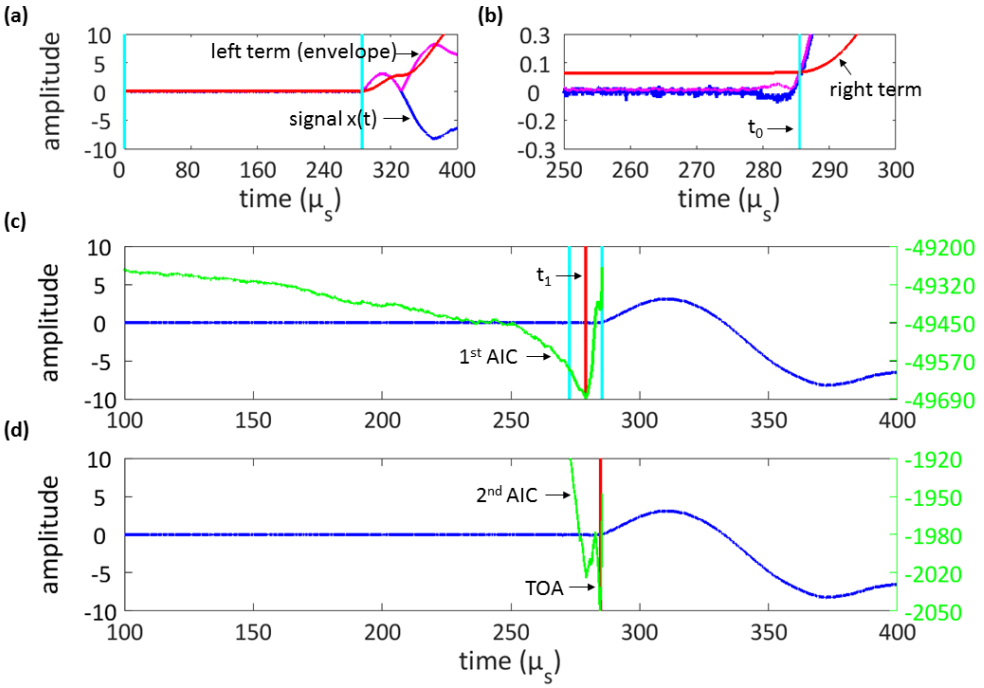

Figure 3. Visual description of threshold AIC picker: determination of the initial time window (a) [left term refers to formula (27)]; zoom on onset time zone (b) [right term refers to formula (27)]; estimation of the first TOA and determination of the second time window (c); estimation of the final TOA (d).

4 EXPERIMENTAL SET-UP

To validate the described algorithms, experimental impact location tests were conducted on two different structures (see Figure 4 and Figure 5):

- an aluminium plate with dimensions $350 \times 260 \times 8\ \text{mm}^3$;
- a carbon fibre reinforced plastic (CFRP) plate with dimensions $290 \times 290 \times 5\ \text{mm}^3$.

The impacts were generated by using an aluminium sphere with 5 mm radius ($\text{mass} \cong 1.4\ \text{g}$), dropped from 100 mm height so that the same impact energy was achieved (around 0.0014 J). The impulsive waveforms were measured employing four surface-bonded piezoelectric transducers (PIC 255) with diameter of 6.5 mm and thickness of 0.3 mm. By considering the small dimensions of sensors (e.g. the maximum diameter was 6.5 mm), the squared configuration shown in Figure 1 was assumed as the most suitable among all possible geometries, so that the transducers could be relatively close together. Other configurations and geometries would have not fulfilled the fundamental condition that all receiver transducers will experience the same group velocity. The signals were acquired using a four-channel oscilloscope with 16 bits of resolution, a sampling rate of 20 MHz and an acquisition window of 5 ms. A MATLAB software code implemented by the authors was written to analyse the waveforms for finding the TOA and the impact location by using the linearised algorithm. Sensor locations are reported in Table 1. The Cartesian reference frame was chosen with the origin at the bottom left corner of the specimens.

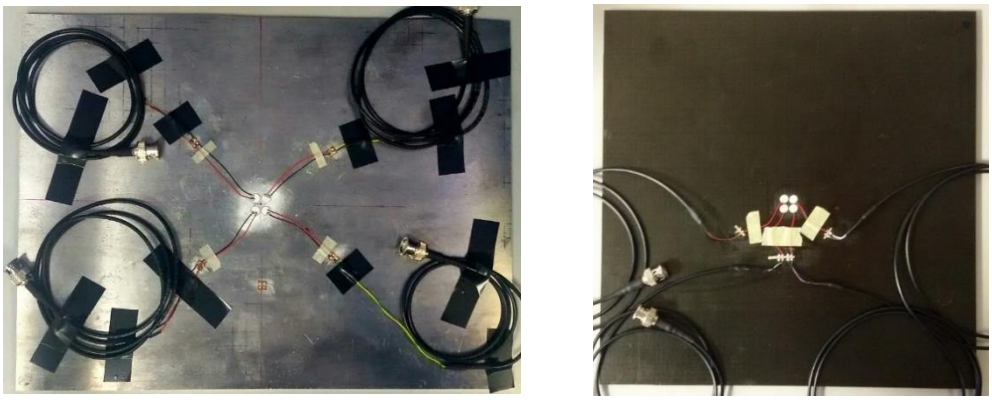

Figure 4. Considered specimens: aluminium plate (left) and composite plate (right).

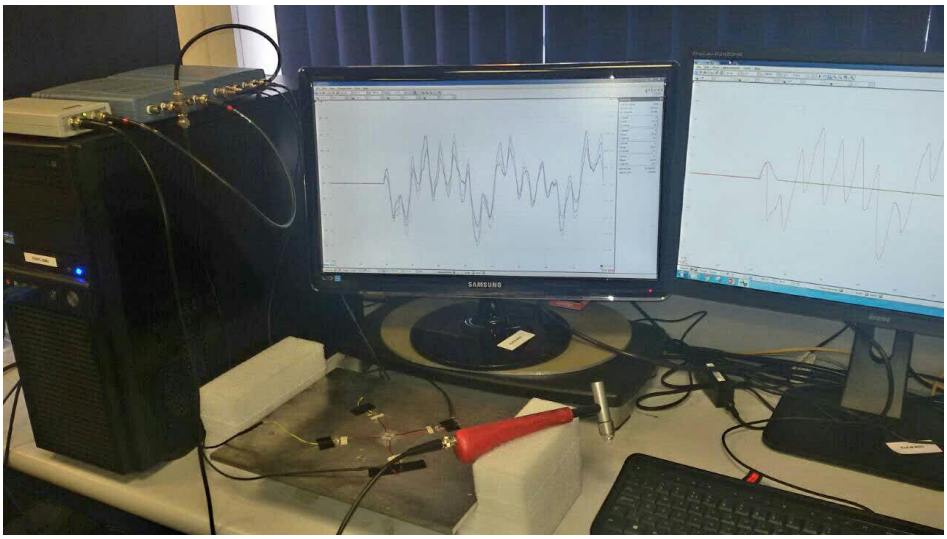

Figure 5. Experimental set-up.

Table 1. Sensor coordinates on the considered specimens.

	Aluminium		Composite	
	x-Coord (mm)	y-Coord (mm)	x-Coord (mm)	y-Coord (mm)
Sens 1	177	126	142	135
Sens 2	176	134	142	142
Sens 3	185	134	149	142
Sens 4	184	126	149	135

5 IMPACT LOCALISATION RESULTS

Table 2 and Figure 6 shows an example of TOA calculation, considering Impact 1 on the aluminium plate and the threshold AIC picker.

Table 2. TOA results – Impact 1 and threshold AIC picker (aluminium plate).

	TOA_{S1} (μs)	TOA_{S2} (μs)	TOA_{S3} (μs)	TOA_{S4} (μs)
Impact 1	933.6	930.52	930.3	933.78

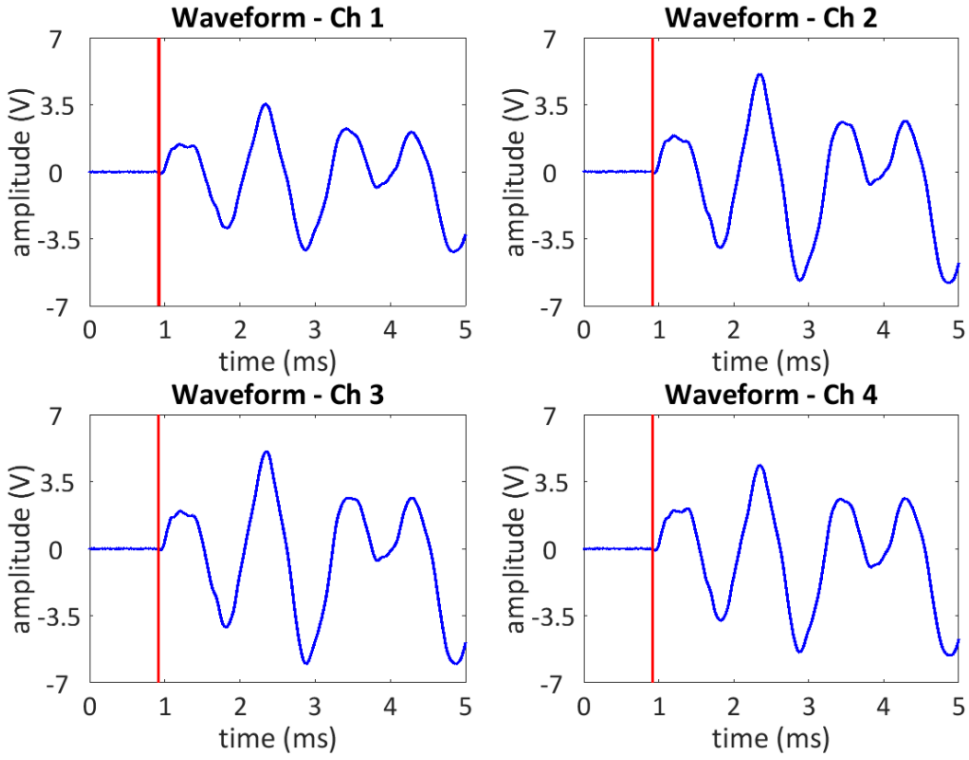

Figure 6. Acquired signals and calculated TOAs – Impact 1 and threshold AIC picker (aluminium plate).

Since the receiving sensors are very close each other, the TOAs are of the order of microseconds. The absolute TOA differences obtained by using both AIC picker methods described in Section 3 are reported in Table 3.

Table 3. Absolute TOA differences using both AIC pickers.

	Sensor 1 (μs)		Sensor 2 (μs)		Sensor 3 (μs)		Sensor 4 (μs)	
	Al	Comp	Al	Comp	Al	Comp	Al	Comp
Impact 1	4.14	5.19	4.1	5.2	4.1	5.2	4.14	5.19
Impact 2	6.88	7.07	6.83	6.9	6.87	6.91	6.93	7.07
Impact 3	6.12	9.21	6.12	9.09	6.12	9.22	6.12	9.26
Impact 4	7.23	9.05	7.24	9.04	7.23	9.04	7.23	9.05
Impact 5	5.42	8.17	5.42	8.07	5.44	7.93	5.42	8.07
Impact 6	6.42	5.81	6.42	5.8	6.42	5.8	6.36	5.81
Impact 7	5.09	20.74	5.09	20.75	5.01	20.77	5.04	20.76
Impact 8	5.57	19.07	5.59	19.06	5.54	19.06	5.5	19.06
Impact 9		9.77		9.7		9.55		9.63

As it can be seen in Table 3, the maximum difference in TOAs is less than 21 μs. Figure 7 and Figure 8 show the source localisation results considering the two specimens, whilst Table 4 and Table 5 depict the evaluated impact position and the location error as expressed by the following formula [43]:

$$\Psi = \sqrt{(x_{real} - x_{calculated})^2 + (y_{real} - y_{calculated})^2}\,, \tag{28}$$

where (x_{real}, y_{real}) are the coordinates of the real impact position and $(x_{calculated}, y_{calculated})$ are the coordinates of the impact location using the described algorithm.

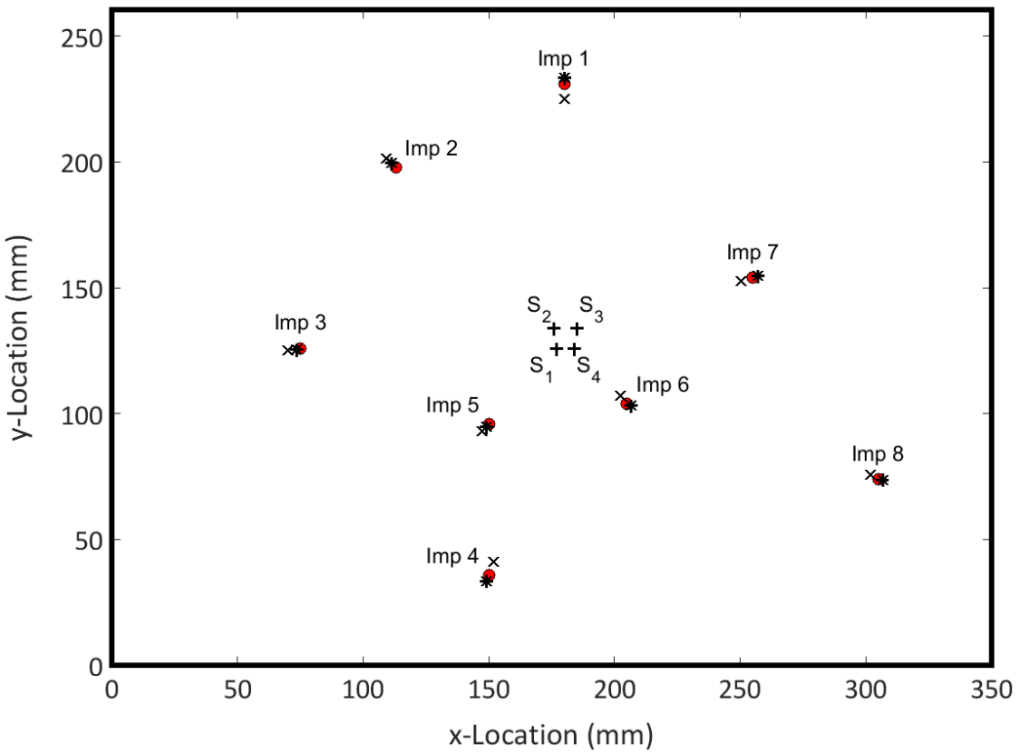

Figure 7. Source location results on the aluminium plate. The calculated impact positions are shown as a cross (×) for the CF-AIC picker, and as a star (∗) for the threshold AIC picker. The true impact positions are shown as a circle (∘).

Table 4. Impact positions and errors for the aluminium plate.

	x-Coord (mm, real value)	x-Coord (mm, detected value – CF AIC picker)	x-Coord (mm, detected value – threshold AIC picker)	y-Coord (mm, real value)	y-Coord (mm, detected value – CF AIC picker)	y-Coord (mm, detected value – threshold AIC picker)	Location error Ψ (mm, CF AIC picker)	Location error Ψ (mm, threshold AIC picker)
Impact 1	180	180.1	180.13	231	225.09	233.35	5.91	2.35
Impact 2	113	109.35	111.36	198	201.44	199.51	5.02	2.23
Impact 3	75	70.05	73.48	126	125.28	125.4	5	1.63
Impact 4	150	151.88	149.26	36	41.02	33.28	5.36	2.82
Impact 5	150	147.52	149.09	96	93.06	94.72	3.85	1.57
Impact 6	205	202.53	206.52	104	107.29	103.1	4.11	1.77
Impact 7	255	250.35	256.93	154	152.53	154.74	4.88	2.07
Impact 8	305	301.78	306.82	74	75.85	73.55	3.71	1.87

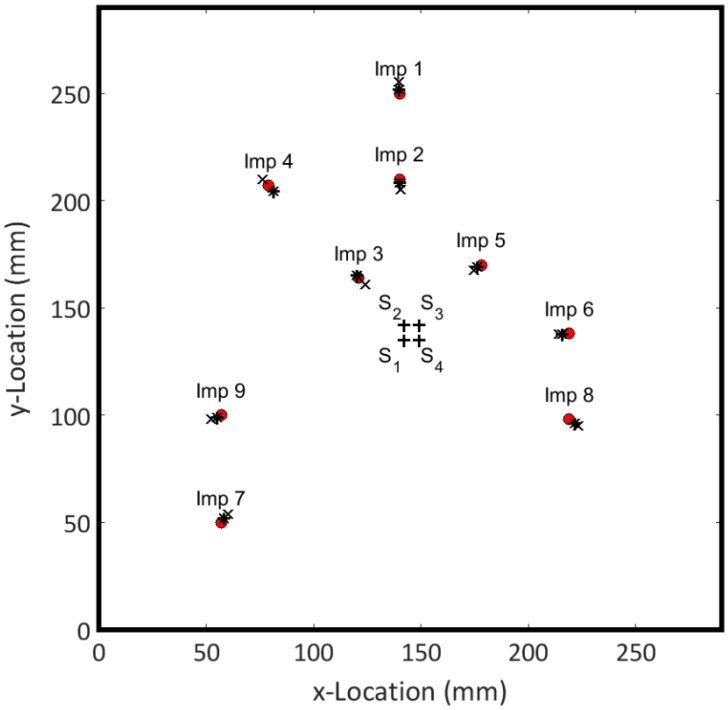

Figure 8. Source location results on the composite plate. The calculated impact positions are shown as a cross (×) for the CF-AIC picker, and as a star (∗) for the threshold AIC picker. The true impact positions are shown as a circle (∘).

Table 5. Impact positions and errors for the composite plate.

	x-Coord (mm, real value)	x-Coord (mm, detected value – CF AIC picker)	x-Coord (mm, detected value – threshold AIC picker)	y-Coord (mm, real value)	y-Coord (mm, detected value – CF AIC picker)	y-Coord (mm, detected value – threshold AIC picker)	Location error Ψ (mm, CF AIC picker)	Location error Ψ (mm, threshold AIC picker)
Impact 1	140	139.7	139.9	250	255.46	251.81	5.47	1.81
Impact 2	140	140.38	140.17	210	205.29	208.24	4.73	1.77
Impact 3	121	124.1	119.95	164	160.71	165.05	4.52	1.48
Impact 4	79	76.18	81.31	207	209.9	204.39	4.05	3.49
Impact 5	178	174.58	176.12	170	167.54	169.11	4.21	2.08
Impact 6	219	214.27	215.84	138	137.63	137.59	4.74	3.19
Impact 7	57	59.99	58.22	50	53.73	51.8	4.78	2.17
Impact 8	219	223.26	221.46	98	95.02	96.06	5.2	3.13
Impact 9	57	52.46	54.96	100	98.14	98.99	4.91	2.28

With reference to Table 4 and Table 5, both AIC pickers are able to localise impacts with an accuracy described by a small location error Ψ less than 6 mm for both aluminium and composite samples.

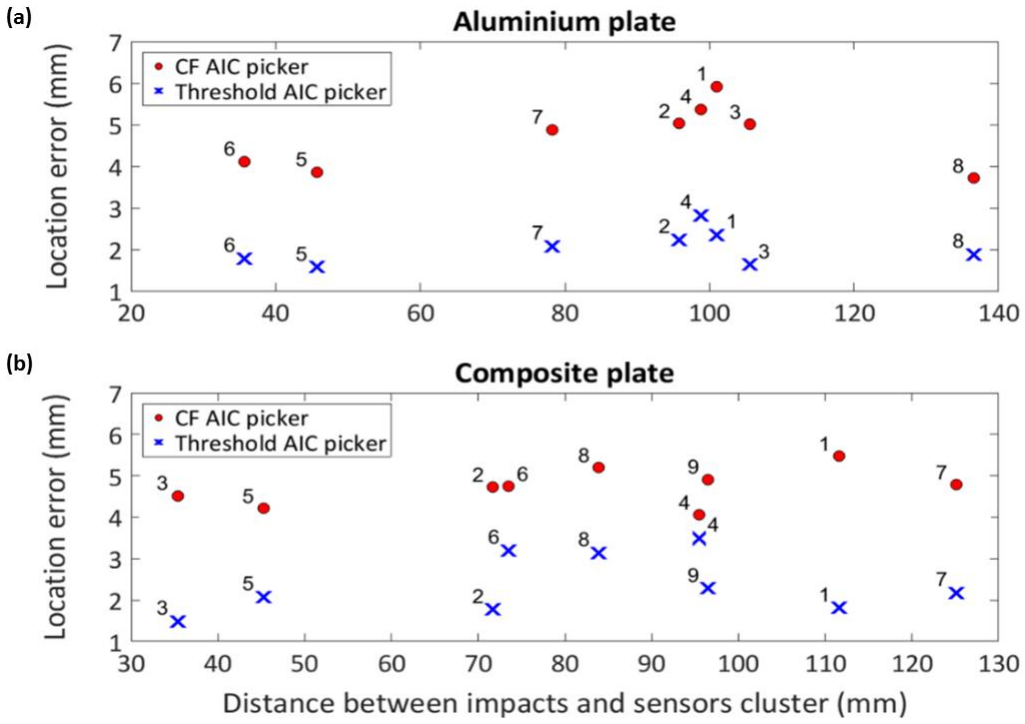

Figure 9. Localisation error using both the CF and threshold AIC methods for the impacts on the aluminium sample (a) and the composite plate (b).

In accordance with Table 4 and Table 5, Figure 9 shows a summary of the impact localisation error Ψ as function of the distance between the impact point and the centre of sensor cluster for the aluminium and composite samples using both the standard AIC picker and the threshold one. As it can be seen from this figure, the threshold AIC method provided better results with a maximum localisation error less than 3 mm for the aluminium sample and less than 4 mm for the composite plate. However, it is difficult to find a clear trend of the localisation error increasing with the distance between the impact point and the sensors cluster location [see for instance the location errors of Impacts 3 and 8 in Figure 9a and of Impacts 4 and 9 in Figure 9b]. This could be due to undesired instrumentation effects such as the cross-talk in the receiving signals, which are independent from the localisation

algorithm and may systematically affect the time of arrival estimation. Table 6 reports the wave velocities obtained from the impact localisation algorithm considering both TOAs calculation methods. Since the energy of each impact was the same, the order of magnitude of the wave velocity for each test specimen was very similar (see Table 6). This was an expected result that further confirms the validity of the proposed impact localisation algorithm.

Table 6. Wave velocities (m/s).

	Aluminium		Composite	
	CF AIC picker	threshold AIC picker	CF AIC picker	threshold AIC picker
Impact 1	2523.2	2555.2	1953.9	1952
Impact 2	2521.4	2577.7	1950.1	2044.4
Impact 3	2523.5	2522.1	1966.8	2041.7
Impact 4	2520.3	2520.8	1950.9	1955.4
Impact 5	2566.4	2574.8	1954.9	2049.8
Impact 6	2540.5	2573.7	1953	1953
Impact 7	2522.7	2576.8	1951.2	1959.4
Impact 8	2522.5	2578.1	1950.1	1950.3
Impact 9			2047.7	1957.4

6 CONCLUSIONS

A new linearised algorithm for the impact source localisation and wave velocity determination was here presented. It is based on the differences of the stress waves measured by four surface-bonded AE piezoelectric transducers. An optimal sensor configuration was used to linearise the system of equations for the identification of the impact coordinates. The acquired signals were processed in order to determine

the TOAs as an input of the proposed algorithm. Two different methods based on Akaike information criterion were performed to provide an accurate TOA results. A number of experimental impact tests were performed on two different specimens, an aluminium and composite plate in order to validate the proposed methodology. Impact localisation results showed the validity of this algorithm, which was able to predict the impact point with high accuracy, i.e. with a maximum location error less than 4 mm by using the threshold AIC picker and with an impact error ranging between 4 and 6 mm by using the characteristic function AIC picker. Since the computational time of both AIC pickers is similar, the threshold one can be used for further TOA applications. This impact localisation method overcomes the limits of previous triangulation approaches as it does not need the knowledge of the material proprieties and the wave velocity. This could be embedded into an automatic impact localisation system that can be retrofitted on existing structures leading to more efficient inspection and enabling prediction of damage severity. By knowing impacts occurrence and location, would allow for a localised search, saving time and expense, and maintenance can be scheduled only when necessary.

REFERENCES

1. Balageas, D., Fritzen, C. P., & Güemes, A. (Eds.) (2010). Structural Health Monitoring. (Vol. 90). John Wiley & Sons.
2. Tobias, A. (1976). Acoustic-emission source location in two dimensions by an array of three sensors. *Non-destructive testing*, *9*(1), 9-12.
3. McLaskey, G. C., Glaser, S. D., & Grosse, C. U. (2010). Beamforming array techniques for acoustic emission monitoring of large concrete structures. *Journal of Sound and Vibration*, *329*(12), 2384-2394.
4. He, T., Pan, Q., Liu, Y., Liu, X., & Hu, D. (2012). Near-field beamforming analysis for acoustic emission source localization. *Ultrasonics*, *52*(5), 587-592.
5. Ciampa, F., & Meo, M. (2010). Acoustic emission source localization and velocity determination of the fundamental mode A_0 using wavelet analysis and a Newton-based optimization technique. *Smart Materials and Structures*, *19*(4), 045027.
6. Kundu, T., Das, S., & Jata, K. V. (2007). Point of impact prediction in isotropic and

anisotropic plates from the acoustic emission data. *The Journal of the Acoustical Society of America*, *122*(4), 2057-2066.

7. Kundu, T., Das, S., Martin, S. A., & Jata, K. V. (2008). Locating point of impact in anisotropic fiber reinforced composite plates. *Ultrasonics*, *48*(3), 193-201.

8. Nakatani, H., Hajzargarbashi, T., Ito, K., Kundu, T., & Takeda, N. (2013). Locating point of impact on an anisotropic cylindrical surface using acoustic beamforming technique. In *Key Engineering Materials* (Vol. 558, pp. 331-340). Trans Tech Publications.

9. Seydel, R., & Chang, F. K. (2001). Impact identification of stiffened composite panels: I. System development. *Smart Materials and Structures*, *10*(2), 354-369.

10. Seydel, R., & Chang, F. K. (2001). Impact identification of stiffened composite panels: II. Implementation studies. *Smart materials and structures*, *10*(2), 370-379.

11. Meo, M., Zumpano, G., Piggott, M., & Marengo, G. (2005). Impact identification on a sandwich plate from wave propagation responses. *Composite structures*, *71*(3), 302-306.

12. Kurokawa, Y., Mizutani, Y., & Mayuzumi, M. (2005). Real-time executing source location system applicable to anisotropic thin structures. *Journal of Acoustic Emission*, *23*, 224-232.

13. Ciampa, F., & Meo, M. (2010). A new algorithm for acoustic emission localization and flexural group velocity determination in anisotropic structures. *Composites Part A: Applied Science and Manufacturing*, *41*(12), 1777-1786.

14. Ciampa, F., Meo, M., & Barbieri, E. (2012). Impact localization in composite structures of arbitrary cross section. *Structural Health Monitoring*, *11*(6), 643-655.

15. Kundu, T. (2012, July). A new technique for acoustic source localization in an anisotropic plate without knowing its material properties. In *6th European Workshop on Structural Health Monitoring* (pp. 3-6).

16. Kundu, T., Nakatani, H., & Takeda, N. (2012). Acoustic source localization in anisotropic plates. *Ultrasonics*, *52*(6), 740-746.

17. Tong, C., & Kennett, B. L. (1996). Automatic seismic event recognition and later phase identification for broadband seismograms. *Bulletin of the Seismological Society of America*, *86*(6), 1896-1909.

18. Baer, M., & Kradolfer, U. (1987). An automatic phase picker for local and teleseismic events. *Bulletin of the Seismological Society of America*, *77*(4), 1437-1445.

19. Kurz, J. H., Grosse, C. U., & Reinhardt, H. W. (2005). Strategies for reliable automatic onset time picking of acoustic emissions and of ultrasound signals in concrete. *Ultrasonics*, *43*(7), 538-546.

20. Ziola, S. M., & Gorman, M. R. (1991). Source location in thin plates using cross-correlation. *The Journal of the Acoustical Society of America*, *90*(5), 2551-2556.

21. Kosel, T., Grabec, I., & Kosel, F. (2003). Intelligent location of simultaneously active acoustic emission sources: Part I. *Aircraft Engineering and Aerospace Technology*, *75*(1), 11-17.

22. Dai, H., & MacBeth, C. (1997). The application of back-propagation neural network to automatic picking seismic arrivals from single-component recordings. *Journal of Geophysical Research: Solid Earth*, *102*(B7), 15105-15113.

23. Boschetti, F., Dentith, M. D., & List, R. D. (1996). A fractal-based algorithm for detecting first arrivals on seismic traces. *Geophysics*, *61*(4), 1095-1102.

24. Xu, J. (2011). P-wave onset detection based on the spectrograms of the AE signals. In *Advanced Materials Research* (Vol. 250, pp. 3807-3810). Trans Tech Publications.

25. Hinkley, D. V. (1971). Inference about the change-point from cumulative sum tests. *Biometrika*, *58*, 509-523.

26. Ciampa, F., & Meo, M. (2014). Impact localization on a composite tail rotor blade using an inverse filtering approach. *Journal of Intelligent Material Systems and Structures*, *25*(15), 1950-1958.

27. Ciampa, F., Boccardi, S., & Meo, M. (2016). Factors affecting the imaging of the impact location with inverse filtering and diffuse wave fields. *Journal of Intelligent Material Systems and Structures*, *27*(11), 1523-1533.

28. Akaike, H. (1973). Information theory and an extension of the maximum likelihood principle. In: BN Petrov, F Csaki, editors, *Second international symposium on information theory*, Springer-Verlag, 267-281.

29. Akaike, H. (1974). Markovian representation of stochastic processes and its application to the analysis of autoregressive moving average processes. *Annals of the Institute of Statistical Mathematics*, *26*(1), 363-387.

30. Akaike, H. (1974). A new look at the statistical model identification. *IEEE transactions on automatic control*, *19*(6), 716-723.

31. Kitagawa, G., & Akaike, H. (1978). A procedure for the modeling of non-stationary time series. *Annals of the Institute of Statistical Mathematics*, *30*(1), 351-363.

32. Yokota, T., Zhou, S., Mizoue, M., & Nakamura, I. (1981). An automatic measurement of arrival time of seismic waves and its application to an on-line processing system. *Bulletin of the Earthquake Research Institute*, *56*, 449-484.

33. Zhang, H., Thurber, C., & Rowe, C. (2003). Automatic P-wave arrival detection and picking with multiscale wavelet analysis for single-component recordings. *Bulletin of the Seismological Society of America*, *93*(5), 1904-1912.

34. Maeda, N. (1985). A method for reading and checking phase times in auto-processing system of seismic wave data. *Zisin*, *38*(3), 365-379.

35. Sleeman, R., & van Eck, T. (1999). Robust automatic P-phase picking: an on-line implementation in the analysis of broadband seismogram recordings. *Physics of the earth and planetary interiors*, *113*(1), 265-275.

36. Leonard, M., & Kennett, B. L. N. (1999). Multi-component autoregressive techniques for the analysis of seismograms. *Physics of the Earth and Planetary Interiors*, *113*(1), 247-263.

37. Sedlak, P., Hirose, Y., Khan, S. A., Enoki, M., & Sikula, J. (2009). New automatic localization technique of acoustic emission signals in thin metal plates. *Ultrasonics*, *49*(2), 254-262.

38. Sedlak, P., Hirose, Y., & Enoki, M. (2013). Acoustic emission localization in thin multi-layer plates using first-arrival determination. *Mechanical Systems and Signal Processing*, *36*(2), 636-649.

39. Carpinteri, A., Xu, J., Lacidogna, G., & Manuello, A. (2012). Reliable onset time determination and source location of acoustic emissions in concrete structures. *Cement and concrete composites*, *34*(4), 529-537.

40. Niccolini, G., Xu, J., Manuello, A., Lacidogna, G., & Carpinteri, A. (2012). Onset time determination of acoustic and electromagnetic emission during rock fracture. *Progress In Electromagnetics Research Letters*, *35*, 51-62.

41. Douglas, A. (1997). Bandpass filtering to reduce noise on seismograms: Is there a better way?. *Bulletin of the Seismological Society of America*, *87*(3), 770-777.

42. Allen, R. (1982). Automatic phase pickers: Their present use and future prospects. *Bulletin of the Seismological Society of America*, *72*(6B), S225-S242.

43. Paget, C. A., Atherton, K., & O'Brien, E. (2003, September). Triangulation algorithm for damage location in aeronautical composite structures. In *Proceedings of the 4th International Workshop on Structural Health Monitoring (F. Chang, ed.),(Stanford, CA, USA)* (pp. 363-370).

APPENDIX 1

As described in Section 2.1 the reference sensor equation is:

$$(x_1 - x_I)^2 + (y_1 - y_I)^2 = \left(t_1 V_g\right)^2 , \tag{A1}$$

and the final expressions for the four unknowns are:

$$\begin{cases} x_I = a_1 - {V_g}^2 c_1 \\ y_I = a_2 - {V_g}^2 c_2 \\ {V_g}^2 t_1 = a_3 - {V_g}^2 c_3 \end{cases} . \tag{A2}$$

The aim is to obtain a third order equation with t_1 or V_g as unknown. The following procedure considers the reference time t_1 as unknown.
Substituting (A2) in (A1) we obtain:

$$\left[x_1 - \left(a_1 - \frac{a_3}{t_1 + c_3} c_1\right)\right]^2 + \left[y_1 - \left(a_2 - \frac{a_3}{t_1 + c_3} c_2\right)\right]^2 = {t_1}^2 \frac{a_3}{t_1 + c_3} , \tag{A3}$$

that becomes, considering $t_1 + c_3 \neq 0$:

$$\begin{aligned} &\{x_1(t_1 + c_3) - a_1(t_1 + c_3) + a_3 c_1\}^2 \\ &\quad + \{y_1(t_1 + c_3) - a_2(t_1 + c_3) + a_3 c_2\}^2 \\ &\quad = {t_1}^2 (t_1 + c_3) a_3 . \end{aligned} \tag{A4}$$

After some mathematical manipulation, equation (A4) can be written as:

$$\begin{aligned} &-a_3 {t_1}^3 + {t_1}^2 [(a_1 - x_1)^2 - a_3 c_3 + (a_2 - y_1)^2] \\ &\quad + t_1 [-2(a_1 - x_1)(a_3 c_1 - a_1 c_3 + x_1 c_3) \\ &\quad - 2(a_2 - y_1)(a_3 c_2 - a_2 c_3 + y_1 c_3)] \\ &\quad + [(a_3 c_1 - a_1 c_3 + x_1 c_3)^2 + (a_3 c_2 - a_2 c_3 + y_1 c_3)^2] \\ &\quad = 0 , \end{aligned} \tag{A5}$$

or, in general, as reported below:

$$ {t_1}^3 Z_1 + {t_1}^2 Z_2 + t_1 Z_3 + Z_4 = 0 , \tag{A6}$$

where the complete expressions of Z_i coefficients in (A6) are:

$$Z_1 = -a_3 \,, \tag{A7}$$

$$Z_2 = (a_1 - x_1)^2 - a_3 c_3 + (a_2 - y_1)^2 \,, \tag{A8}$$

$$\begin{aligned} Z_3 = -2(a_1 - x_1)(a_3 c_1 - a_1 c_3 + x_1 c_3) \\ - 2(a_2 - y_1)(a_3 c_2 - a_2 c_3 + y_1 c_3) \,, \end{aligned} \tag{A9}$$

$$Z_4 = (a_3 c_1 - a_1 c_3 + x_1 c_3)^2 + (a_3 c_2 - a_2 c_3 + y_1 c_3)^2 \,. \tag{A10}$$

APPENDIX 2 (NOT PART OF THE PUBLISHED PAPER)

In this Appendix, a comparison between some characteristic functions (CFs) cited in Section 3.2.1 of the previous paper is performed.

The Hilbert transform of a generic signal $x(t)$ is given by [27, 28]:

$$H\{x(t)\} = \frac{1}{\pi}\, p.v. \int_{-\infty}^{+\infty} \frac{x(\tau)}{t - \tau} \,, \tag{A11}$$

and it is defined using the Cauchy principal value (denoted here by p.v.). The Hilbert transform of signal $x(t)$ can be thought of as the convolution of $x(t)$ with the function $h(t) = 1/(\pi t)$, known as the Cauchy kernel.

To explain the meaning of the envelope of a signal it is important to introduce the concept of "analytic signal". It is a complex-valued function that has no negative frequency components and can be expressed as [28]:

$$x_a = x(t) + j\, H\{x(t)\} \,. \tag{A12}$$

The envelope of the signal is the absolute value of the complex amplitude of (A11) and it is given by [29]:

$$Env\big(x(t)\big) = \sqrt{x(t)^2 + H\{x(t)\}^2} \,. \tag{A13}$$

A comparison among the Hilbert signal envelope and other CFs (see Section 3.2.1 of the previous paper) is depicted in Figure 10 and Figure 11, where the considered signal consists of a generic structural response recorded after a low-velocity impact and the squared envelope is simply the square of (A13).

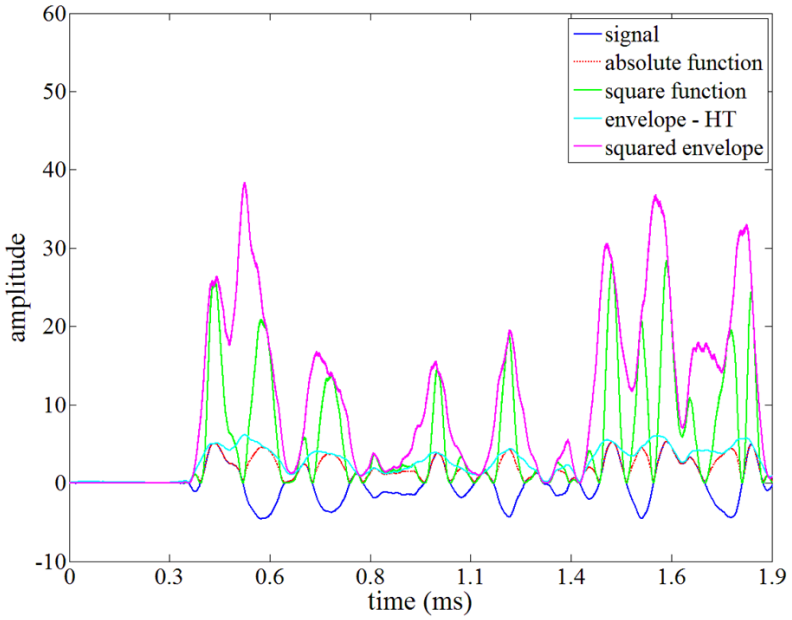

Figure 10. Characteristic functions visualisation.

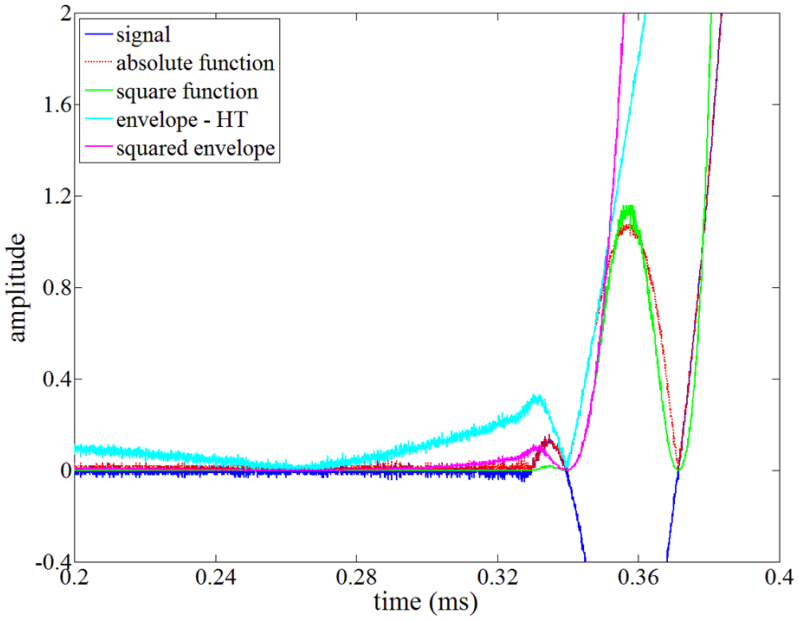

Figure 11. Characteristic functions focused on the initial part of the signal.

Due to the limitations of these functions (see Section 3.2.1 of the previous paper), a different characteristic function, called “Sedlak function” [30] and derived from “Allen function” [31], was used in the paper.

A comparison among the CFs is reported in Figure 12, where a “chirp signal” is considered:

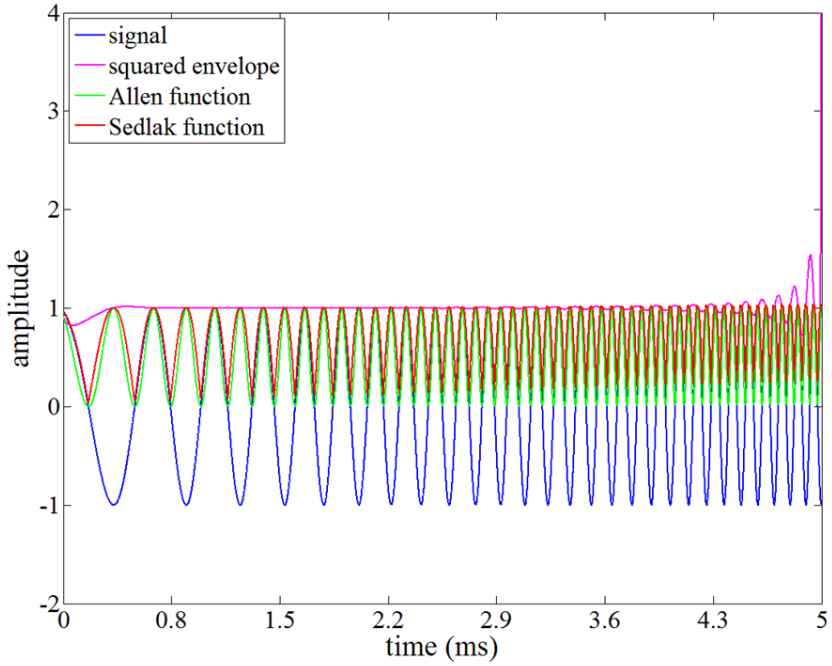

Figure 12. Characteristic functions of a “chirp signal”.

As described in Section 3.2.1 of the previous paper, the squared envelope is not suitable for this kind of signal, if compared to other reported CFs.

Chapter 4

Impact force reconstruction by using time reversal and radial basis functions

In Chapter 3 a method able to localise the coordinates of an impact event on an aeronautical component was developed and presented. However, it should be noted that an efficient prediction of damage occurrence on a structure could not ignore the impacting force amount. For this reason, the main achievement of the publication presented in this Chapter is to develop a suitable method able to furnish the reconstruction of impact force history in time domain.

The principal hypothesis for the developed method is that the components under investigation respect the linear relationship between the impact (the input) and the structural response (the output). The data are obtained by an initial calibration process, where a set of impacts are performed in numerous “calibration points”, arranging a grid on the specimen surface. The impact forces and the structural responses are collected respectively from an instrumented impact hammer and a sparse array of surface bonded receiving ultrasonic transducers.

At the end of the process, both the structural responses and the frequency response functions (also called “transfer functions” in the paper) between the calibration points and the transducer locations are available.

The developed method cannot ignore the location of the impact event, calculated in a totally different way with respect to the algorithm presented in Chapter 3, because of the presence of three far-from each other receiving sensors. Moreover, the necessity to create an initial baseline for the calculation and storing of the transfer functions, is perfect for the time reversal method. The algorithm developed in [21-23] was improved and applied in order to identify the cell on the structure, whose corners are a subset of the calibration points, where the impact event occurs. The coordinates of the impact event inside the detected cell are then calculated by a centre-of-gravity method.

It should be remarked that even if only one transducer could be employed for the acquisition of structural responses necessary for the time reversal method, three transducers are considered in the research work in order to avoid ambiguities in the identification of the right impact cell. Moreover, to consider average data coming from transducers covering a large monitoring zone on the structures, can provide better results also in transfer function computation.

The unknown transfer function in frequency domain between the calculated impact point and transducer locations is calculated by using a radial basis function interpolation approach, able to approximate functions or data only available at sparse locations with high level of accuracy [32]. Once obtained the interpolated and transfer functions at impact location and by knowing the structural responses due to the unknown impact, it is easy to calculate the averaged impact spectrum in frequency domain and then the time impact history.

It should be noted that in the following publication:

- despite it is reported a generic frequency response function as related to an impact point, it is well-known that the frequency response function is a mathematical representation of the relationship between the input and the output of the system, then it is not related only to the impact (input) point;
- strong nonlinear effects and damage presence due to the performed impacts are not considered.

The results obtained on a CFRP plate and an aluminium/CFRP composite wing stringer-skin panel confirmed the accuracy, reliability and robustness of both algorithms, for the impact localisation and reconstruction of the impact force.

The Statement of Authorship Form and the paper can be found next.

This declaration concerns the article entitled:	
A hierarchical method for the impact force reconstruction in composite structures	
Publication status (tick one)	
Draft manuscript	
Submitted	
In review	
Accepted	
Published	✓
Candidate's contribution to the paper (detailed, and also given as a percentage)	
The candidate contributed to/ considerably contributed to/predominantly executed the…	
Formulation of ideas:	80% I improved the time reversal idea for the impact localisation, furnished by my supervisors. I developed the idea to calculate the transfer functions after the calibration process and to interpolate them. The radial basis function interpolation approach was suggested by supervisors.
Design of methodology:	90% I designed/improved all the algorithms used in the localisation and force reconstruction methods. I designed the experimental tests, helped by my supervisors.

Experimental work:	90% I provided all the equipment (structural components, instrumented impact hammer and transducers). I collected all the data and evaluated all the algorithm outputs. My supervisors helped me in results interpretation.
Presentation of data in journal format:	90% I decided structure, wrote all drafts, prepared all figures. Supervisors provided feedback on drafts and helped with submission, responses to reviews and publication process.

Statement from Candidate			
This paper reports on original research I conducted during the period of my Higher Degree by Research candidature.			
Signed	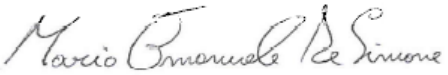	**Date**	26/06/2019

The following is the author accepted manuscript of: De Simone, ME, Ciampa, F & Meo, M 2019, A hierarchical impact force reconstruction method for Aerospace composites. in Key Engineering Materials: Advanced Materials for Defense. vol. 812, Scientific.net, pp. 17-24. t
The final published version is available online via: https://doi.org/10.4028/www.scientific.net/KEM.812.17

A hierarchical method for the impact force reconstruction in composite structures

Mario Emanuele DE SIMONE, Francesco CIAMPA, Michele MEO*

Mechanical Engineering Department, University of Bath, Bath, United Kingdom

* corresponding author: m.meo@bath.ac.uk

Keywords: Impact force reconstruction, time-reversal, radial basis functions, composite materials.

ABSTRACT

Impact damage is a major concern for new generation aircraft composite components due to their low impact resistance capabilities. The development of an impact location and force reconstruction algorithm would provide rapid and efficient prediction of damage occurrence, thus making structures safer and creating maintenance inspection procedures more efficient, thus saving time and costs. However, state-of-the-art impact force reconstruction algorithms use reference data from numerical simulations and require a detailed knowledge of mechanical properties, which are difficult to obtain under real operational conditions.

This paper presents a hierarchical impact force reconstruction algorithm that relies on experimental structural responses measured by a sparse array of surface bonded receiving ultrasonic transducers. This algorithm uses time reversal method to retrieve the location of an impact source and interpolation techniques based on hierarchical radial basis functions to calculate the transfer function at the impact point and reconstruct the impact force history. A number of impact testing were performed on a composite plate-like structure and a wing stringer-skin panel, and compared with impact force algorithms available in literature. Experimental results revealed that the proposed impact force reconstruction method was able to extrapolate the information associated with points far from the impact location and

determine the impact force history with high level of accuracy in a real aircraft structure. Since the proposed algorithm requires the calibration of transfer functions from a very sparse training set of data and it does not need numerical models of the component under investigation, it demonstrates its potential as a useful monitoring tool for impact force reconstruction in composite components for full-scale aircraft structural applications leading to timely and cost-efficient inspections.

1 INTRODUCTION

Composite materials exhibit desirable physical and chemical properties that include lightweight coupled with high stiffness and strength and, in the last few decades, have been widely used in many industrial sectors, from aerospace to civil and nuclear. However, composite structures may experience significant material degradation if impacted by low-velocity objects such as tool drops, runway debris and hail stones. Hence, in order to prevent serious and dangerous consequences due to micro-cracks and barely visible impact damage (BVID), a number of structural health monitoring (SHM) techniques capable of localising the impact source and reconstructing the force history (or energy) in composites have been investigated [1-3]. These SHM methods enhance the efficiency of current material inspection systems and enable the prediction of damage severity. The so-called “inverse approach” has been widely used for the determination of the force history in different materials and components. In this approach, the impact energy can be detected through the knowledge of structural responses acquired by a set of transducers surface bonded to the specimen [4]. However, the inverse approach leads to a deconvolution for numerical solutions, which is a well-known ill-posed mathematical problem that can be numerically unsolvable or, if the solution exists, can be instable for the presence of small disturbance such as noise. To overcome this issue, Doyle solved the inverse problem by using the fast Fourier transform method in both isotropic [5] and orthotropic [6] plates. However, this method needed cumbersome windowing and filtering processes in order to suppress the effect of wave reflection from the plate boundaries. Chang and Sun [7] proposed a

method suitable for composite structures based on the generation of the experimental Green's function using time signal deconvolutions. However, this technique was limited by (i) a scaling factor for the identification of the absolute amplitude of the Green's function and (ii) the short duration of responses that were characterised by a low signal-to-noise ratio. Wu et al. [8] utilised an optimisation method to reconstruct the time history of the impact force on a circular plate, which was subject to impact loading at its centre. In this work, Green's functions were generated from a series of Bessel functions. The authors also proposed an experimental method based on a deconvolution process, which did not provide accurate results when simultaneous impacts acted at multiple locations. The accuracy in reconstructing the impact force was further enhanced by developing an analytical method suitable for composite laminates [9], which was based on the classical lamination theory and the Rayleigh-Ritz equations. A detailed theoretical explanation of the deconvolution problem for impact force reconstruction and the regularisation methods for its solution was also presented by Jacquelin et al. [4]. Nevertheless, this approach required the determination of unknown regularisation parameters, as well as a-priori knowledge of mechanical properties, which is often difficult to obtain. Despite this limitation, several authors proposed algorithms based on regularisation techniques. Kalhori et al. [10, 11] proposed some research works based on l_2-norm-based regularisation methods (Tikhonov regularisation), whilst Qiao et al. [12, 13] and Pan et al. [14] presented methodologies based on l_1-norm regularisation. Moreover, Yan et al. [15] developed a two-loops algorithm based on the Bayesian interference regularisation and a nonlinear unscented Kalman filter (UKF), both applied to a state-space dynamic model of a composite plate under impact. Park et al. [16] introduced an inverse method based on a system identification technique able to establish a model constructed with transfer functions. This method is suitable for complex structures using a distributed sensor array. Chen et al. [17, 18] and Xu et al. [19] proposed a similar approach by using four transducers fixed on both isotropic and composite plates. A completely different approach for impact force reconstruction is based on the artificial neural network (ANN) method (see [20-24]), which consists of complex mathematical

models that can be trained with scattered data. However, due to the large amount of training data to be generated, the ANN approach is considered impractical for SHM applications.

The aim of this research work was to develop an impact force reconstruction method that relies on the structural responses measured by three surface bonded receiving sensors. The proposed algorithm was divided into two steps. In the first one, the impact localisation was achieved by using the time reversal (TR) method [25-28]. In the second step, an interpolation technique based on the hierarchical radial basis function (RBF) approach was used to calculate the transfer function at the impact location and reconstruct the impact force history [36]. Radial basis functions were here used as they are able to approximate functions or data with high level of accuracy, which are only available at sparse locations [37, 39, 40]. Moreover, one of the greatest advantages of this approach is related to its versatility in multi-dimensional applications. For their peculiar characteristics, radial basis functions are used in many fields including numerical finite element methods for the solution of partial differential equations [46], neural networks and machine learning [48, 51], statistical approximation [53], geophysical research [47], ultrasonic imaging [55] and engineering applications such as the analysis of orthotropic shells and boundary condition reconstruction on an elastic cavity [52]. In order to validate the proposed hierarchical impact force reconstruction algorithm, a number of experimental tests were performed on a composite plate and a wing stringer-skin panel. Moreover, further comparison with a method available in literature, namely the shape function (SF) interpolation technique [16], was performed. The outline of this research work is as follows: in Section 2, the impact localisation algorithm based on the time reversal method is described. The impact force reconstruction algorithm is presented in Section 3, whose main parts are the Section 3.1, where a suitable transfer function calculation method is presented, and the Section 3.2, whose topic is the interpolation trough the radial basis functions. Section 4 shows the set-up used to perform experimental tests, whilst in Section 5 all the results are illustrated. The conclusions of this paper are presented in Section 6.

2 IMPACT LOCALISATION – TIME REVERSAL METHOD

A number of impact localisation algorithms were developed for both isotropic and anisotropic media without requiring *a-priori* knowledge of the mechanical properties of the material [29-32]. In this work, the impact source localisation was the initial stage of the impact force reconstruction algorithm that, in turn, allowed reconstructing the impact force magnitude through information available in points close to the impact event. The TR method was here used for the impact localisation. TR is based on the hypothesis of time invariance and spatial reciprocity of elastodynamic wave equation and on the Huygens' Principle, through which it is possible to reconstruct the wave function in a generic volume by the knowledge of its sources located on a two-dimensional surface. A detailed theoretical explanation of TR method is presented in [25-27]. TR method is typically split into the "forward propagation" and the "backward propagation" steps. In the "forward" one, low-velocity impacts were applied in M excitation points, also called "calibration points", which were arbitrarily chosen on the plane of the structure (focusing plane) that identifies the monitoring zone. A number of N receiving sensors were used, so that a set of $N \times M$ signals was acquired and stored in the computer memory. These waveforms represent the response of the structure (e.g. displacements, velocities, strains, etc.) subject to impact loading. With the hypothesis of free unbounded space and assuming that the wave field, $u(\boldsymbol{r}, t)$, can be measured at any point of a closed surface S, the general solution of the elastodynamic wave equation is:

$$u(\boldsymbol{r}, t) = \iiint_{\Omega} [G(\boldsymbol{r}, t;\, \boldsymbol{r}_0) \otimes p(\boldsymbol{r}_0, t)]\, d\Omega_0 \,, \tag{1}$$

where $\otimes$ represents a convolution over time, $p(\boldsymbol{r}_0, t)$ indicates an impulsive force located in $\boldsymbol{r}_0$ and $G(\boldsymbol{r}, t;\, \boldsymbol{r}_0)$ is the Green space-time function. If the excitation function is a Dirac delta function (unit impulse function), the Green function is called "impulse response" and it is equal to the measured wave field.

As aforementioned, the surface of the structure was divided into a discrete domain composed of M excitation points, so that Eq. (1) can be re-written as:

$$u(\boldsymbol{r},t) = \sum_{m=1}^{M} G(\boldsymbol{r},t;\,\boldsymbol{r}_m) \otimes p(\boldsymbol{r}_m,t) = \sum_{m=1}^{M} \left[\int_0^t G(\boldsymbol{r},t-\tau;\,\boldsymbol{r}_m)\, p(\boldsymbol{r}_m,\tau)\, d\tau \right], \tag{2}$$

where τ is the time lag. It should be noted that only if the structure deformation are considered linearly elastic and small enough to neglect geometric nonlinearities, the relationship between the impact force and the response of the structure can be considered as linear and mathematically described by the linear convolution reported in Eq. (2). The "backward propagation step" consisted of correlating the waveform emitted by a point of unknown position $\boldsymbol{r}_{m0}$ with all the impulse responses stored in the "forward propagation" step. It can be demonstrated (see for instance [25-27]) that the impact location is calculated as the maximum of the following time reversal operator (i.e. when $\boldsymbol{r}_m = \boldsymbol{r}_{m0}$):

$$R_{TR} = G(\boldsymbol{r}_m,t;\,\boldsymbol{r}) \otimes G(\boldsymbol{r},-t;\,\boldsymbol{r}_{m0}) = \int_0^t G(\boldsymbol{r}_m,t;\,\boldsymbol{r})\, G(\boldsymbol{r},t+\tau;\,\boldsymbol{r}_{m0})\, d\tau\,, \tag{3}$$

which represents a cross correlation operation. The Cauchy-Schwarz inequality proves that [33]:

$$|R_{TR}|^2 = \left| \int_0^t G(\boldsymbol{r}_m,t;\,\boldsymbol{r})\, G(\boldsymbol{r},t+\tau;\,\boldsymbol{r}_{m0})\, d\tau \right|^2 \leq \int_0^t |G(\boldsymbol{r}_m,t;\,\boldsymbol{r})|^2\, d\tau \int_0^t |G(\boldsymbol{r},t+\tau;\,\boldsymbol{r}_{m0})|^2\, d\tau\,, \tag{4}$$

where $|\cdot|$ is the absolute value. Eq. (4) is equivalent to:

$$|R_{TR}| \leq \left(\int_0^t |G(\boldsymbol{r}_m,t;\,\boldsymbol{r})|^2\, d\tau \right)^{\frac{1}{2}} \left(\int_0^t |G(\boldsymbol{r},t+\tau;\,\boldsymbol{r}_{m0})|^2\, d\tau \right)^{\frac{1}{2}}. \tag{5}$$

The Euclidean norm is defined as:

$$\|G(\boldsymbol{r}_m, t;\, \boldsymbol{r})\| = \left(\int_0^t |G(\boldsymbol{r}_m, t;\, \boldsymbol{r})|^2 \, dt \right)^{\frac{1}{2}}. \tag{6}$$

The signal energy is defined as:

$$E_{G\boldsymbol{r}_m} = \int_0^t |G(\boldsymbol{r}_m, t;\, \boldsymbol{r})|^2 \, dt \,. \tag{7}$$

Comparing Eqs. (6) and (7), Eq. (5) becomes:

$$|R_{TR}| \leq \|G(\boldsymbol{r}_m, t;\, \boldsymbol{r})\| \, \|G(\boldsymbol{r}, t+\tau;\, \boldsymbol{r}_{m0})\| = \sqrt{E_{G\boldsymbol{r}_m} \, E_{G\boldsymbol{r}_{m0}}} \,. \tag{8}$$

As a measure of similarity of two signals, the correlation coefficient was used, which is defined as:

$$c_{TR} = max\left(\frac{|R_{TR}|}{\sqrt{E_{G\boldsymbol{r}_m} \, E_{G\boldsymbol{r}_{m0}}}} \right). \tag{9}$$

The expression (9) satisfies the inequality $0 \leq c_{TR} \leq 1$. The c_{TR} coefficient is close to one when the signals are similar (i.e. at the true impact location), whilst it is close to zero elsewhere. In order to compensate the incoherent measurement noise due to electronics, an average from the contribution of the N receiving sensors was here used, and a single mean correlation coefficient was related to each grid node. According to Figure 1, each cell of the grid on the monitoring zone is identified by four nodes and it was possible to perform a further mean among the correlation coefficients associated to each node in order to calculate a global correlation coefficient of the cell, indicated as c_{TR_GLOBAL}.

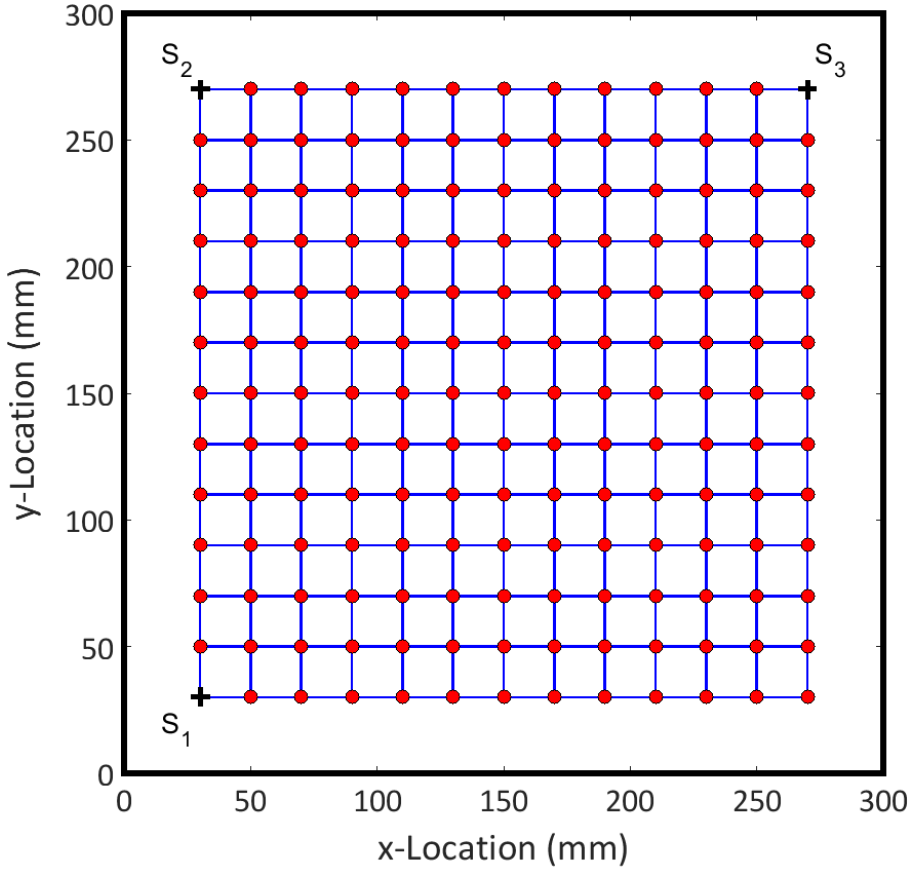

Figure 1. Initial surface grid. Calibration points are depicted as red spots.

The cell where c_{TR_GLOBAL} was maximum was regarded as the cell including the unknown impact point and here named as the "impact cell". The described TR approach is depicted in Figure 2. The impact coordinates were estimated by a centre-of-gravity method, in a similar way to [18, 19]:

$$x_I = \frac{\sum_{i=1}^{4} x_i \, c_{TR_i}}{\sum_{i=1}^{4} c_{TR_i}}, \qquad y_I = \frac{\sum_{i=1}^{4} y_i \, c_{TR_i}}{\sum_{i=1}^{4} c_{TR_i}}, \tag{10}$$

where x_i and y_i are the coordinates of the i^{th} node of the impact cell, c_{TR_i} is the averaged correlation coefficient related to the i^{th} node, x_I and y_I are the estimated locations of the current impact event.

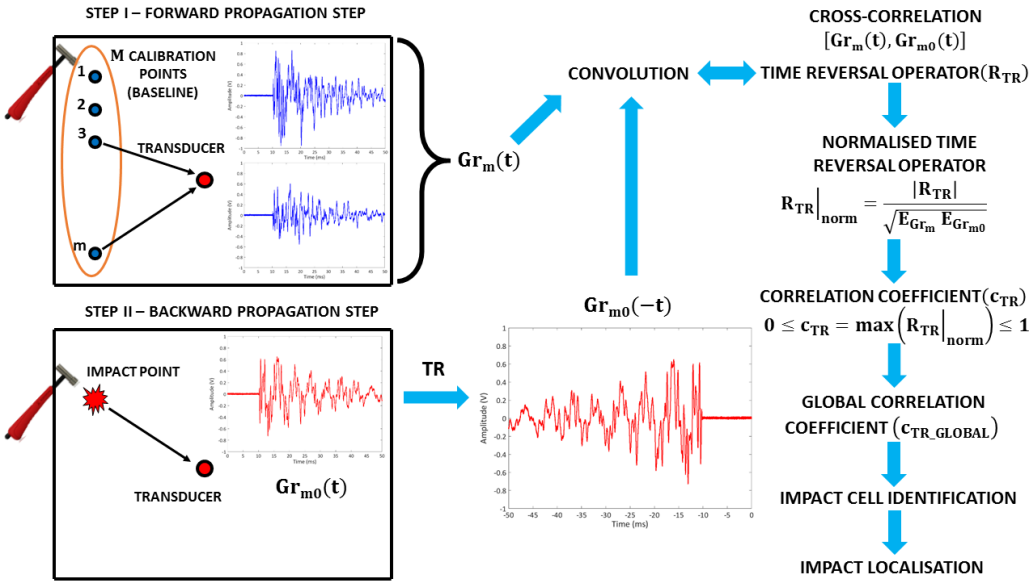

Figure 2. Graphical illustration of both "forward" and "backward" steps in the time reversal process for impact localisation.

3 IMPACT FORCE RECONSTRUCTION

For the impact force reconstruction, an impact force $p(t)$ acting on the surface of a specimen and the structural response $u(t)$ acquired by a transducer fixed to the specimen were considered. From a signal processing perspective, Eq. (1) mathematically represents a linear convolution between two arbitrary signals, so it can be rewritten as:

$$u(t) = (G \otimes p)(t) = \int_0^t G(t-\tau)\, p(\tau)\, d\tau\,. \tag{11}$$

The aim of this research work was to recover the impact force from Eq. (11). As described in [4], a discrete problem must be solved by transforming the convolution integral [Eq. (11)] into a system of algebraic equations expressed in the following matrix form:

$$[u] = [G]\,[p]\,, \tag{12}$$

where $[u]$ is the response vector $n \times 1$, $[p]$ is the force vector of dimensions $n \times 1$ and $[G]$ is the transfer matrix of dimensions $n \times n$, where n is the number of samples of acquired signals. The recovering of impact forces in Eq. (11) identifies an "inverse problem", known as "deconvolution problem", which is a well-known ill-posed system of equations with the $[G]$ matrix ill-conditioned. In order to overcome the difficulties related to a deconvolution problem in time domain, the frequency response function (FRF) of the impulsive structural response was considered. Indeed, according to the convolution theorem [34], the convolution of two time signals corresponds to a simple product of their spectra in the Fourier domain:

$$u(t) = (G \otimes p)(t) = \int_0^t G(t-\tau)\, p(\tau)\, d\tau \Rightarrow U(f) = H(f) \cdot P(f)\,, \qquad (13)$$

where $H(f)$ is the Fourier transform of the Green space-time function $G(t)$, indicated as the transfer function in the next sections. By following the TR process for impact localisation described in Section 2, the impact force reconstruction algorithm was divided into the following three steps:

1. the calculation of transfer function at each calibration point;
2. the hierarchical interpolation of transfer functions associated with a sparse array of points close to the identified impact location;
3. the impact force identification by using the estimated transfer function at impact location.

The description of these three steps is provided in the following sub-sections.

3.1 TRANSFER FUNCTION CALCULATION

An experimental method for the calculation of transfer function at each calibration point was here employed to prevent the use of approximated analytical and numerical models of the sample under investigation, which may poorly reconstruct the transfer function of the structure. This is the common case of components with

complex geometries or when material properties are not available [35]. The identification of the transfer function is based on the cross-correlation function between the acquired response and the impact force, which is expressed by:

$$S_{up}(f) = U(f) \cdot P^*(f) \,. \tag{14}$$

By inserting Eq. (13) into Eq. (14), yields:

$$S_{up}(f) = H(f) \cdot \, P(f) \cdot \, P^*(f) \,. \tag{15}$$

The auto-spectrum of the impact force is defined as:

$$S_{pp}(f) = P(f) \cdot \, P^*(f) = |P(f)|^2 \,, \tag{16}$$

therefore, Eq. (15) becomes:

$$S_{up}(f) = H(f) \cdot \, S_{pp}(f) \,, \tag{17}$$

and the transfer function, component by component, is calculated as reported below:

$$H(f_i) = \frac{S_{up}(f_i)}{S_{pp}(f_i)} \,. \tag{18}$$

Other studies consider the transfer function as the ratio between the auto-spectra of response and impact force, which represents only the modulus of the transfer function that does not contain any information on the phase of the system. Conversely, the described approach provides both module and phase of transfer function [35]. If nonlinear effects would not be negligible, the transfer functions associated to impacts with different energies could be calculated and the resulting average would be regarded as the transfer function of the system. However, this case was not investigated in the presented research work. At the end of the process a number of N transfer functions are available at each calibration point. Figure 3 shows an example of transfer function calculation from one of the calibration points.

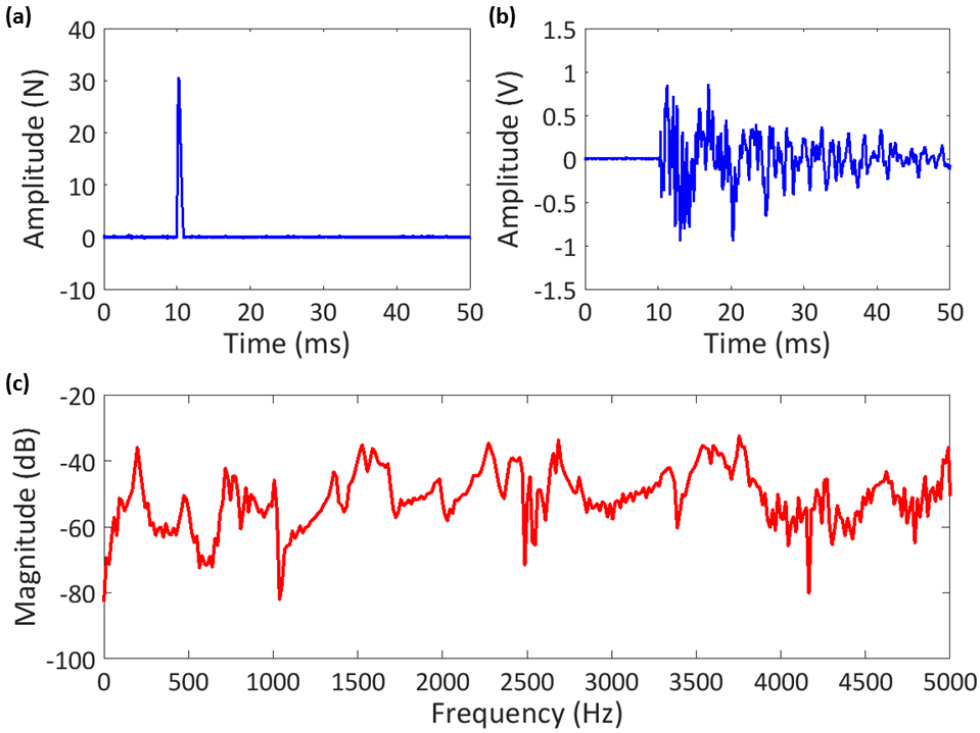

Figure 3. Transfer function calculation by using a single transducer: impact force (a); acquired response (b); calculated transfer function in the frequency domain (c).

3.2 RADIAL BASIS FUNCTION 2D INTERPOLATION

As described in Section 2, it was possible to identify the impact location using the TR method [Eq. (10)]. The transfer function at the impact location can then be obtained by using an interpolation of transfer functions associated with the cell whose vertices are the four calibration points surrounding the impact location. In this regard, Park et al. firstly proposed the shape function (SF) method, which uses polynomial interpolating functions (also known as shape functions) to reconstruct the impact force ([16-19]). The main idea of the SF technique is to relate the cell with a regular element of the same topology, whose edges have a non-dimensional length (see Figure 4).

The corresponding nodes in this parametric space have coordinates (ξ, η) and the transfer function at impact location in frequency domain can be expressed by:

$$\bar{H}_{(x_I,y_I)} = \sum_{i=1}^{4} \lambda_i \, H_i \, , \tag{19}$$

where H_i is the transfer function at i^{th} point of the physical cell and λ_i are the basis functions linking the physical and parametric coordinates. For two-dimensional bilinear interpolation, these functions are given by [16]:

$$\begin{aligned} \lambda_1(\xi,\eta) &= (1-\xi)(1-\eta) \\ \lambda_2(\xi,\eta) &= \xi\,(1-\eta) \\ \lambda_3(\xi,\eta) &= (1-\xi)\,\eta \\ \lambda_4(\xi,\eta) &= \xi\,\eta \end{aligned} \tag{20}$$

where it is $\xi = \frac{x-x_1}{x_2-x_1}$ and $\eta = \frac{y-y_1}{y_3-y_1}$.

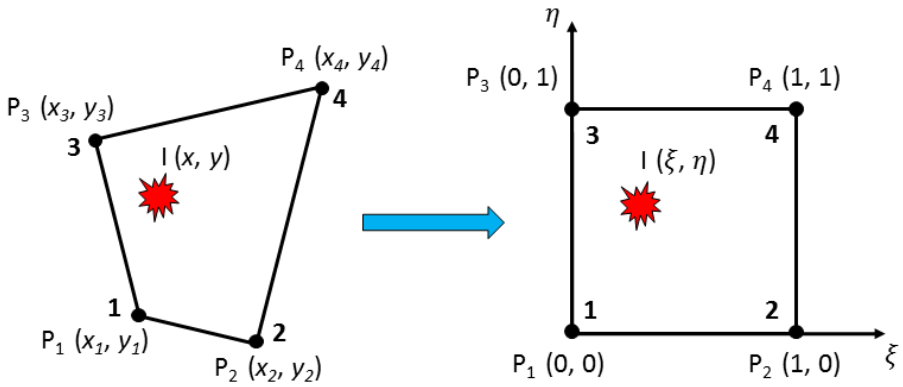

Figure 4. Illustration of the shape function (SF) interpolation method.

The SF method needs information related to four points close to the impact event. However, the higher is the distance from the impact event, the larger would the interpolation error.

To overcome this issue, in this paper a different interpolation method was used, which is based on the hierarchical radial basis functions (RBF) approach, analysed and developed in several research works. A detailed theoretical explanation of the RBF approach was presented by Wright [49]. The general idea of the RBF method

is that for a given set of n data points $\{x_j\}_{j=1}^{n}$ and corresponding data values $\{f_j\}_{j=1}^{n}$, a set of basis functions $\{\psi_j(x)\}_{j=1}^{n}$ is chosen such that a linear combination of these functions satisfies the interpolation conditions. For a one-dimensional function $s(x)$ it is possible to write:

$$s(x) = \sum_{j=1}^{n} \lambda_j \, \psi_j(x) \,, \tag{21}$$

where λ_j are the expansion coefficients, determined by solving a linear system of equations based on the interpolation conditions $s(x_j) = f_j$ for $j = 1, \dots, n$. Many types of basis functions ensure this system is non-singular when the data points $\{x_j\}_{j=1}^{n}$ are distinct. In the case of one-dimensional data, a number of techniques such as the polynomial and Fourier interpolation are able to solve the described problem [56]. Conversely, these interpolation techniques are not suitable if data in more than one dimension are considered, so that the described approach is doomed to fail because the linear system of equations for determining the expansion coefficients becomes singular (according to the Haar's theorem [36]). This non-singularity problem can be overcome by creating an interpolating function approach that uses a linear combination of translates of a single basis function radially symmetric about its centre. This approach is referred to as the RBF method. This is a generalised version of the multiquadric (MQ) method, developed previously by Hardy [38] and then by Carlson [44] and Foley [45], for solving problems of topographic surface reconstruction from a set of sparse and scattered measurements from some source points. The general form of MQ interpolant in d dimensions is expressed by:

$$s(\boldsymbol{x}) = \sum_{j=1}^{n} \lambda_j \sqrt{c^2 + \left\|\boldsymbol{x} - \boldsymbol{x}_j\right\|^2} \,, \qquad \boldsymbol{x}, \boldsymbol{x}_j \in \mathbb{R}^d \,, \tag{22}$$

where $\|\cdot\|$ denotes the Euclidean norm and $c \neq 0$ is a constant, introduced by Hardy for circular hyperboloid basis functions. The expansions coefficients λ_j are

determined from the interpolation conditions $s(\boldsymbol{x_j}) = f_j$ for $j = 1, \dots, n$. Micchelli demonstrated the method was unconditionally non-singular, also when a number of other basis functions are used, that, because of the radial symmetry about their centre, were called "radial basis functions" [41]. The basic RBF method can be expressed by the following interpolant:

$$s(\boldsymbol{x}) = \sum_{j=1}^{n} \lambda_j \, \phi\left(\left\|\boldsymbol{x} - \boldsymbol{x}_j\right\|\right), \qquad \boldsymbol{x}, \boldsymbol{x}_j \in \mathbb{R}^d, \tag{23}$$

where $\phi(r)$, $r \geq 0$, is some radial function. As described above, the expansions coefficients λ_j are determined from the interpolation conditions $s(\boldsymbol{x_j}) = f_j$ for $j = 1, \dots, n$, which leads to the following symmetric linear system:

$$[A][\lambda] = [f], \tag{24}$$

where the entries of A matrix are given by $a_{j,k} = \phi\left(\left\|\boldsymbol{x_j} - \boldsymbol{x}_k\right\|\right)$. Many radial basis functions are present in literature; some common examples of $\phi(r)$ are reported in Table 1 (see [50]).

Table 1. Some common types of radial basis functions.

Radial function $\phi(r), r \geq 0$	**Name**
Piecewise Smooth	
$r^{2n-1}, \ \ n = 1, 2, 3, \dots$	Powers (linear, cubic, quantic, …)
$r^{2n} \ln r, \ \ n = 1, 2, 3, \dots$	Thin Plate Splines (TPS)
Infinitely Smooth	
$\dfrac{1}{1 + (\varepsilon r)^2}$	Inverse Quadratic (IQ)
$\sqrt{1 + (\varepsilon r)^2}$	Multiquadric (MQ)
$e^{-(\varepsilon r)^2}$	Gaussian (GA)

The thin plate spline (TPS) was used as radial basis function, whose kernel is $\phi(r) = r^2\, ln(r)$. This function was selected for its peculiar characteristics, as a smooth interpolation can be achieved with derivatives of any order and there are no free parameters requiring manual tuning. Furthermore, there is a physical analogy involving the bending of a thin sheet of metal, because TPS is able to minimise the so-called "bending energy" [43]. Due to some stability issues, it is possible to consider additional polynomial terms to Eq. (23). The augmented RBF method can be expressed by the following interpolant:

$$s(\boldsymbol{x}) = \sum_{j=1}^{n} \lambda_j\, \phi\left(\left\|\boldsymbol{x} - \boldsymbol{x}_j\right\|\right) + \sum_{k=1}^{L} \gamma_k\, p_k(\boldsymbol{x})\,, \qquad \boldsymbol{x}, \boldsymbol{x}_j \in \mathbb{R}^d\,, \tag{25}$$

where $\{p_k(\boldsymbol{x})\}_{k=1}^{L}$ is a basis for $\prod_l(\mathbb{R}^d)$, that is the space of all *d*-variate polynomials that have degree less than or equal to l and whose dimension is $L = \binom{d+l}{d}$. To account for the conditions from the additional polynomial terms, the following constraints are applied:

$$\sum_{j=1}^{n} \lambda_j\, p_k\left(\boldsymbol{x}_j\right) = 0\,, \qquad k = 1, 2, \dots, L\,. \tag{26}$$

The expansions coefficients λ_j and γ_k are determined from the interpolation conditions and the constraints (26), which lead to the following symmetric linear system [54, 55] :

$$\begin{bmatrix} A & P \\ P^T & 0 \end{bmatrix} \begin{bmatrix} \lambda \\ \gamma \end{bmatrix} = \begin{bmatrix} f \\ 0 \end{bmatrix}, \tag{27}$$

where A is the $n \times n$ matrix presented in (24) and P is the $n \times L$ matrix with entries $p_k\left(\boldsymbol{x}_j\right)$ for $j = 1, \dots, n$ and $k = 1, \dots, L$. The Micchelli's theorem [42] admit that the augmented RBF method is uniquely solvable for the cubic and TPS RBFs when $l = 1$ and the conditions on the data points $\left\{\boldsymbol{x}_j\right\}_{j=1}^{n}$ are satisfied. With $l = 1$ and considering a two-dimensional approach ($d = 2$), a constant and linear polynomial is considered ($L = 3$), which leads the following RBF interpolant:

$$s(x,y) = \sum_{j=1}^{n} \lambda_j \, \phi\left(\sqrt{\left(x - x_j\right)^2 + \left(y - y_j\right)^2}\right) + \gamma_o + \gamma_1 x + \gamma_2 y \,. \qquad (28)$$

In this paper, RBF interpolant (28) is used for the transfer functions interpolation. As first step the expansion coefficients λ_j and γ_k are calculated by solving the linear system of equations (29), where the f values are the known values of the transfer functions in an arbitrary set of calibration points. Then, they are used for the calculation of the unknown transfer function value at the impact location. This process needs to be performed for all samples of the transfer function.

$$\begin{bmatrix} \phi_{1,1} & \dots & \phi_{1,n} & x_1 & y_1 & 1 \\ \vdots & \ddots & \vdots & \vdots & \vdots & \vdots \\ \phi_{n,1} & \dots & \phi_{n,n} & x_n & y_n & 1 \\ x_1 & \dots & x_n & 0 & 0 & 0 \\ y_1 & \dots & y_n & 0 & 0 & 0 \\ 1 & \dots & 1 & 0 & 0 & 0 \end{bmatrix} \begin{bmatrix} \lambda_1 \\ \vdots \\ \lambda_n \\ \gamma_1 \\ \gamma_2 \\ \gamma_o \end{bmatrix} = \begin{bmatrix} f_1 \\ \vdots \\ f_n \\ 0 \\ 0 \\ 0 \end{bmatrix}. \qquad (29)$$

3.3 IMPACT FORCE IDENTIFICATION

The interpolation algorithm described in Section 3.2 was performed by considering the N transfer functions available at each calibration point. Once obtained the N transfer functions at impact location, it was possible to calculate the N spectra of impact force through Eq. (13). The impact force in time domain was calculated by the inverse Fourier transform of the average impact spectrum as expressed by the following expression [19]:

$$p(t) = \mathcal{F}^{-1}\left\{\frac{P(f)|_1 + P(f)|_2 + P(f)|_3}{3}\right\}, \qquad (30)$$

where $P(f)|_N$ is the spectrum of the impact force calculated by using signals acquired by the N^{th} receiving sensor.

4 EXPERIMENTAL SET-UP

To validate the described algorithms, experimental impact tests were conducted on two specimens:

- a carbon fibre reinforced plastic (CFRP) plate with dimensions of $300 \times 300 \times 4\ \mathrm{mm}^3$ and lay-up sequence of $[45/\text{-}45/90/0]_{2S}$ (see Figure 5);
- an aluminium/CFRP composite wing stringer-skin panel provided by the courtesy of Airbus UK with dimensions of $3000 \times 1000 \times 4\ \mathrm{mm}^3$ (see Figure 6).

The impacts were generated by using a hand-held instrumented impact hammer (sensitivity factor $= 2.215\ \mathrm{mV/N}$) connected to a signal conditioner both manufactured by Meggit-Endevco. Two different arrangements of three receiving sensors were chosen, in order to demonstrate the validity of the described approach independently from the transducer locations:

- three surface-bonded piezoelectric transducers (PIC 255) with diameter of 6.5 mm and thickness of 0.3 mm were used and located at corners of the CFRP plate;
- three acoustic emission transducers with 150 kHz central frequency provided by the courtesy of Airbus UK.

The Cartesian reference frame was chosen with the origin at the bottom left corner of both the CFRP plate and the wing panel, where the monitoring area consists of a grid arranged with equally spaced nodes, which are the calibration points of the proposed TR algorithm. The spacing between them is 20 mm in both samples under investigation. The signals were acquired using a four-channel oscilloscope with 16 bits of resolution, a sampling rate of 2 MHz and an acquisition window of 50 ms. All algorithms were implemented by the authors by using a MATLAB software code. The experimental set-up is showed in Figure 5 and Figure 6 with sensor coordinates reported in Table 2.

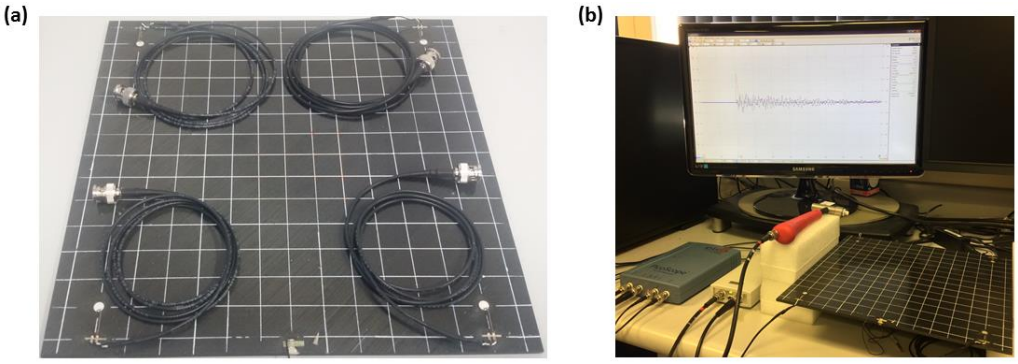

Figure 5. CFRP composite plate (a) and experimental set-up (b).

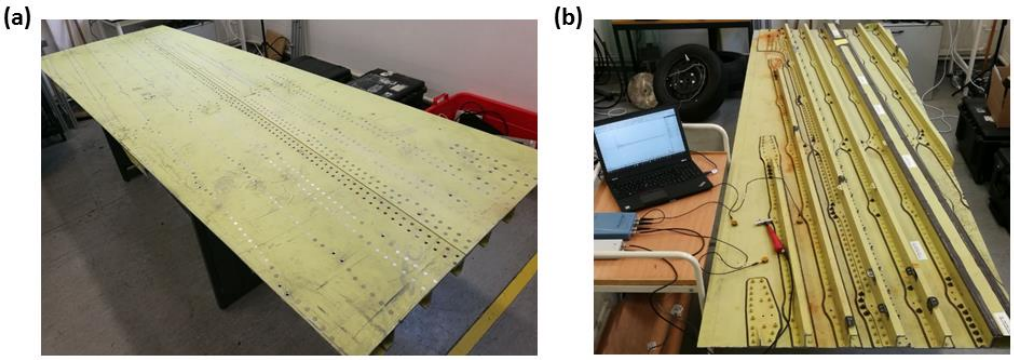

Figure 6. Wing stringer-skin panel: top view (a) and bottom view (b).

Table 2. Sensor coordinates on both specimens.

	CFRP plate		Wing panel	
	x-Coord (mm)	y-Coord (mm)	x-Coord (mm)	y-Coord (mm)
Sensor 1	30	30	30	30
Sensor 2	30	270	30	270
Sensor 3	270	270	270	150

5 RESULTS

The result section will be divided in three sub-sections: in Section 5.1 the impact localisation results on both specimens obtained with time reversal will be shown and discussed, whilst Sections 5.2, 5.3 and 5.4 report the impact force histories, calculated by using both the radial basis function and shape function interpolation methods. For these three sub-sections, three different sets of calibration points are considered:

- Set 1, which consists of the four closest to impact location calibration points. These points represent the corners of an impact cell with dimension 20×20 mm^2 used for both interpolation methods;
- Set 2, which consists of four calibration points far from the impact location. These points represent the corners of an impact cell with dimension 60×60 mm^2, used for both interpolation methods;
- Set 3, in which we suppose that the information related to the four closest to impact location calibration points are not available. For the SF interpolation method, eight far points arranged in two impact cells are considered, whilst twelve points equally disposed in a square around the impact location are used for the RBF interpolation method.

The accuracy of the impact localisation method is expressed by the following formula for the location error Ψ [57]:

$$\Psi = \sqrt{(x_{real} - x_{calculated})^2 + (y_{real} - y_{calculated})^2}\,, \tag{31}$$

where (x_{real}, y_{real}) are the coordinates of the true impact position and $(x_{calculated}, y_{calculated})$ are the coordinates of the impact location using the TR algorithm. Several methods can be also used to estimate the accuracy of the force reconstruction algorithms.

In this paper, an error based on time integral of the force is considered that is given by the following equation [35]:

$$\Gamma = \frac{\int_{t_1}^{t_2} |p_{real}(t) - p_{reconstructed}(t)|\, dt}{\int_{t_1}^{t_2} p_{real}(t)\, dt}, \tag{32}$$

where $T = t_2 - t_1$ is an interval of the recording, which includes the impact force. By experimentally observing the time histories of measured data, two time intervals surrounding the impact peak were here used, i.e. 1 ms and 3 ms.

It will be shown that the impact forces reconstructed by using the two different interpolation methods are exactly the same under the assumption that the same set of four interpolation points is used. As aforementioned in the Section 3.2, the RBF interpolation method overcomes the limitation of considering only four points and provides more accurate results by using the available information related to points far from the impact source.

5.1 IMPACT LOCALISATION RESULTS

The initial calibration process at each grid point was performed, considering the same (constant) amplitude of the impact forces generated with the instrumented hammer. Therefore, information associated with impact force histories and structural responses acquired by the three receiving sensors were known. The three transfer functions at each grid point were calculated through the method described in Section 3.1. A set of impact tests were performed on the two specimens at arbitrary locations. Figure 7, Figure 8 and Table 3 show the real impact location and that calculated by the TR algorithm on both specimens (see Section 2). The four nodes of the impact cells depicted in Figure 7 and Figure 8 represent the set 1 and their coordinates are presented in Table 3.

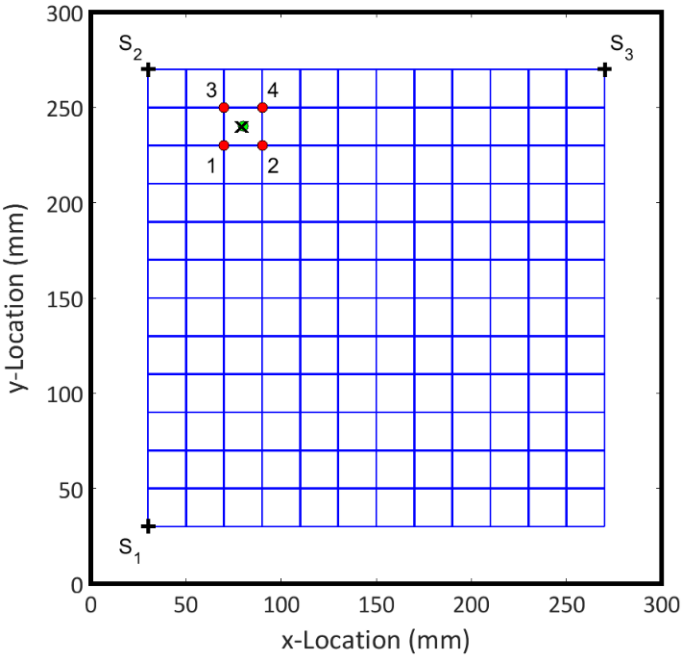

Figure 7. Source location on the CFRP plate by using time reversal method. The actual impact location is shown as a green circle, whilst the calculated one is shown as a cross (×). The set 1 is shown with red circles.

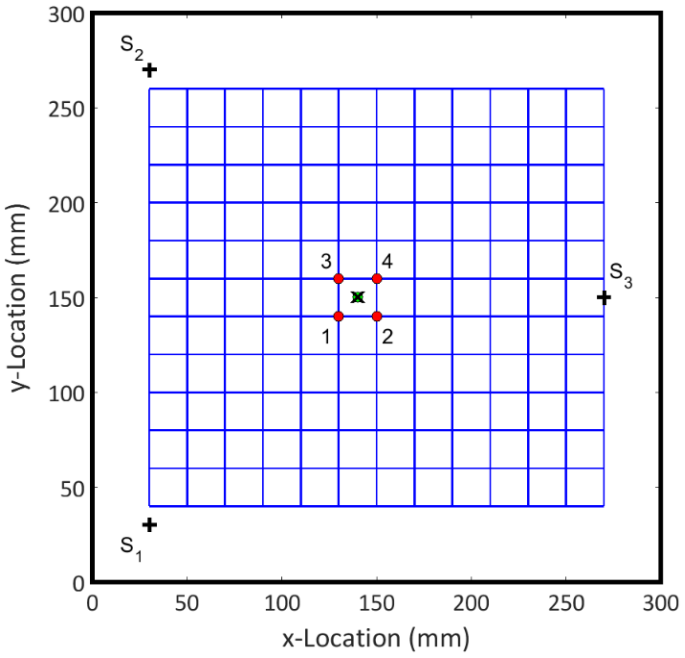

Figure 8. Source location on a portion of the wing panel by using time reversal method. The actual impact location is shown as a green circle, whilst the calculated one is shown as a cross (×). The set 1 is shown with red circles.

Table 3. Coordinates of set 1 of interpolation points, impact positions and errors on both specimens.

	CFRP plate		Wing panel	
	x-Coord (mm)	y-Coord (mm)	x-Coord (mm)	y-Coord (mm)
Node 1	70	230	130	140
Node 2	90	230	150	140
Node 3	70	250	130	160
Node 4	90	250	150	160
Current impact	80	240	140	150
Calculated impact	79.42	239.91	140.13	150.16
Location error Ψ (mm)	0.59		0.21	

Since the main purpose of this paper was to illustrate the performance of the proposed force reconstruction algorithm using hierarchical functions, only one impact location is reported in Figure 7 and Figure 8 for clarity reasons. In reality, more than fifty impacts were applied on both samples, showing great accuracy for all of them. However, by using a spacing of 20 mm between nodes and considering a high number of impact events (more than 50) at different positions along the plane of the specimens, location errors were always less than 1 mm. For further information about the efficiency and accuracy of TR, please refer to other papers from the same group (e.g. [25-27]) and from other authors (e.g. [28]).

5.2 IMPACT FORCE RECONSTRUCTION RESULTS – SET 1 OF CALIBRATION POINTS

Figure 9 shows the transfer functions related to set 1 on the CFRP plate. Three transfer functions are available at each node, therefore the average transfer function associated with each node is presented in the following figure.

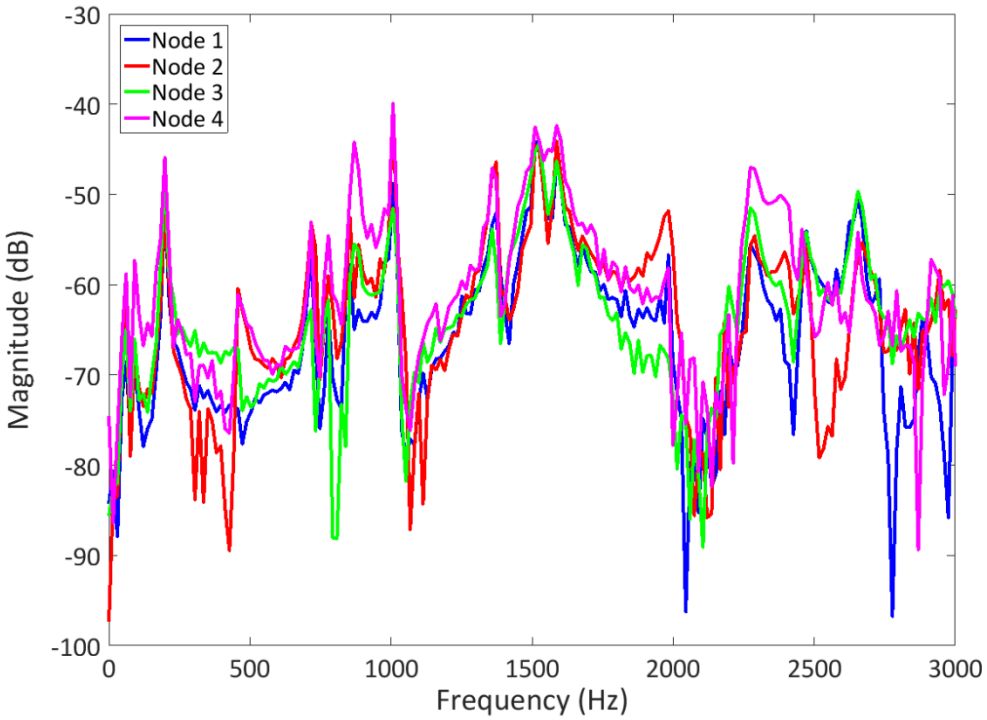

Figure 9. Transfer functions calculated at nodes of the impact cell (set 1) on the CFRP plate.

The interpolation process was performed three times since three sets of transfer functions were available at each node of the impact cell. Figure 10, related to the CFRP plate, depicts the comparison between the average transfer function at impact location calculated during the initial calibration process, and the interpolated ones obtained by using both the SF and the proposed RBF interpolation methods, averaged over the three receiving sensors.

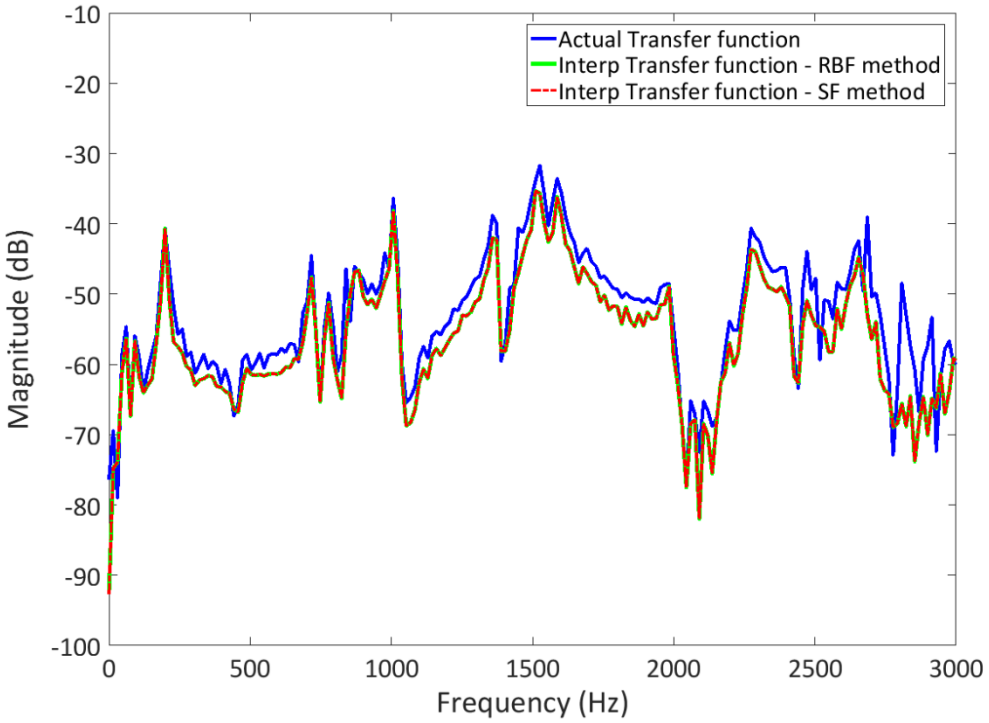

Figure 10. Comparison between the actual transfer function and the interpolated ones at the impact location on the CFRP plate.

As showed in Figure 10 the transfer functions calculated with the two interpolation methods are the same. Moreover, because of interpolation points are very close to the impact location, both interpolated results presented a negligible difference with the original transfer function. This assertion can be deducted also by considering Figure 11 and Figure 12, which present the comparison between the current impact force history and the reconstructed ones for the set 1 on both specimens and the signals acquired by all the receiving sensors (see Section 3.3).

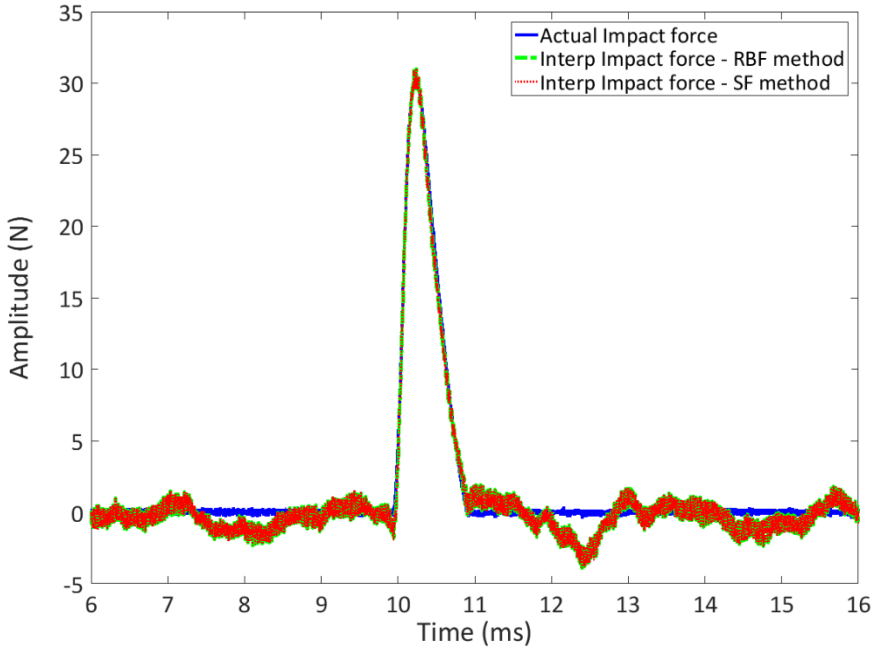

Figure 11. Comparison between the actual impact force and the interpolated ones by using radial basis function (RBF) and shape function (SF) methods. Set 1 of interpolation points on the CFRP plate is considered (see Figure 7).

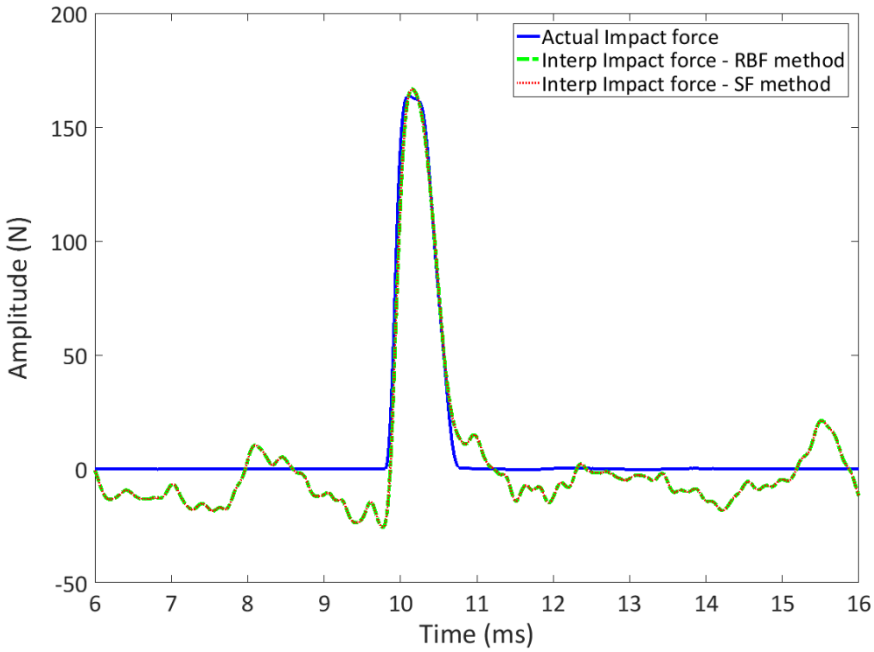

Figure 12. Comparison between the actual impact force and the interpolated ones by using radial basis function (RBF) and shape function (SF) methods. Set 1 of interpolation points on the wing panel is considered (see Figure 8).

Dimensionless errors of both reconstructed impact forces with respect to the actual one on the two specimens are showed in Table 4. They are obtained by using Eq. (32).

Table 4. Comparison between impact forces considering set 1 of interpolation points on both specimens.

		INTERPOLATED IMPACT FORCES			
		RBF method		SF method	
		CFRP plate	Wing panel	CFRP plate	Wing panel
Error Γ	$T = 1$ ms	0.05	0.1	0.05	0.1
	$T = 3$ ms	0.12	0.37	0.12	0.37

As aforementioned, the two interpolation algorithms generated the same results with a small error with respect to the original signal, especially in the detection of impact peak amplitude. It should be noted that the error increases if the considered time window is wider, this is because of the signal fluctuations due to the interpolation process.

5.3 IMPACT FORCE RECONSTRUCTION RESULTS – SET 2 OF CALIBRATION POINTS

Figure 13, Figure 14 and Table 6 depict the same comparison by now considering the set 2 of interpolation points on the two specimens, which are far from the impact location. The coordinates of the new set are reported in Table 5. In Figure 13 and Figure 14, the set 2 is shown with red circles, whilst the other calibration points are depicted with blue circles.

Table 5. Coordinates of set 2 of interpolation points on both specimens.

	CFRP plate		Wing panel	
	x-Coordinate (mm)	y-Coordinate (mm)	x-Coordinate (mm)	y-Coordinate (mm)
Node 1	50	210	110	120
Node 2	110	210	170	120
Node 3	50	270	110	180
Node 4	110	270	170	180

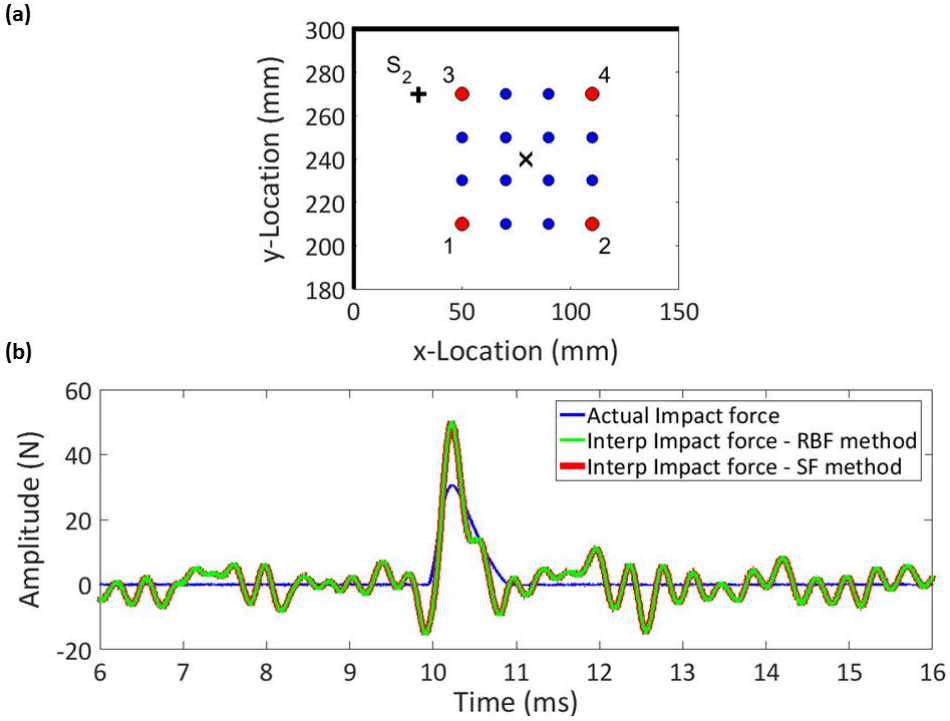

Figure 13. Zoom on the CFRP plate with a reduced section of the initial grid. The calculate impact location is shown as a cross (×) (a). Comparison between the actual impact force and the interpolated ones by using radial basis function (RBF) and shape function (SF) interpolation methods (b).

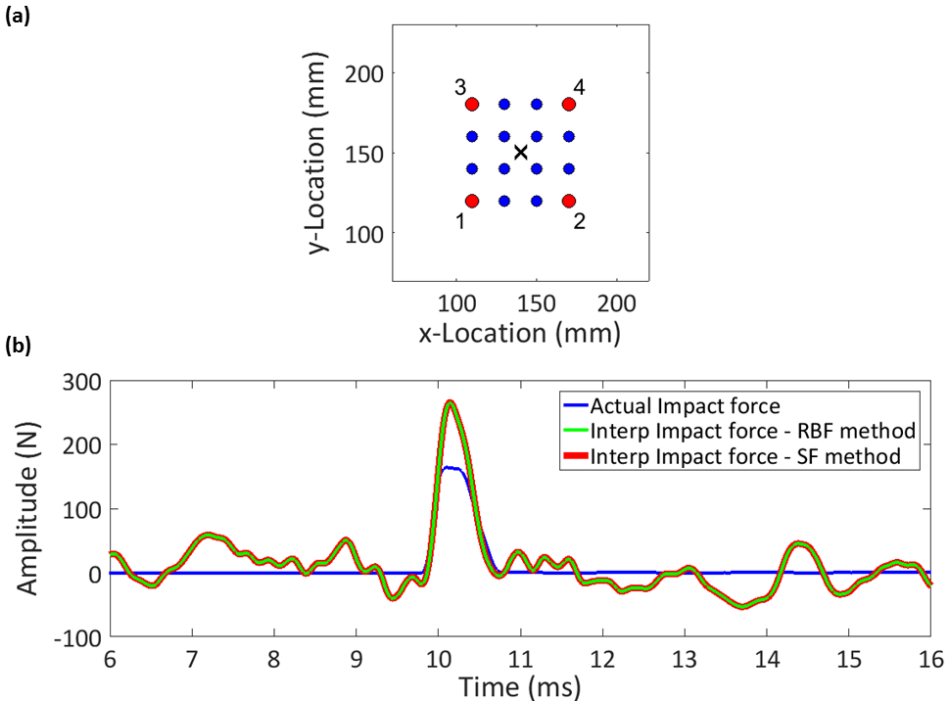

Figure 14. Zoom on the wing panel with a reduced section of the initial grid. The calculate impact location is shown as a cross (×) (a). Comparison between the actual impact force and the interpolated ones by using radial basis function (RBF) and shape function (SF) interpolation methods (b).

Table 6. Comparison between impact forces considering set 2 of interpolation points on both specimens.

		INTERPOLATED IMPACT FORCES			
		RBF method		SF method	
		CFRP plate	Wing panel	CFRP plate	Wing panel
Error Γ	$T = 1$ ms	0.55	0.38	0.55	0.38
	$T = 3$ ms	1.04	0.73	1.04	0.73

It should be noted that, as obtained by considering set 1 (see Table 4), the two interpolation algorithms generated the same results, as reported in Table 6. Comparing Table 4 and Table 6 it is evident that the error increases as the distance between the interpolation points is higher.

5.4 IMPACT FORCE RECONSTRUCTION RESULTS – SET 3 OF CALIBRATION POINTS

In some cases, the calibration process could not be performed on a dense initial grid, therefore information associated with points far from the impact location needed to be used with a high error in the interpolated results. However, unlike the SF method, the RBF interpolation technique is not limited to only four points (as in set 2, please see Section 5.3) and it was possible to take advantage of the information related to other calibration points far from impact event on a coarse initial grid. This is shown in Figure 15, Figure 16 and Table 7 where the information associated with four points closest to the impact on both specimens was not available. The SF interpolation method is applied considering the average between the results obtained by using the two closest to impact sets of calibration points (set 3), as depicted in Figure 15 and Figure 16.

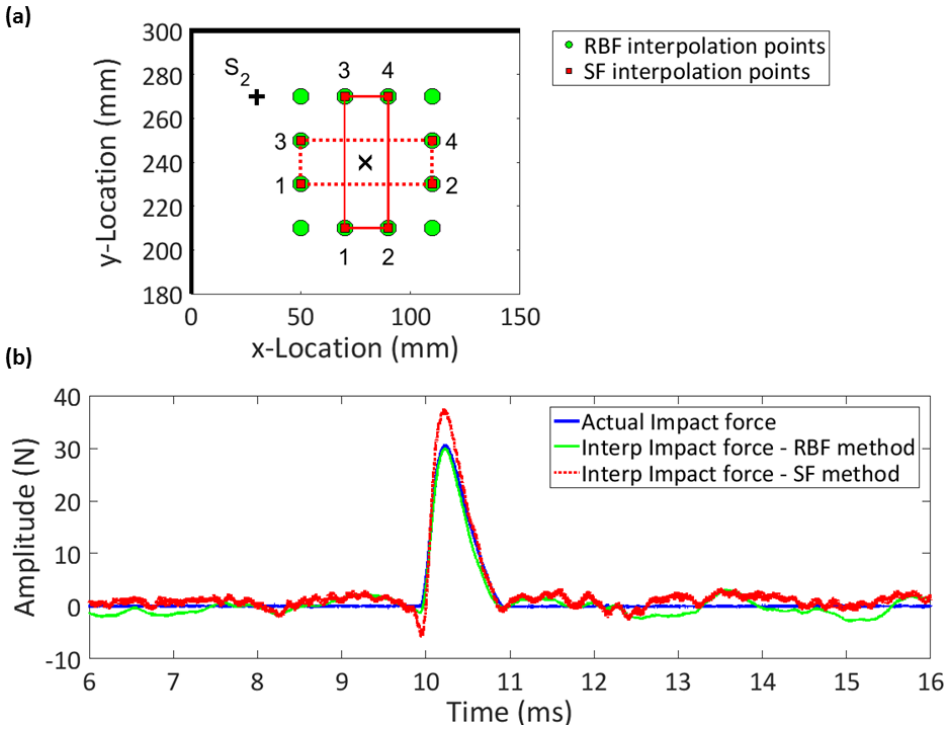

Figure 15. Zoom on the CFRP plate with the two sets 3 of interpolation points. The calculated impact location is shown as a cross (×) (a). Comparison between the actual impact force and the interpolated ones by using radial basis function (RBF) and shape function (SF) interpolation methods (b).

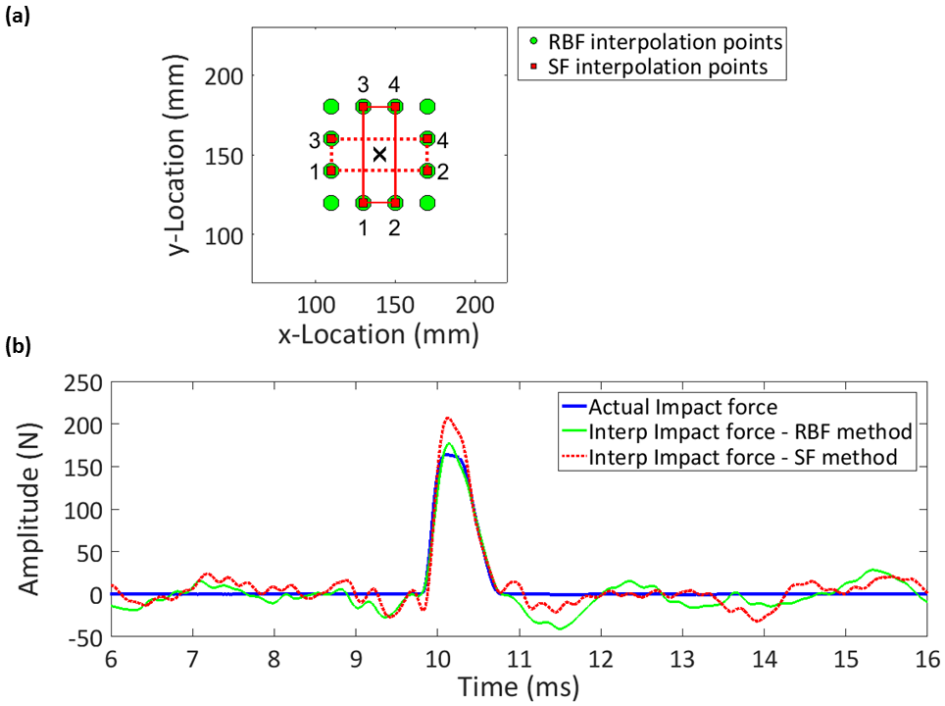

Figure 16. Zoom on the wing panel with the two sets 3 of interpolation points. The calculated impact location is shown as a cross (×) (a). Comparison between the actual impact force and the interpolated ones by using radial basis function (RBF) and shape function (SF) interpolation methods (b).

Table 7. Comparison between impact forces considering the two sets 3 of interpolation points on both specimens.

		INTERPOLATED IMPACT FORCES			
		RBF method		SF method	
		CFRP plate	Wing panel	CFRP plate	Wing panel
Error Γ	$T = 1$ ms	0.09	0.07	0.17	0.18
	$T = 3$ ms	0.24	0.49	0.4	0.41

As depicted in Figure 15 and Figure 16, the RBF interpolation method shows a good performance in detecting the maximum value of the impact force on both specimens (30 N and 150N), despite an higher error of the RBF method with respect to SF method if the wing panel is considered (see Table 7). This is due to a wider

time window ($T = 3$ ms). Nevertheless this result does not affect the validity of the approach in amplitude peak detection when RBF interpolation method is used.

As showed in the comparison between the CFRP plate and the wing panel, the validity of the described method is not dependent of the impact amplitude. Figure 17 and Table 8 illustrates the comparison results considering two different calibration processes on the CFRP plate, with maximum values of impact forces equal to 60 N and 90 N. The sets of calibration points are the same as used in Figure 15 and Figure 16 (set 3), where the information associated with four points closest to the impact on both specimens was not available.

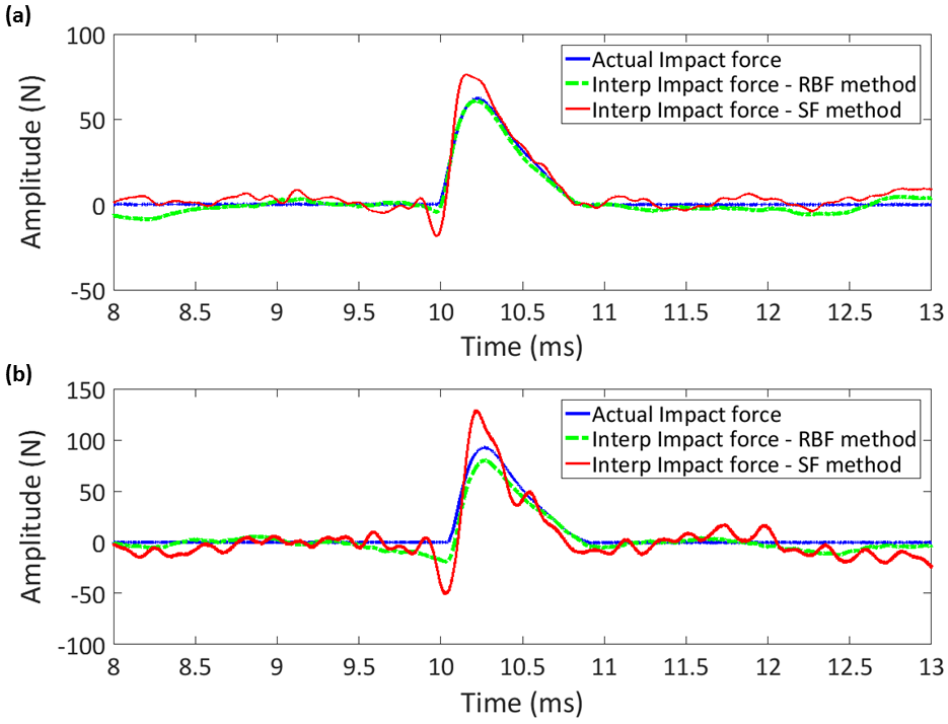

Figure 17. Comparison between the actual impact force and the interpolated ones on the CFRP plate by using radial basis function (RBF) and shape function (SF) interpolation methods, considering the set 3 of calibration points and impact peak amplitudes equal to: 60 N (a) and 90 N (b).

Table 8. Comparison between impact forces considering set 3 of interpolation points on the CFRP plate and different impact peak amplitudes.

		INTERPOLATED IMPACT FORCES	
		RBF method	SF method
$T = 1$ ms	Error Γ (60 N)	0.06	0.18
	Error Γ (90 N)	0.24	0.44
$T = 3$ ms	Error Γ (60 N)	0.18	0.43
	Error Γ (90 N)	0.4	0.74

The results confirmed the accuracy of the proposed method with respect to SF interpolation approach, with a maximum error less than 13 N in the detection of a 90 N impact peak (see Figure 17b). In Figure 18 it is depicted the results comparison related to an impact event on a different location on the wing panel. The errors are reported in Table 9.

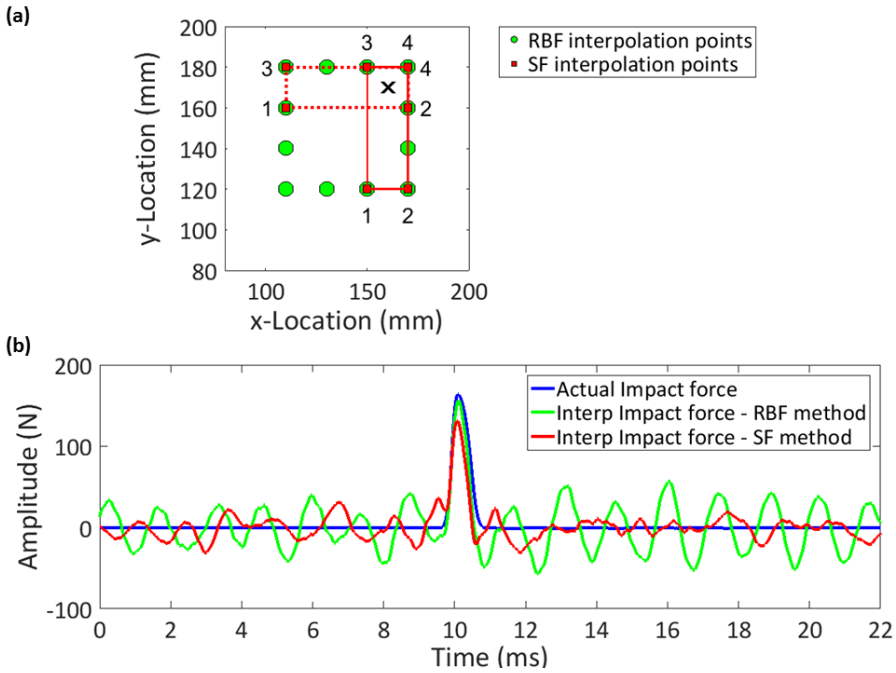

Figure 18. Zoom on the wing panel with the sets of interpolation points. The calculated impact location is shown as a cross (×) (a). Comparison between the actual impact force and the interpolated ones by using radial basis function (RBF) and shape function (SF) interpolation methods (b).

Table 9. Comparison between impact forces considering an impact at different location on the CFRP plate.

		INTERPOLATED IMPACT FORCES	
		RBF method	SF method
Error Γ	$T = 1$ ms	0.27	0.4
	$T = 3$ ms	0.62	0.79

Despite the new impact location on the wing panel is not equally surrounded by the set point used in the RBF interpolation method (the green points in Figure 18), the obtained result is still better than the SF method (see Table 9).

It should be finally noted that, in spite of the hypothesis of linear relation between the impact force and the structural responses [Eqs. (2) and (11)], the obtained results on the real aeronautical structure (i.e. the wing panel) showed the validity of the proposed impact force reconstruction algorithm also in the presence of nonlinear effects due to the material and geometry. This confirmed the robustness of the presented approach.

6 CONCLUSIONS

This paper presented a hierarchical radial basis function algorithm for the reconstruction of the impact force. An initial calibration process was initially performed, which consists of acquiring and storing impact forces and structural responses from a set of excitation points on the specimen surface. The localisation of the impact event was achieved by using time reversal method, which was able to detect the impact coordinates with high level of accuracy. The reconstruction of the impact force was then obtained through an interpolation algorithm based on hierarchical radial basis functions. Such a reconstruction algorithm involved the interpolation of transfer functions calculated during the calibration process by using a Fourier method able to preserve the magnitudes and phases of measured signals. A number of experimental impact tests were performed on a CFRP composite plate-

like structure and an aluminium/CFRP composite wing-stringer-skin panel in order to validate the proposed methodology on full-scale aircraft structures. The radial basis function interpolation method provided an accurate reconstruction of the impact force with a perfect matching of the impact peak. Moreover, this algorithm was compared with an interpolation approach available in literature, which was based on polynomial shape functions. Impact force reconstruction results revealed that the proposed hierarchal algorithm provided higher accuracy, especially when calibration points far from the impact location were considered. The proposed impact location and force reconstruction approach were applied on a real aeronautical structure since no information about the material and geometry was needed, thus allowing for faster and timely inspections.

REFERENCES

1. Kundu, T., Nakatani, H., & Takeda, N. (2012). Acoustic source localization in anisotropic plates. *Ultrasonics*, *52*(6), 740-746.
2. Meo, M., Zumpano, G., Piggott, M., & Marengo, G. (2005). Impact identification on a sandwich plate from wave propagation responses. *Composite structures*, *71*(3), 302-306.
3. Tobias, A. (1976). Acoustic-emission source location in two dimensions by an array of three sensors. *Non-destructive testing*, *9*(1), 9-12.
4. Jacquelin, E., Bennani, A., & Hamelin, P. (2003). Force reconstruction: analysis and regularization of a deconvolution problem. *Journal of Sound and Vibration*, *265*(1), 81-107.
5. Doyle, J. F. (1987). Determining the contact force during the transverse impact of plates. *Experimental Mechanics*, *27*(1), 68-72.
6. Doyle, J. F. (1987). Experimentally determining the contact force during the transverse impact of an orthotropic plate. *Journal of Sound and Vibration*, *118*(3), 441-448.
7. Chang, C., & Sun, C. T. (1989). Determining transverse impact force on a composite laminate by signal deconvolution. *Experimental mechanics*, *29*(4), 414-419.
8. Wu, E., Tsai, T. D., & Yen, C. S. (1995). Two methods for determining impact-force history on elastic plates. *Experimental mechanics*, *35*(1), 11-18.
9. Wu, E., Yeh, J. C., & Yen, C. S. (1994). Identification of impact forces at multiple locations on laminated plates. *AIAA journal*, *32*(12).

10. Kalhori, H., Ye, L., & Mustapha, S. (2017). Inverse estimation of impact force on a composite panel using a single piezoelectric sensor. *Journal of Intelligent Material Systems and Structures*, *28*(6), 799-810.

11. Kalhori, H., Alamdari, M. M., & Ye, L. (2018). Automated algorithm for impact force identification using cosine similarity searching. *Measurement*, *122*, 648-657.

12. Qiao, B., Zhang, X., Gao, J., & Chen, X. (2016). Impact-force sparse reconstruction from highly incomplete and inaccurate measurements. *Journal of Sound and Vibration*, *376*, 72-94.

13. Qiao, B., Zhang, X., Gao, J., Liu, R., & Chen, X. (2017). Sparse deconvolution for the large-scale ill-posed inverse problem of impact force reconstruction. *Mechanical Systems and Signal Processing*, *83*, 93-115.

14. Pan, C. D., Yu, L., Liu, H. L., Chen, Z. P., & Luo, W. F. (2018). Moving force identification based on redundant concatenated dictionary and weighted l1-norm regularization. *Mechanical Systems and Signal Processing*, *98*, 32-49.

15. Yan, G., Sun, H., & Büyüköztürk, O. (2017). Impact load identification for composite structures using Bayesian regularization and unscented Kalman filter. *Structural Control and Health Monitoring*, *24*(5), e1910.

16. Park, J., Ha, S., & Chang, F. K. (2009). Monitoring impact events using a system-identification method. *AIAA J*, *47*(9), 2011-2021.

17. Chen, C., & Yuan, F. G. (2010). Impact source identification in finite isotropic plates using a time-reversal method: theoretical study. *Smart Materials and Structures*, *19*(10), 105028.

18. Chen, C., Li, Y., & Yuan, F. G. (2012). Impact source identification in finite isotropic plates using a time-reversal method: experimental study. *Smart Materials and Structures*, *21*(10), 105025.

19. Xu, L., Wang, Y., Cai, Y., Wu, Z., & Peng, W. (2016). Determination of impact events on a plate-like composite structure. *The Aeronautical Journal*, *120*(1228), 984-1004.

20. Jones, R. T., Sirkis, J. S., & Friebele, E. J. (1997). Detection of impact location and magnitude for isotropic plates using neural networks. *Journal of intelligent material systems and structures*, *8*(1), 90-99.

21. Worden, K., & Staszewski, W. J. (2000). Impact location and quantification on a composite panel using neural networks and a genetic algorithm. *Strain*, *36*(2), 61-68.

22. Haywood, J., Coverley, P. T., Staszewski, W. J., & Worden, K. (2004). An automatic impact monitor for a composite panel employing smart sensor technology. *Smart Materials and*

Structures, *14*(1), 265.

23. Ghajari, M., Sharif-Khodaei, Z., Aliabadi, M. H., & Apicella, A. (2013). Identification of impact force for smart composite stiffened panels. *Smart Materials and Structures*, *22*(8), 085014.

24. Sarego, G., Cappellini, L., Zaccariotto, M., & Galvanetto, U. (2017). Impact force reconstruction in composite panels. *Procedia Structural Integrity*, *5*, 107-114.

25. Ciampa, F., & Meo, M. (2012). Impact detection in anisotropic materials using a time reversal approach. *Structural Health Monitoring*, *11*(1), 43-49.

26. Ciampa, F., & Meo, M. (2014). Impact localization on a composite tail rotor blade using an inverse filtering approach. *Journal of Intelligent Material Systems and Structures*, *25*(15), 1950-1958.

27. Ciampa, F., Boccardi S., & Meo, M. (2016). Factors affecting the imaging of the impact location with inverse filtering and diffuse wave fields. *Journal of Intelligent Material Systems and Structures*, *27*(11), 1523-1533.

28. Ing, R. K., Quieffin, N., Catheline, S., & Fink, M. (2005). In solid localization of finger impacts using acoustic time-reversal process. *Applied Physics Letters*, *87*(20), 204104.

29. Ciampa, F., & Meo, M. (2010). Acoustic emission source localization and velocity determination of the fundamental mode A_0 using wavelet analysis and a Newton-based optimization technique. *Smart Materials and Structures*, *19*(4), 045027.

30. Ciampa, F., & Meo, M. (2010). A new algorithm for acoustic emission localization and flexural group velocity determination in anisotropic structures. *Composites Part A: Applied Science and Manufacturing*, *41*(12), 1777-1786.

31. Ciampa, F., Meo, M., & Barbieri, E. (2012). Impact localization in composite structures of arbitrary cross section. *Structural Health Monitoring*, *11*(6), 643-655.

32. De Simone, M. E., Ciampa, F., Boccardi, S., & Meo, M. (2017). Impact source localisation in aerospace composite structures. *Smart Materials and Structures*, *26*(12).

33. Aldaz, J. M., Barza, S., Fujii, M., & Moslehian, M. S. (2015). Advances in Operator Cauchy-Schwarz inequalities and their reverses. *Annals of Functional Analysis*, *6*(3), 275–295.

34. Katznelson, Y. (2004). *An introduction to harmonic analysis*. Cambridge University Press.

35. Thiene, M., Ghajari, M., Galvanetto, U., & Aliabadi, M. H. (2014). Effects of the transfer function evaluation on the impact force reconstruction with application to composite panels. *Composite Structures*, *114*, 1-9.

36. Haar, A. (1918). Die minkowskische geometrie und die ann an stetige funktionen. *Math. Ann*, *18*, 294-311.

37. Cheney, E. W. (1966). Introduction to approximation theory McGraw-Hill Book Co. New York.

38. Hardy, R. L. (1971). Multiquadric equations of topography and other irregular surfaces. *Journal of geophysical research*, *76*(8), 1905-1915.

39. Davis, P. J. (1975). Interpolation and approximation. Dover, New York.

40. Powell, M. J. D. (1981). Approximation theory and methods. Cambridge University Press.

41. Rippa, S. (1984). Interpolation and smoothing of scattered data by radial basis functions. Tel Aviv University. Master's thesis.

42. Micchelli, C. A. (1986). Interpolation of scattered data: distance matrices and conditionally positive definite functions. *Constructive approximation*, *2*(1), 11-22.

43. Bookstein, F. L. (1989). Principal warps: Thin-plate splines and the decomposition of deformations. *IEEE Transactions on pattern analysis and machine intelligence*, *11*(6), 567-585.

44. Carlson, R. E., & Foley, T. A. (1991). The parameter R2 in multiquadric interpolation. *Computers & Mathematics with Applications*, *21*(9), 29-42.

45. Foley, T. A. (1994). Near optimal parameter selection for multiquadric interpolation. *J. Appl. Sci. Comput*, *1*, 54-69.

46. Fornberg, B. (1998). A practical guide to pseudospectral methods (Vol. 1). Cambridge University Press.

47. Freeden, W., Gervens, T., & Schreiner, M. (1998). Constructive approximation on the sphere with applications to geomathematics. Oxford University Press.

48. Cucker, F., & Smale, S. (2002). On the mathematical foundations of learning. *Bulletin of the American mathematical society*, *39*(1), 1-49.

49. Wright, G. B. (2003). Radial basis function interpolation: numerical and analytical developments. University of Colorado, Boulder. Doctoral dissertation.

50. Fornberg, B., & Flyer, N. (2005). Accuracy of radial basis function interpolation and derivative approximations on 1-D infinite grids. *Advances in Computational Mathematics*, *23*(1), 5-20.

51. Schaback, R., & Wendland, H. (2006). Kernel techniques: from machine learning to meshless methods. *Acta numerica*, *15*, 543-639.

52. Ferreira, A. J., Kansa, E. J., Fasshauer, G. E., & Leitão, V. M. A. (Eds.). (2009). Progress on meshless methods. Berlin, Germany: Springer.

53. Elder, J. (2009). Handbook of statistical analysis and data mining applications. Academic Press.

54. Skala, V. (2016). A practical use of radial basis functions interpolation and approximation. *Proceedings of revista investigacion operacional*, *37*(2), 137-145.

55. Ciampa, F., Pickering, S. G., Scarselli, G., & Meo, M. (2017). Nonlinear imaging of damage in composite structures using sparse ultrasonic sensor arrays. *Structural Control and Health Monitoring*, *24*(5), e1911.

56. Atkinson, K. E. (2008). An introduction to numerical analysis. John Wiley & Sons.

57. Paget, C. A., Atherton, K., & O'Brien, K. (2003, September). Triangulation algorithm for damage location in aeronautical composite structures. In *Proceedings of the 4th International Workshop on Structural Health Monitoring (F. Chang, ed.),(Stanford, CA, USA)* (pp. 363-370).

Chapter 5

Improvements on impact force reconstruction by using time reversal and radial basis functions

In Chapter 4 an impact force reconstruction method based on time reversal and radial basis functions was presented. In that case the impacts involved in the calibration process and the unknown impact tests were performed with the same impactor (an instrumented impact hammer with steel tip) at the same energy, that means with the same force amount. It was not essential to consider unknown impacts at different energy levels; indeed, it is well known that for a linear system, transfer functions obtained from different impact data are the same. Because of the negligibility of nonlinear effects, the authors decided to consider the same force amount for all the impact tests.

The main objective of the publication reported in this Chapter is to demonstrate that with a single set of transfer functions it is possible to perform an accurate impact force reconstruction, also if an impact source completely different from the impactor used in the initial calibration process, and with a different energy level, is considered. Indeed, in industrial field, it is useful to have a sort of “standard

baseline" created only one time in an easy and fast way but, at the same time, suitable for different impact typologies. In a generic case, nonlinear effects could be present in the dynamics of the system with consequential differences in transfer functions. Moreover, a very complex real aeronautical structure (a thick composite wing stringer-skin panel) is considered as monitored specimen in the paper, so it is necessary to take in account also the material nonlinearities.

The idea is to perform different initial calibration process at different energy levels but with the same steel impactor. At the end of the process, the "right" transfer function relating all the distinct impacts at the same calibration point and all the structural responses acquired by a transducer can be calculated as the average of all the obtained transfer functions. This means that the interpolation algorithm by radial basis functions involves the averaged transfer functions related to an appropriate set of calibration points. Also in the presented case, it is fundamental to know the impact coordinates, identified again by using the time reversal method.

It should be noted that during the impact tests no damage occurred in the plate, as supposed in Chapter 4.

The obtained results showed the robustness of the presented approach in reconstruction of the impact force, characterised by a negligible difference (maximum difference in peak amplitudes less than 2.5%) with respect to the actual one, also if a different tip is used on the instrumented hammer, impacting the composite specimen with various energies.

The Statement of Authorship Form and the paper can be found next.

This declaration concerns the article entitled:
A hierarchical impact force reconstruction method for Aerospace composites
Publication status (tick one)

Draft manuscript	
Submitted	
In review	
Accepted	
Published	✓

Candidate's contribution to the paper (detailed, and also given as a percentage)	
The candidate contributed to/ considerably contributed to/predominantly executed the…	
Formulation of ideas:	100% I proposed the entire idea, the hypothesis, the methodology approach and the experimental tests.
Design of methodology:	100% I designed all the algorithms used in the method and the experimental tests to be performed.
Experimental work:	90% I provided all the equipment (structural components, instrumented impact hammer and transducers). I collected all the data and evaluated all the algorithm outputs. My supervisors helped me in results interpretation.
Presentation of data in journal format:	90% I decided structure, wrote all drafts, prepared all figures. Supervisors provided feedback on drafts and helped with submission, responses to reviews and publication process.

Statement from Candidate			
This paper reports on original research I conducted during the period of my Higher Degree by Research candidature.			
Signed		**Date**	26/06/2019

A hierarchical impact force reconstruction method for Aerospace composites

Mario Emanuele DE SIMONE[1,a*], Francesco CIAMPA[2,b], Michele MEO[3,c]

[1,2,3] Department of Mechanical Engineering, University of Bath, Bath, United Kingdom

[a] m.e.de.simone@bath.ac.uk, [b] f.ciampa@bath.ac.uk, [c] m.meo@bath.ac.uk

Keywords: Impact force reconstruction, time reversal, radial basis functions, composite materials.

ABSTRACT

This research work presents a hierarchical method able to reconstruct the time history of the impact force on a composite wing stringer-skin panel by using the structural responses measured by a set of surface bonded ultrasonic transducers. Time reversal method was used to identify the impact location by the knowledge of structural responses recorded from a set of excitation points arbitrarily chosen on the plane of the structure. A radial basis function interpolation approach was then used to calculate the transfer function at the impact point and reconstruct the impact force history. Experimental results showed the high level of accuracy of the proposed impact force reconstruction method for a number of low-velocity impact sources and energies.

1 INTRODUCTION

Composite materials present excellent mechanical properties such as high stiffness and lightweight so that are nowadays used in many industrial applications. However, low-velocity impacts can generate micro-cracks and barely visible

damage in structures, thus leading to serious and dangerous consequences. Structural Health Monitoring (SHM) techniques have been developed in the last decades to localise the impact source [1-6] and reconstruct the force history [7-12]. A number of researches provided the force reconstruction by using the so-called "inverse approach", based on the resolution of a well-known ill-posed deconvolution problem in time domain [8]. Another approach for reconstruction of the time history of the impact force is based on artificial neural network (ANN). Such a method, however, involves the training of complex mathematical models, which makes this technique still cumbersome for real applications.

The impact force reconstruction algorithm proposed in this paper was divided in two stages. The first one relies on the impact localisation with time reversal method [4, 5], which is based on the knowledge of structural responses measured on a set of excitation points (also called "calibration points") on the plane of the specimen. At the end of this stage the "impact cell", that is the cell including the unknown impact, is identified and the location of the impact source in this cell is calculated.

The second stage consists of the impact force reconstruction, obtained following three steps: i) the calculation of the frequency response functions (reported as "transfer functions" in this work) at the corners of the impact cell by using a method able to preserve both signal modules and phases [10] at different impact energies, ii) the calculation of the transfer function at impact location by using the radial basis function (RBF) interpolation method [13] and iii) the impact force reconstruction in the time domain.

This paper builds on from the work recently published by De Simone and Ciampa [12]. The main novelty of this work is the using of a so-called "standard baseline" for recovering the impact force generated by an "unknown" source. This new baseline information corresponds to an average of the data obtained through a steel impactor generating the same impulse at each calibration points for each energy level. Other important novelties in the proposed paper are: 1) calibration points are more far away from each other with respect to the experimental tests reported in [12], therefore less baseline information was available and less impact tests were performed (quicker calibration process) considering the same monitoring area, and,

more importantly, 2) the considered specimen is not a simple plate as in [12] but a composite wing stringer-skin panel, therefore a very complex real aeronautical structure. The presented method provided high level of accuracy in the reconstruction of impact force, also if an impact source completely different from the impactor used in the initial calibration process is considered.

2 FIRST STAGE – IMPACT SOURCE LOCALISATION BY USING TIME REVERSAL METHOD

The first stage of the presented algorithm is achieved by using the time reversal (TR) method. TR is based on the hypothesis of time invariance and spatial reciprocity of elastodynamic wave equation, and the Huygens' principle, through which it is possible to reconstruct the wave function in a generic volume by the knowledge of its sources located on a two-dimensional surface [4, 5].

The aim of the first step of TR method, called "forward propagation step", consists of acquiring and storing: 1) the low-velocity impacts time histories (input signals), performed at M excitation (calibration) points on the specimen surface (focusing plane) and acquired by using a hand-held instrumented hammer, and 2) the structural responses (output signals), acquired by N receiving sensors. It should be noted that excitation points are the corners of a set of cells arranged in a grid that covers the monitoring zone of the specimen surface.

During the second step, called "backward propagation step", a correlation between the N responses due to an impact of unknown location $(\boldsymbol{Gr}_{m0})$ and the $N \times M$ stored responses $(\boldsymbol{Gr}_{m})$, is performed. The cross-correlation operation produces $n \times m$ functions, called "time reversal operators" $\left(R_{TR_s}\right)$. Considering the responses acquired by a single transducer, the moduli of the $1 \times M$ calculated R_{TR_s} are normalised respectively with the geometric mean between the energy of the unknown impact response $\left(E_{G\boldsymbol{r}_{m0}}\right)$, and the M energies of the stored impact responses $\left(E_{G\boldsymbol{r}_{m}}\right)$. The correlation coefficient c_{TR} is used as the similarity measurement between each presented signal couple and it is defined as:

$$c_R = max\left(\frac{|R_{TR}|}{\sqrt{E_{Gr_m}\, E_{Gr_{m0}}}}\right). \quad (1)$$

It is possible to demonstrate that Eq. (1) satisfies the inequality $0 \leq c_{TR} \leq 1$, therefore the c_{TR} is close to one when the signals are similar (i.e. at the true impact location), whilst it is close to zero elsewhere. A number of N correlation coefficients are available at each excitation point, so, in order to consider an average from the contribution of the N receiving sensors, a single mean correlation coefficient at each grid note is calculated. A further mean among the four coefficients related to the corners of each cell is performed, therefore a unique global correlation coefficient c_{TR_GLOBAL} is calculated for each cell. The impact cell is identified as the cell with the maximum c_{TR_GLOBAL}.

The coordinates of the impact source, x_I and y_I, are estimated by a centre-of-gravity method [11, 12]:

$$x_I = \frac{\sum_{i=1}^{4} x_i\, c_{TR_i}}{\sum_{i=1}^{4} c_{TR_i}}, \qquad y_I = \frac{\sum_{i=1}^{4} y_i\, c_{TR_i}}{\sum_{i=1}^{4} c_{TR_i}}, \quad (2)$$

where x_i and y_i are the coordinates of the i^{th} node of the impact cell and c_{TR_i} is the averaged correlation coefficient related to the i^{th} node.

3 SECOND STAGE – IMPACT FORCE RECONSTRUCTION

This study concerns composite components subject to low-velocity impacts. If the structure deformation is considered linearly elastic and small enough to neglect geometric nonlinearities, the relationship between an impact force $p(t)$ and the structural response $u(t)$ can be described by a linear convolution. Such time convolution corresponds to a simple product of signal spectra in the frequency domain according to the following convolution theorem:

$$u(t) = (G \otimes p)(t) = \int_0^t G(t-\tau)\, p(\tau)\, d\tau \Rightarrow U(f) = H(f) \cdot P(f)$$
$$\Rightarrow P(f) = \frac{U(f)}{H(f)} \Rightarrow p(t) = \mathcal{F}^{-1}\{P(f)\}, \tag{3}$$

where $G(t)$ is the Green function, also called "impulse response" if the excitation function is a Dirac delta function (unit impulse function), and $H(f)$ is its Fourier transform, correspondent to the frequency response function (FRF) and called "transfer function". The principal aim of this paper is to recover the spectrum of an unknown impact, and therefore the impact time history through the Inverse Fourier Transform, by the knowledge of structural responses recorded by the N receiving sensors. Information related to the transfer functions are also necessary, so input-output data acquired and stored in the first stage of the algorithm (initial calibration process) are useful in order to calculate the transfer functions on a set of calibration points (e.g. the four corners of the identified impact cell). The transfer function at impact location can be easily estimated by using a suitable interpolation method, as reported in the following Section.

3.1 TRANSFER FUNCTION CALCULATION

Transfer functions are calculated experimentally, as showed in Eq. (4) considering the i^{th} frequency component:

$$H(f_i) = \frac{S_{up}(f_i)}{S_{pp}(f_i)}, \tag{4}$$

where S_{up} is the cross-spectrum between the acquired response and the impact force and S_{pp} is the auto-spectrum of the impact force. This method is described in detail in [10]. A number of N transfer functions are available at each calibration point.

3.2 RADIAL BASIS FUNCTION INTERPOLATION

In a recent work, the authors demonstrated that hierarchical radial basis functions (RBFs) provide high accuracy in the data reconstruction when information related to a point on the structure is not available [12]. In the proposed paper, the unknown data are the N transfer functions at impact location. The RBF interpolation method, explained in detail in [13], requires the coordinates of the impact source, calculated in the first stage by using Eq. (2), and a set of data to be interpolated. These data are the coordinates of a set of calibration points and the transfer functions related to the same points and calculated by using Eq. (4). The transfer function at the impact location considering the i^{th} frequency component is calculated by using the following augmented RBF interpolant considering a two-dimensional approach:

$$h(x_I, y_I)|_{f_i} = \sum_{j=1}^{M'} \lambda_j \, \phi\left(\sqrt{\left(x_I - x_j\right)^2 + \left(y_I - y_j\right)^2}\right) + \gamma_o + \gamma_1 x_I + \gamma_2 y_I \,, \tag{5}$$

where x_I and y_I are coordinates of the impact source, x_j and y_j are coordinates of the M' arbitrary chosen calibration points (whose related information needs to be interpolated), λ_j and γ_k are the expansion coefficients and $\phi(\cdot)$ is a suitable radial basis function. The expansion coefficients are calculated as shown below, as solutions of a linear system of equations:

$$\begin{bmatrix} \lambda_1 \\ \vdots \\ \lambda_{m'} \\ \gamma_1 \\ \gamma_2 \\ \gamma_o \end{bmatrix} = \begin{bmatrix} \phi_{1,1} & \cdots & \phi_{1,m'} & x_1 & y_1 & 1 \\ \vdots & \ddots & \vdots & \vdots & \vdots & \vdots \\ \phi_{m',1} & \cdots & \phi_{m',m'} & x_{m'} & y_{m'} & 1 \\ x_1 & \cdots & x_{m'} & 0 & 0 & 0 \\ y_1 & \cdots & y_{m'} & 0 & 0 & 0 \\ 1 & \cdots & 1 & 0 & 0 & 0 \end{bmatrix}^{-1} \begin{bmatrix} h_1|_{f_i} \\ \vdots \\ h_{m'}|_{f_i} \\ 0 \\ 0 \\ 0 \end{bmatrix}, \tag{6}$$

where $h_1|_{f_i} \ldots h_{m'}|_{f_i}$ are the values of the transfer functions related to the M' arbitrary chosen calibration points at the i^{th} frequency component. The thin plate spline (TPS) is used as radial basis function [12], whose kernel is $\phi(\cdot) = (\cdot)^2 \, ln(\cdot)$.

The described process is performed N times (i.e. N transfer functions are available at each considered point) for all the frequency range. At the end of this step, a number of N transfer functions are available at the impact location.

3.3 IMPACT FORCE IDENTIFICATION

Once the transfer functions at the impact location are obtained, n simple divisions, component by component, are performed, as showed in Eq. (3). Such division allows obtaining N impact spectra, whose their mean is the final impact spectrum, as performed in [11, 12]. The inverse Fourier Transform of the calculated impact spectrum represents the time histories of the unknown impact event. In this paper, the final impact spectrum is obtained by using a different approach, that is the same developed in [7, 10] to take in account the measurements coming from the N receiving sensors. Such approach is shown below:

$$P(f) = \sum_{i=0}^{n} \left[\frac{H_{S_1}^{*}\, U_{S_1} + H_{S_2}^{*}\, U_{S_2} + \cdots + H_{S_n}^{*}\, U_{S_n}}{\left|H_{S_1}\right|^2 + \left|H_{S_2}\right|^2 + \cdots + \left|H_{S_n}\right|^2 + R} \right]_{f_i} \Rightarrow \tag{7}$$

$$\Rightarrow p(t) = \mathcal{F}^{-1}\{P(f)\}\,.$$

The subscripts $S_1, \ldots, S_n$ refer to the N receiving sensors, f_i indicates the frequency component, H^* and $|H|^2$ represents respectively the complex conjugate and the square of the complex modulus of the transfer function. R represents a small amount of random noise, necessary to avoid division by zero in Eq. (3). Experimental tests demonstrated the higher accuracy of the reconstructed impact force by using the described method [Eq. (7)] compared to the approach followed by the authors in [12].

4 EXPERIMENTAL SET-UP

In order to validate the described algorithms, experimental impact tests were conducted on a composite wing stringer-skin panel provided by the courtesy of Airbus UK, with average dimensions of $1680 \times 708 \times 27$ mm^3 (see Figure 1).

The impacts were generated by using a hand-held instrumented hammer (sensitivity factor $= 2.215$ mV/N) connected to a signal conditioner, both manufactured by Meggit-Endevco. Two tips with different hardness were investigated: the steel one was adopted in the initial calibration process, whilst the softer rubber one was used for the unknowns impacts. The calibration process was performed through five impacts with maximum amplitudes at 180 N and five impacts with maximum amplitudes at 270 N, at each calibration point (see Figure 2a), whilst the unknown impacts were performed by using the instrumented hammer connected to a pendulum-system, dropping five times from two different heights (see Figure 2b). Three acoustic emission transducers with 300 kHz central frequency provided by Airbus UK were chosen and arranged in a triangular shape backward the focusing plane (see Figure 1b and Figure 1c). The monitoring area consists of a grid arranged with equally spaced nodes (30 mm), which are the calibration points (see Figure 1a). Signals were acquired using a four-channel oscilloscope with 16 bits of resolution, a sampling rate of 1 MHz and an acquisition window of 10 ms. All algorithms were implemented by the authors by using a MATLAB software code.

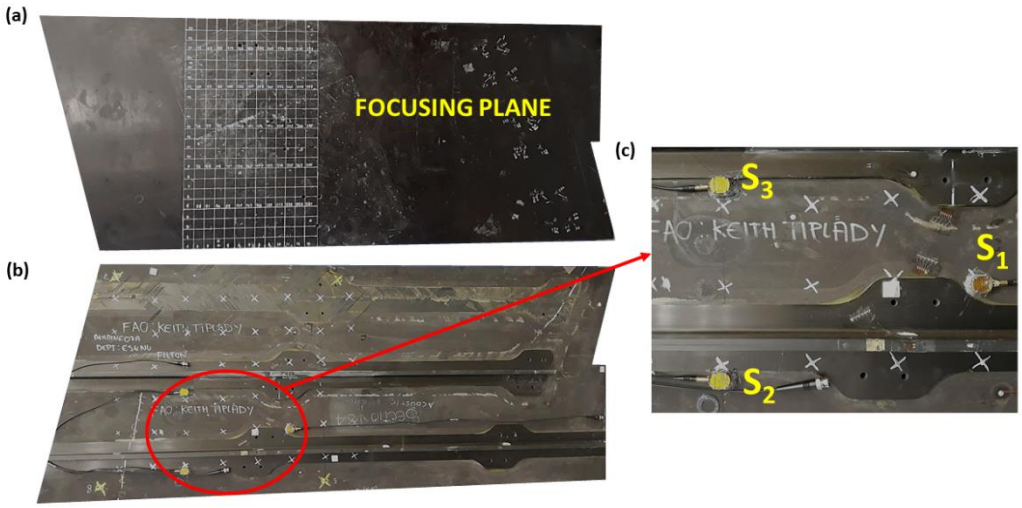

Figure 1. Composite wing stringer-skin panel: focusing plane (a); backward part of the specimen (b); zoom on the transducer locations (c).

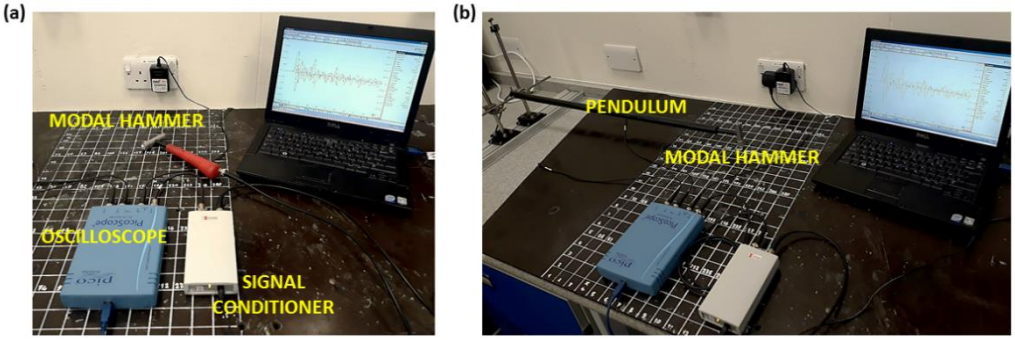

Figure 2. Experimental set-up for: baseline data acquisition (a) and unknown impacts data acquisition (b).

5 RESULTS

Experimental tests revealed that the accuracy of the presented algorithm is guaranteed at each point of the monitoring zone. For clarity reasons, experimental results on ten impacts occurred at the centre of the monitoring zone (see Figure 3) are shown in this Section. The two energy levels considered for the unknown impacts led maximum peak amplitudes at around 180 N and 270 N.

The accuracy of the force reconstruction algorithm is expressed by considering two error functions: the first one [Eq. (8)] represents an error based on time integral of the force in an interval of the recording $[t_2 - t_1]$ which includes the impact force [10, 12]. The second error function [Eq. (8)] estimates the percentage error of the reconstructed impact peak amplitudes with respect to the actual ones [11]. It should be noted that time histories of unknown impacts are available by means of the recorded instrumented hammer data, which was connected to the pendulum-system.

$$a) \quad \Gamma_1 = \frac{\int_{t_1}^{t_2} |p_{real}(t) - p_{rec}(t)|\, dt}{\int_{t_1}^{t_2} p_{real}(t)\, dt}\,, \qquad (8)$$

$$b) \quad \Gamma_2 = \frac{|max(amp)_{real} - max\ (amp)_{rec}|}{max(amp)_{real}} \times 100\,.$$

Figure 3 depicts the monitoring zone of the composite wing with dimensions of 210×330 mm^2: the red "plus" marks indicate transducer locations, the blue "dot" marks represent the calibrations points and the four red "dot" marks are the corners of the impact cell (cell 155), identified with TR method.

Impacts performed at cell 155 (see green mark in Figure 3), generated by the instrumented hammer, were identified by the localisation algorithm with high level of accuracy, with an error always less than 5 mm. The expression for the location error is reported below [6]:

$$\Psi = \sqrt{(x_{real} - x_{calculated})^2 + (y_{real} - y_{calculated})^2}\,, \tag{9}$$

where (x_{real}, y_{real}) are the coordinates of the true impact position and $(x_{calculated}, y_{calculated})$ are the coordinates of the impact location calculated by using Eq. (2).

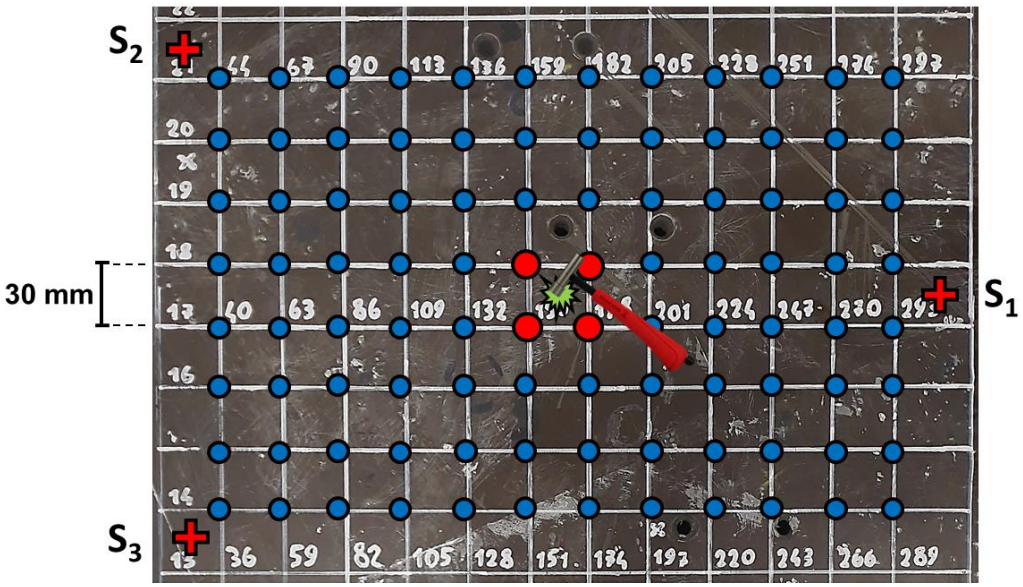

Figure 3. Zoom on the monitoring zone of the composite wing. Transducer locations, calibration points and impact cell are reported. The green mark represents the unknown impact at cell 155.

Once identified the impact source location and the impact cell, the two baseline data sets (at 180 N and 270 N) related to the four corners were extrapolated, averaged and used for the RBF interpolation.

Three transfer functions related to the impact location were available at the end of the interpolation process, due to the contribution of the three receiving sensors. The mean impact spectrum and the time history of the impact force were obtained by using Eq. (7).

In Figure 4 and Figure 5, the reconstruction of ten unknown impacts with maximum amplitudes respectively at around 180 N and 270 N are presented. The considered time interval for the Γ_1 error [Eq. (8a)] was $t_1 = 0.5$ ms and $t_2 = 1.6$ ms. As depicted in figures below the unknown impact forces were reconstructed with high accuracy, with a maximum difference in peak amplitudes less than 1.1% for the first set of impacts (180 N) and less than 2.2% for the second set (270 N).

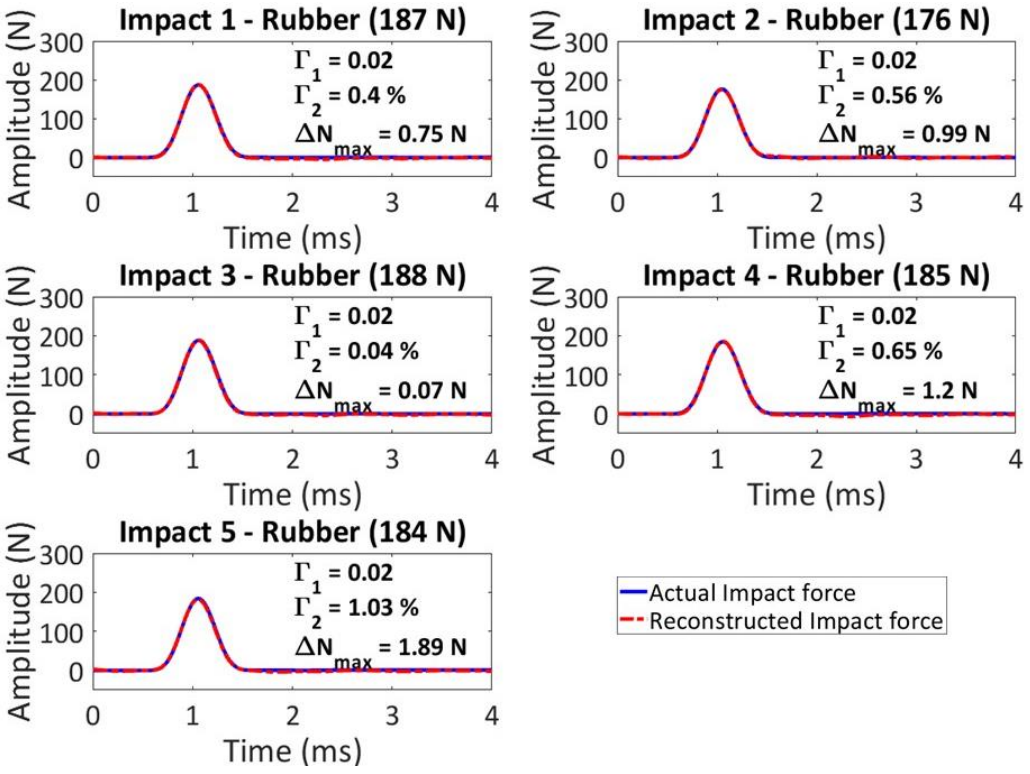

Figure 4. Reconstruction of the first set of unknown impact forces with error comparison values. The five impacts were recorded by the instrumented hammer with the rubber tip. The maximum peak amplitudes were at around 180 N.

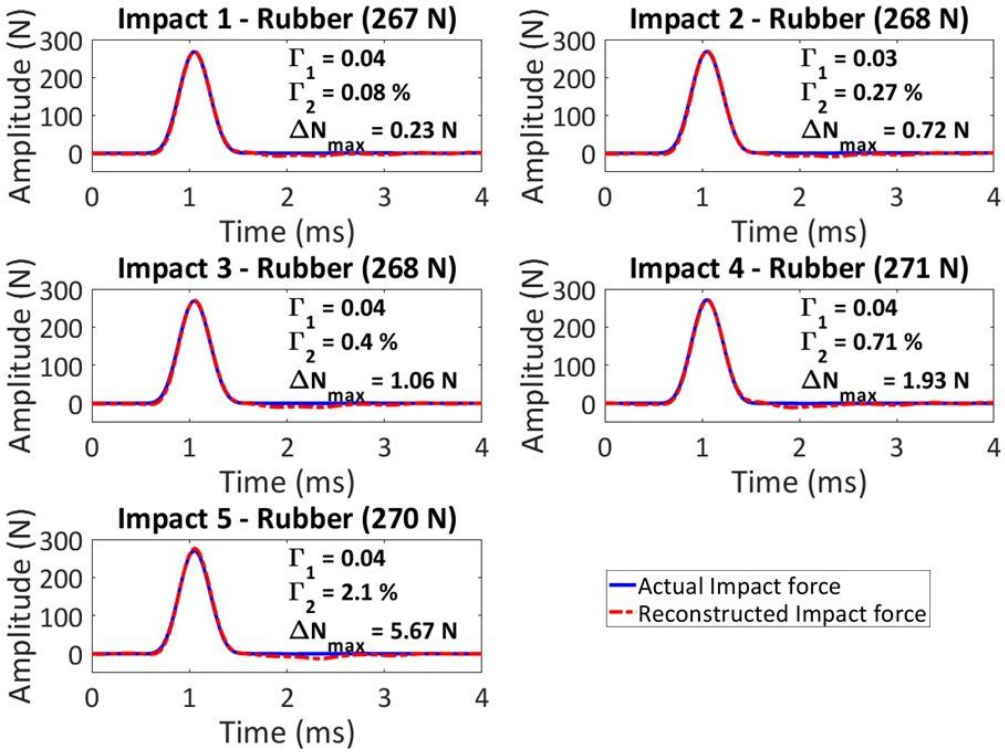

Figure 5. Reconstruction of the second set of unknown impact forces with error comparison values. The five impacts were recorded by the instrumented hammer with the rubber tip. The maximum peak amplitudes were at around 270 N.

6 CONCLUSIONS

A method capable of reconstructing the impact force due to low-velocity impacts was presented and investigated. The localisation of the source events was performed by using the time reversal method, therefore an initial calibration process was necessary. It consists of acquiring and storing impact forces with different peak amplitudes and structural responses, recorded by using respectively a hand-held instrumented hammer and a set of surface bonded ultrasonic transducers, from a set of excitation points on the specimen's surface. Transfer functions at the four corners of the identified impact cell were calculated, averaged and interpolated by using a hierarchical radial basis function algorithm. The mean impact spectrum and impact force were calculated. A number of experimental tests was performed on a composite wing stringer-skin panel in order to validate the proposed methodology.

The algorithm was able to reconstruct impact forces due to object different with respect to the impactor used in the calibration process with high accuracy. The error functions showed a negligible difference between the actual impact forces and the reconstructed ones.

REFERENCES

1. Meo, M., Zumpano, G., Piggott, M., & Marengo, G. (2005). Impact identification on a sandwich plate from wave propagation responses. *Composite structures*, *71*(3-4), 302-306.
2. Ciampa, F., Meo, M., & Barbieri, E. (2012). Impact localization in composite structures of arbitrary cross section. *Structural Health Monitoring*, *11*(6), 643-655.
3. Kundu, T. (2014). Acoustic source localization. *Ultrasonics*, *54*(1), 25-38.
4. Ciampa, F., & Meo, M. (2014). Impact localization on a composite tail rotor blade using an inverse filtering approach. *Journal of Intelligent Material Systems and Structures*, *25*(15), 1950-1958.
5. Ciampa, F., Boccardi, S., & Meo, M. (2016). Factors affecting the imaging of the impact location with inverse filtering and diffuse wave fields. *Journal of Intelligent Material Systems and Structures*, *27*(11), 1523-1533.
6. De Simone, M. E., Ciampa, F., Boccardi, S., & Meo, M. (2017). Impact source localisation in aerospace composite structures. *Smart Materials and Structures*, *26*(12).
7. Martin, M. T., & Doyle, J. F. (1996). Impact force identification from wave propagation responses. *International journal of impact engineering*, *18*(1), 65-77.
8. Jacquelin, E., Bennani, A., & Hamelin, P. (2003). Force reconstruction: analysis and regularization of a deconvolution problem. *Journal of sound and vibration*, *265*(1), 81-107.
9. Park, J., Ha, S., & Chang, F. K. (2009). Monitoring impact events using a system-identification method. *AIAA journal*, *47*(9), 2011-2021.
10. Thiene, M., Ghajari, M., Galvanetto, U., & Aliabadi, M. H. (2014). Effects of the transfer function evaluation on the impact force reconstruction with application to composite panels. *Composite Structures*, *114*, 1-9.
11. Xu, L., Wang, Y., Cai, Y., Wu, Z., & Peng, W. (2016). Determination of impact events on a plate-like composite structure. *The Aeronautical Journal*, *120*(1228), 984-1004.
12. De Simone, M. E., Ciampa, F., & Meo, M. (2019). A hierarchical method for the impact

force reconstruction in composite structures. *Smart Materials and Structures*, *28*(8).

13. Wright, G. B. (2003). Radial basis function interpolation: numerical and analytical developments. University of Colorado, Boulder, Doctoral dissertation.

Chapter 6

Proof of concept for a smart composite orbital debris detector

Space debris is defined as non-functional, human-made objects, including fragments and elements thereof, in Earth orbit or re-entering into Earth's atmosphere. Human-made space debris dominates over the natural meteoroid environment, except around millimetre sizes. The presence of space debris and micrometeoroids particles in the space environment are a serious threat for Earth orbiting spacecraft. Hypervelocity impacts (HVIs) at the typical velocities of around 7-10 km/s can severely damage or destroy satellites, so that debris removal devices are necessary.

In the publication presented in this Chapter, a "smart" composite detector of orbital debris and micrometeoroids particles is proposed and developed as proof of concept for future space missions. The fundamental idea of the authors was to use some of the algorithms and the methods described in previous Chapters in a different application, involving also considerations about space environment. Details related to the scientific background and previous research works in this field can be found in the Introduction section of the following paper.

The presented detector consists of two thin parallel carbon fibre reinforced plastic (CFRP) composite plates, each instrumented with three piezoelectric transducers embedded into the laminate. The developed algorithm can estimate both directions and velocities of orbital debris and micrometeoroids particles by the knowledge of: (i) impact locations on the two plates, (ii) the time differences of arrival of acoustic emissions generated by impacts and (iii) the wave velocity profile in the composite plates. The localisation of the impact events is estimated by time reversal methods (see Chapter 4 and Chapter 5), while the time of arrivals are calculated by using Akaike Information Criterion method (see Chapter 3).

A set of experimental tests were performed to validate the proof of concept using a small drop tower. Impact results showed the high accuracy of the proposed algorithm in the estimation of impact locations (maximum location error small than 1 mm), directions and velocities of impact objects.

The Statement of Authorship Form and the paper can be found next.

This declaration concerns the article entitled:	
Proof of concept for a Smart Composite Orbital Debris Detector	
Publication status (tick one)	
Draft manuscript	
Submitted	
In review	
Accepted	
Published	✓

Candidate's contribution to the paper (detailed, and also given as a percentage)	
The candidate contributed to/ considerably contributed to/predominantly executed the…	
Formulation of ideas:	30% The ideas were proposed by my supervisors.
Design of methodology:	80% I designed all the algorithms used in the method. The experimental tests to be performed were set with the help of supervisors.
Experimental work:	70% I provided most of equipment. The structural components were provided by a colleague of mine, Christos Andreades. The experimental tests were conducted with the help of a final year student. I collected all the data and evaluated all the algorithm outputs. My supervisors helped me in results interpretation.
Presentation of data in journal format:	80% I decided structure, wrote all drafts, prepared all figures. Supervisors and Christos provided feedback on drafts and helped with submission, responses to reviews and publication process.
Statement from Candidate	
This paper reports on original research I conducted during the period of my Higher Degree by Research candidature.	

Signed	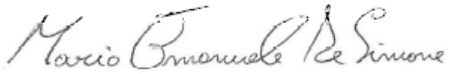	**Date**	26/06/2019

Proof of concept for a Smart Composite Orbital Debris Detector

Mario Emanuele DE SIMONE[a], Christos ANDREADES[a], Mohamad Hizami MOHAMAD HILMI[a], Michele MEO[a], Francesco CIAMPA[b]*

[a]Department of Mechanical Engineering, University of Bath, Bath, BA2 7AY, UK
[b]Department of Mechanical Engineering Sciences, University of Surrey, Guildford, GU2 7XH, UK

* corresponding author: f.ciampa@surrey.ac.uk

Keywords: Space debris, impact localisation, time reversal, composite materials, embedded sensors.

ABSTRACT

Space debris particles with dimensions smaller than tens of millimetres are not trackable with existing monitoring systems and have sufficient energy to harm orbiting Earth satellites during impact events. This paper presents a proof of concept for an in-situ smart carbon fibre reinforced plastic (CFRP) composite orbital debris detector that is capable of localising space debris impacts on Earth satellites and measuring the direction and velocity of debris particles. This spacecraft detection system can be used to warn satellites about the impact occurrence and to enhance current Space Surveillance Networks by providing a catalogue of debris objects. The proposed orbital debris detector consists of two thin parallel CFRP composite plates, each instrumented with three piezoelectric transducers embedded into the laminate. The localisation method is based on the measurement of acoustic emissions generated by debris impacts on the CFRP plates, which are processed with the time reversal algorithm. The calculation of the direction of debris particles and their speed are accomplished by determining the arrival time of acquired signals

and the speed of waves propagating within each CFRP plate. Experimental results showed accurate estimation of the impact location, direction and velocity, thus demonstrating the potential use of the proposed orbital debris detector in future Earth satellite systems.

1 INTRODUCTION

Space debris accounts for about 95% of human-made orbiting objects in the outer space [1] and includes non-functional entities such as fragments and elements orbiting around the Earth or re-entering the Earth's atmosphere [2]. In Low Earth Orbit (LEO), space debris speeds are typically around 7 - 10 km/s [3] and impacts at these velocities are commonly referred to as "hypervelocity impacts" (HVIs). In HVIs, the impact speed is such that the strength of materials upon impact is sufficiently small compared to their inertial forces [4, 5]. As a result, high impact energies are achieved even with small particles having dimensions ranging between 10 μm and few mm, which are sufficient to harm the orbiting spacecraft. Large objects (> 1 - 10 cm) would, instead, destroy or severely damage the satellite [6]. Debris particles greater than few tens of mm are generally detectable with current optical systems (e.g. telescopes [7, 8]), so that collision avoidance measures can be taken. These include mitigation and remediation methods, and active debris removal technologies. Mitigation methods involve the use of space debris models for mission risk analysis and debris population such as the ESA's Meteoroid and Space Debris Terrestrial Environment Reference (MASTER) and NASA's Orbital Debris Engineering Model (ORDEM) series [9-11], as well as space debris tracking and monitoring systems such as the NASA Meter-Class Autonomous Telescope [8]. Remediation methods are, for example, spacecraft shields used to protect the spacecraft against impacts from untracked debris [12]. Whipple shield and its variations such as Multi-Shock and Stuffed Whipple shields [13] are the most widely used protection systems on modern spacecrafts. Active debris removal is, lately, the most effective yet the most challenging measure against space debris. Some examples of space debris removal technologies include satellite drag sails

[14], hybrid propulsion for re-entry after service [1] and debris capture systems using the space net [15]. However, these technologies still need years or even decades for full implementations to take place.

Nevertheless, all above mentioned technologies do not currently allow protection from small debris particles, which are not trackable nor visible with existing observation systems. Hence, mitigation strategies including the development of *in-situ* passive space debris detectors carried on satellites are required to minimise the failure risk of future unmanned spacecrafts and manned operational space stations (e.g. the International Space Station) [6]. In particular, *in-situ* passive detectors can provide in-service monitoring of spacecraft components and are able to characterise space debris population by measuring the trajectory (direction), the time of impact and velocity of particles. This information is of fundamental importance to (*i*) understand the orbital dynamics of space debris, (*ii*) allow rapid warning to orbiting satellites of the impact occurrence, (*iii*) enhance current Space Surveillance Networks by providing an accurate catalogue of debris objects of various dimensions and (*iv*) validate existing numerical models for the orbital prediction of space debris with experimental orbital data [9].

For this scope, a number of passive debris detection systems have been proposed and validated in literature. Burchell et al. [16, 17] investigated a debris sensing technology using a resistive grid sensitive to hypervelocity impacts. In this concept, the particle penetration of a thin substrate with a resistive grid enabled changes to the overall grid resistance. These changes were proportional to the perforation area that, in turn, was related to the debris particle's size. This detection system was validated with particles of 0.15 mm diameter and above. Bauer et al. [18] recently developed the Solar Panel based Space Debris Impact Detector (SOLID) that uses an autonomous electronic box implemented into the spacecraft and solar panel structures to monitor impact damage. Forli [19] and Schäfer and Janovsky [20] used acoustic emission based impact sensor networks to detect HVIs. Graziani et al. [21] developed an impact debris detector that was installed on the UNISAT microsatellite and used piezoelectric (PZT) patches for on-board monitoring of the micro-particle environment.

Regarding to the elastic wave propagation in solids after HVIs, Liu et al. [4, 5] demonstrated that HVI-induced shock waves generated at the impact spot convert rapidly into standard elastic waves. Standards waves can be, therefore, measured by traditional signal detection systems to provide information about the impact location. Kobayashi et al. [22] recently developed the Circum-Martian Dust Monitor (CMDM) system consisting of a thin film and PZT sensors, which will be used in the JAXA's Martian Moons Exploration (MMX) project. Corsaro et al. [23] conducted an experiment to characterise space dust using acoustic emissions. Their system was inspired by the multi-layer spacecraft shielding technology and consisted of two pairs of four Polyvinylidene Fluoride (PVDF) sensors placed on two parallel Mylar thin films to provide impact location. In Corsaro et al.'s work, triangulation techniques based on accurate time-of-flight measurements were used to identify the impact location and determine the impact direction and velocity of debris objects. However, such a debris detection system was affected by the uncertainty of the time of arrival estimation, which may cause large errors on the impact location. Moreover, the use of Mylar films required PVDF sensors to be exposed to the outer space.

This paper builds on Corsaro et al.'s work [23] and aims at developing an *in-situ* and lightweight "Smart Composite Orbital Debris Detector (SCODD)" based on acoustic emission measurements, which is capable of localising space debris impacts and measuring the direction and velocity of debris particles. The proposed SCODD system consists of two sacrificial thin parallel carbon fibre reinforced plastic (CFRP) composite plates, which are instrumented with three embedded PZTs located at the middle layer of each plate. The two CFRP samples were manufactured thin enough so that they can be easily penetrated by the debris particles without significantly slowing their orbital speed. As a result, the impact energy attenuation during penetration can be neglected even with small debris objects. The technology for embedding PZT transducers into CFRP laminates was recently developed by the authors and reported in Andreades et al.'s paper [24]. The implementation of embedded acoustic transducers, as in the proposed SCODD system, represents more practical approaches for space applications where harsh

space environmental conditions such as extreme temperatures and high levels of radiation and humidity may easily degrade surface mounted piezo-films and exposed transducers. Moreover, for the accurate impact localisation in both plates, time reversal (TR) method was used (see, for instance, [25-29]). Particle direction can be easily determined by knowing the impact locations on the two plates. Debris particle velocity was then calculated by determining the arrival times (TOAs) of acquired waveforms and the speed of waves propagating in the CFRP specimens. TOAs were obtained by using the Akaike Information Criterion method, which provides the onset time of a recorded signal with microseconds of precision [30]. The outline of this research work is as follows: in Section 2, the SCODD system is presented. The particle direction calculation is shown in Section 3, whose main parts are the time reversal method for the impact localisation in Section 3.1, and the angular parameters identifying the particle direction of arrival in Section 3.2. The particle speed is the topic of Section 4. Section 5 shows the set-up used to perform experimental tests, whilst in Section 6 all the experimental impact results are illustrated. The conclusions of this paper are presented in Section 7.

2 SMART COMPOSITE ORBITAL DEBRIS DETECTOR

The objectives of the SCODD system are the impact location and the estimation of both direction and speed of debris objects impacting the detector. The proposed SCODD system is shown in Figure 1, in which S_i $(i = 1, 2, 3)$ are the three piezoelectric transducers embedded in each CFRP laminate. In this concept, the space debris particle hits the thin CFRP top plate at the time t^* and continues along its trajectory towards the bottom one. The particle impacts the bottom sample at the time $t^* + \frac{s_p}{V_p}$, where V_p is the particle's velocity and s_p is the distance covered by the particle between the two impact points on the two plates. For clarity reasons, a two-dimensional illustration of the proposed SCODD system is represented in Figure 2. An impact perpendicular to both membranes is considered and only one couple of transducers, S_1, embedded at the same location on both plates is represented.

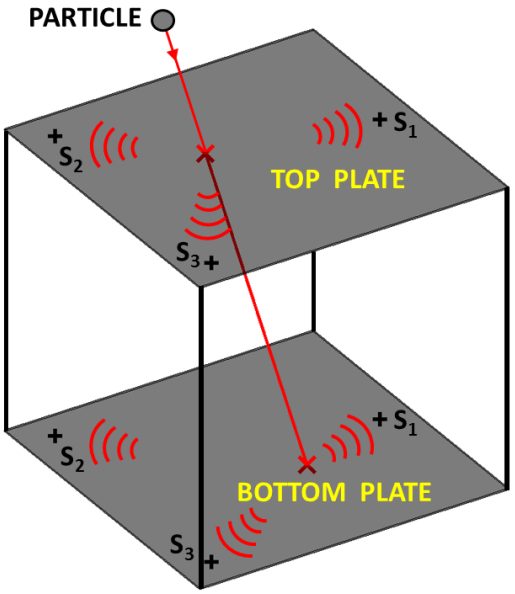

Figure 1. 3D sketch of the proposed SCODD system.

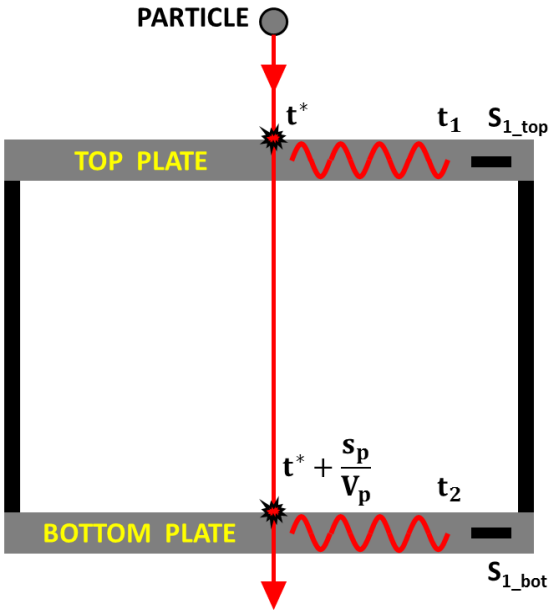

Figure 2. Illustration of the impacting debris particle perpendicular to the plane of both CFRP plates with embedded PZT transducers.

Acoustic waves generated by the impact on the top plate propagate along the membrane and are detected by the receiver transducer S_{1_top} at time t_1, whose mathematical expression is:

$$t_1 = t^* + \frac{r_1}{V_{w\_top}}, \tag{1}$$

where r_1 is the distance between the impact location and the position of the transducer S_{1_top} on the top plate. The velocity V_{w_top} is the propagation speed of the acoustic waves in the top plate and is calculated by using an initial calibration process (see Section 4.2 for details). After the particle penetrates the bottom plate, elastic waves propagate into the sample and are acquired by the receiver sensor S_{1_bot} at time t_2, whose mathematical expression is:

$$t_2 = t^* + \frac{s_p}{V_p} + \frac{r_2}{V_{w\_bot}}. \tag{2}$$

Similarly to r_1, r_2 represents the distance between the impact location and the position of the transducer S_{1_bot} on the bottom plate. The particle velocity can be calculated by using the time difference Δt measured by the two embedded transducers:

$$\Delta t = t_2 - t_1 = \frac{s_p}{V_p} + \frac{r_2}{V_{w\_bot}} - \frac{r_1}{V_{w\_top}}. \tag{3}$$

The final expression for the speed of the debris particle is:

$$V_p = \frac{s_p}{\Delta t + \frac{r_1}{V_{w\_top}} - \frac{r_2}{V_{w\_bot}}}. \tag{4}$$

Since both CFRP plates are the same, we can assume $V_{w\_top} = V_{w\_bot}$. In the simple case of an impact perpendicular to both plates, the distance $r_1 \equiv r_2$ and it is:

$$V_p = \frac{s_p}{\Delta t}. \tag{5}$$

It should be also noted that Eq. (4) considers only a couple of embedded transducers at the same locations on the two plates. In this work, a number of $N = 3$ embedded transducers were considered for the processing of time reversal, so N velocities were calculated. Following a calibration process of CFRP plates, the particle velocity was obtained as the mean of the N estimated velocities.

3 ESTIMATION OF SPACE DEBRIS IMPACT LOCATION AND DIRECTION

In this Section, the algorithm for the estimation of the impact location and debris particle direction is presented. The particle trajectory (direction) is identified by two angular parameters, the "elevation", α, and the "azimuth", γ, which are measured in a horizontal coordinate system relative to the bottom plate.

3.1 IMPACT LOCALISATION ALGORITHM

A number of impact localisation algorithms were developed for both isotropic and anisotropic media [30-35]. In this work, the time reversal method is used to achieve high accuracy on the impact localisation for the SCODD system. TR is based on the hypothesis of time invariance and spatial reciprocity of the elastodynamic wave equation and on the Huygens' Principle, through which it is possible to reconstruct the wave function in a generic volume by the knowledge of its sources located on a two-dimensional surface. A detailed theoretical explanation of the TR method is presented in [25-29]. TR is typically divided into the "forward" and "backward" propagation steps. In the "forward" one, calibration impacts were applied in M excitation points, also called "calibration points", which were arbitrarily chosen on the plane of the plate (focusing plane) identifying the monitoring zone. A number of N receiving sensors were used, so that a set of $N \times M$ signals was acquired and stored in the computer memory. These waveforms represent the impulsive response of the single CFRP plate subject to impact loading. The "backward" propagation step consisted of correlating the waveform emitted by a point of unknown position $\boldsymbol{r}_{m0}$ with all the impulse responses stored in the "forward" step. It can be demonstrated that the impact location is calculated as the maximum of the following time reversal operator (i.e. when $\boldsymbol{r}_m = \boldsymbol{r}_{m0}$):

$$R_{TR} = G(\boldsymbol{r}_m, t;\, \boldsymbol{r}) \otimes G(\boldsymbol{r}, -t;\, \boldsymbol{r}_{m0}) = \int_0^t G(\boldsymbol{r}_m, t;\, \boldsymbol{r})\, G(\boldsymbol{r}, t+\tau;\, \boldsymbol{r}_{m0})\, d\tau\,, \tag{6}$$

which represents a cross correlation operation. The symbol $\otimes$ represents a convolution over time and $G(\cdot)$ denotes the Green space-time function. It should be noted that for the experimental campaign, given the existing facilities available, HVIs could not be performed during both "forward" and "backward" steps and low-velocity impacts were, instead, examined. However, the lower impact speed would not compromise the validity of the proof of concept for the proposed SCODD system. Indeed, in accordance with both numerical and experimental evidence reported by Liu et al. [4, 5] and Burchell et al. [16, 19], elastic modes recorded during low-velocity impacts resemble those generated after shock waves during HVIs. In particular, after HVI occurrence, pressure-induced shock waves are immediately converted into standard elastic modes due to wave attenuation and diffraction distance [5]. Moreover, whilst shock waves require high speed data acquisition systems (~100 million samples per second), traditional bulk and guided waves involve lower signal acquisition rates [16, 19] and [20]. Hence, standard elastic modes can be used to retrieve the information of the impact location. For the TR process, signals at different elastic energies caused by low-velocity impacts were measured in the "forward" propagation step and a normalisation of the energy of acquired signals was performed. Such a normalisation allowed TR to be independent from the amplitude and, thus, from the elastic energy of recorded waveforms. Such a normalisation process is expressed as follows:

$$|R_{TR}| \leq \|G(\boldsymbol{r}_m, t;\, \boldsymbol{r})\|\, \|G(\boldsymbol{r}, t+\tau;\, \boldsymbol{r}_{m0})\| = \sqrt{E_{G\boldsymbol{r}_m}\, E_{G\boldsymbol{r}_{m0}}}\,, \tag{7}$$

where E_G is the waveform's elastic energy. As a measure of similarity of two signals, the time reversal correlation coefficient, c_{TR}, was used, which is defined as:

$$c_{TR} = max\left(\frac{|R_{TR}|}{\sqrt{E_{Gr_m}\, E_{Gr_{m0}}}}\right). \quad (8)$$

Eq. (8) satisfies the inequality $0 \leq c_{TR} \leq 1$. The c_{TR} coefficient is close to one when the signals are similar (i.e. at the true impact location), whilst it is close to zero elsewhere. In order to compensate the incoherent measurement noise due to electronics, an average from the contribution of the N receiving sensors was here used and a single mean correlation coefficient was related to each grid node. According to Figure 3, each cell of the grid on the monitoring zone is identified by four nodes and it was possible to perform a further mean among the correlation coefficients associated to each node in order to calculate a global correlation coefficient of the cell, indicated as c_{TR_GLOBAL}.

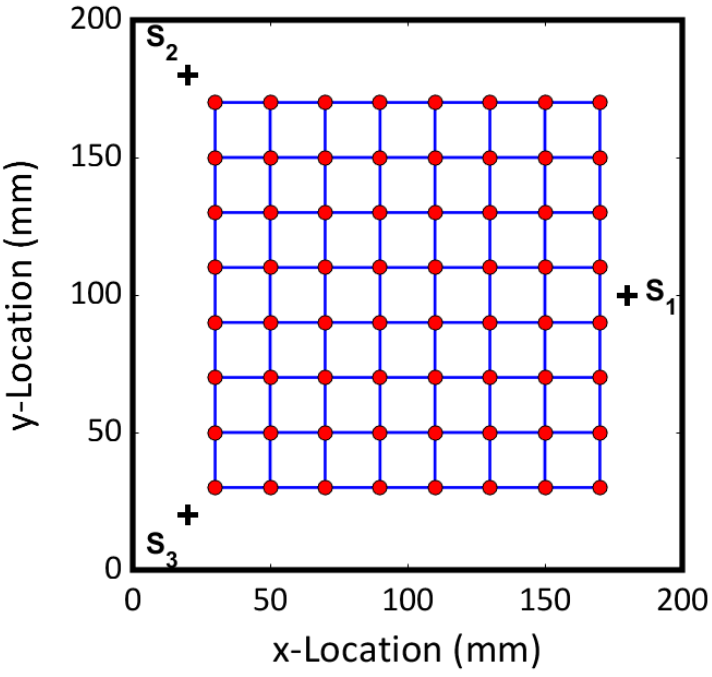

Figure 3. Initial surface grid. Calibration points are depicted as red spots.

Similarly to [36] and [37], the impact coordinates were finally estimated by the following centre-of-gravity method:

$$x_I = \frac{\sum_{i=1}^{4} x_i \, c_{TR_i}}{\sum_{i=1}^{4} c_{TR_i}}, \qquad y_I = \frac{\sum_{i=1}^{4} y_i \, c_{TR_i}}{\sum_{i=1}^{4} c_{TR_i}}, \tag{9}$$

where x_i and y_i are the coordinates of the i^{th} node of the impact cell, c_{TR_i} is the averaged correlation coefficient related to the i^{th} node, x_I and y_I are the estimated locations of the current impact event.

3.2 ESTIMATION OF THE PARTICLE DIRECTION PARAMETERS

Once obtained the coordinates of the impact locations on both plates, it is possible to evaluate the distance covered by the particle between the two impacts and its direction. A three-dimensional spherical coordinate system was used, in which a generic position vector, $\boldsymbol{s_p}$, joining two points in space is identified by the following three parameters:

- the Euclidean distance, s_p, between the two points, which is the modulus of the position vector $\boldsymbol{s_p}$;
- the azimuth angle, γ, of the orthogonal projection of $\boldsymbol{s_p}$ on a reference plane passing through its origin and that is orthogonal to the zenith direction, measured from a fixed reference direction on that plane;
- the elevation angle, α, measured from the orthogonal projection of $\boldsymbol{s_p}$ on a reference plane towards the direction of $\boldsymbol{s_p}$ and that is restricted to the interval $[0^\circ \;\; 90^\circ]$.

Figure 4 illustrates the described coordinate system related to SCODD. The origin of the Cartesian coordinate system is chosen as one of the corners of the bottom plate, which is considered as the reference *xy*-plane (the horizon). The *z*-axis is chosen to form the right-handed coordinate system, positive towards the corner of the top plate (i.e. the zenith). In the following figures the transducer numbers were not depicted for clarity.

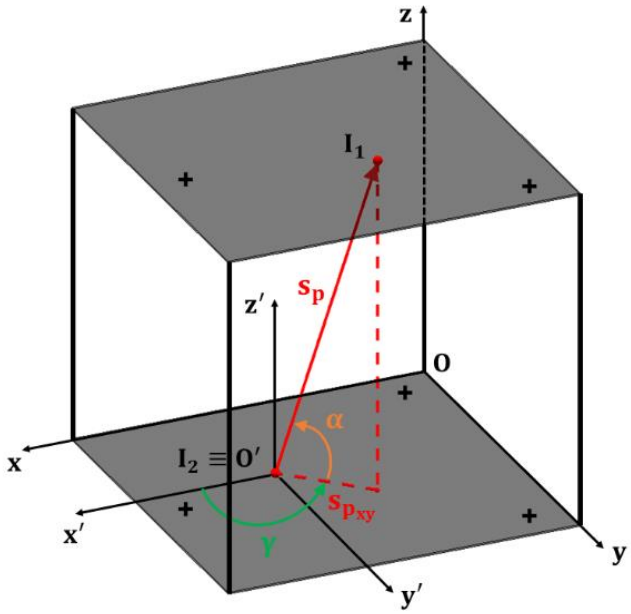

Figure 4. Coordinate systems for the estimation of the space debris direction.

The particle trajectory coincides with the direction of the vector joining points I_1 and I_2, which are the location impact on the top and bottom plates, respectively. The position vector $\boldsymbol{s_p}$ points from I_2 to I_1 and can be identified by the three vector components (or projections) with respect to the $Oxyz$ axes:

$$\boldsymbol{s_p} = s_{p_x}\,\hat{\boldsymbol{\imath}} + s_{p_y}\,\hat{\boldsymbol{\jmath}} + s_{p_z}\,\hat{\boldsymbol{k}}\,, \tag{10}$$

where $[\hat{\boldsymbol{\imath}} \quad \hat{\boldsymbol{\jmath}} \quad \hat{\boldsymbol{k}}]$ represent the unit vectors of the three axes. In terms of coordinates of the two impact points, Eq. (10) can be rewritten as:

$$\boldsymbol{s_p} = (x_1 - x_2)\,\hat{\boldsymbol{\imath}} + (y_1 - y_2)\,\hat{\boldsymbol{\jmath}} + (z_1 - z_2)\,\hat{\boldsymbol{k}}\,. \tag{11}$$

The magnitude (or modulus) of the position vector can be calculated as shown below:

$$s_p = \sqrt{(x_1 - x_2)^2 + (y_1 - y_2)^2 + (z_1 - z_2)^2}\,. \tag{12}$$

The unknown angles are visualised by considering a Cartesian coordinate system with the impact location at the bottom plate as the new origin, i.e. a translated system with respect to the original one. The reference direction for the azimuth

angle is the *x*-axis and it is measured counter clockwise from this axis towards the *y*-axis. The three components of the position vector $\boldsymbol{s_p}$ are related to its magnitude by the following system of equations:

$$\begin{cases} s_{p_x} = s_p \ cos\,\alpha \ cos\,\gamma \\ s_{p_y} = s_p \ cos\,\alpha \ sin\,\gamma \\ s_{p_z} = \ s_p \ sin\,\alpha \end{cases} . \tag{13}$$

The elevation angle α can be computed by the third equation of system (13):

$$\alpha = sin^{-1}\left(\frac{s_{p_z}}{s_p}\right) = sin^{-1}\left(\frac{z_2 - z_1}{\sqrt{(x_2 - x_1)^2 + (y_2 - y_1)^2 + (z_2 - z_1)^2}}\right), \tag{14}$$

whereas the azimuth angle γ can be calculated by using the first and second equation of system (13):

$$\gamma = tan^{-1}\left(\frac{s_{p_y}}{s_{p_x}}\right) = tan^{-1}\left(\frac{y_2 - y_1}{x_2 - x_1}\right). \tag{15}$$

4 ESTIMATION OF THE SPACE DEBRIS VELOCITY

Since TR method provides the impact location on both plates (see Section 3.1), it is possible to calculate the distance between the impact point and the sensor location on both plates, obtaining $N = 3$ values for r_1 and r_2. Only two elements are still unknown in the velocity formulation of the debris particle [Eq. (4)]: i.e. the time difference Δt of the signals acquired by a couple of transducers located at the same positions on the two plates and the wave velocities on both plates at transducer locations. The methodology to obtain time differences Δt and wave speeds is reported in the following two sub-sections.

4.1 TIME DIFFERENCES OF ARRIVAL ESTIMATION

Several methods are present in literature to compute the time difference between measured elastic signals, which are based on direct calculation using the cross-correlation technique [35] or by simple difference between TOAs. In the latter

case, the objective is to estimate the TOAs with high level of accuracy [30]. The TOA, also called "onset time" of transient signals such as acoustic emissions, seismograms or ultrasound, can be described as the time when the ballistic wave originated at the impact source reaches one (or more) receiving sensor. The TOA is usually referred to as the time where the first difference between the signal and the noise takes place. The proposed research work used an estimation approach based on the Akaike Information Criterion (AIC) that, unlike traditional TOA identification techniques, it allows identifying the onset time with high accuracy in the range of microseconds. A detailed explanation of the AIC theory and derived automatic pickers able to identify the TOA of a signal is reported in [30] and [38-41]. The main assumption for the AIC method is to consider the signal, or a general time series, as divided in two different locally stationary segments, each modelled as an autoregressive (AR) process. The first segment is the non-informative part, and it is called "noise", while the second one is the informative part, and it is called "signal". These two datasets are separated by the onset time, which can be regarded as the global minimum of the following AIC function, called "Maeda's relation" [42]:

$$AIC(k) = k\,ln\big(var(x[1,k])\big) + (n-k-1)\,ln\big(var(x[k+1,n])\big)\,, \qquad (16)$$

where x represents the time series (the signal), k represents the range through all points of the signal and $var(\cdot)$ is the sample variance of the signal. In this work the so-called "characteristic function AIC picker" based on Eq. (16) was chosen [30, 43, 44]. The name is due to a suitable mathematical function, called "characteristic function" (CF), whose purpose is to improve the resolution level between noise and signal through the enhancement of changes in signal features [45] such as the frequency, the amplitude or both. In correspondence of these changes, it is possible to detect the time of arrival of the signal. For this reason, the performance of the picker highly depends on the chosen characteristic function. Among all characteristic functions used in literature, in this research work the following function suitable for thin plates was chosen [43, 44]:

$$CF(i) = |x(i)| + R\,|x(i) - x(i-1)|\,, \tag{17}$$

where R is a constant. The algorithm is divided into two steps (see Figure 5), consisting of a first rough estimation of the onset time during the first step, with a more precise determination of it during the second step. The first step starts with the determination of a shortened time window, which is illustrated in Figure 5a as the range between the two cyan lines. The starting time was set at the beginning of the original signal within the noise level. The ending time was set after the global maximum of the characteristic function (17), t_{MAX}, on time $t_{MAX} + \Delta t_{AM}$. The time delay Δt_{AM} is a value depending on the tested material, set to 20 μs for our experiment and suitable for CFRP thin-plate specimens in accordance to [43, 44]. Maeda's relation (16), with the characteristic function (17) as input, is applied to this time window so that the first onset time, t_{MIN}, is determined. The accuracy of the AIC picker is increased by focusing on the neighbourhood of the first estimation. A new time window is considered, whose limits are $t_{MIN} - \Delta t_{FB}$ and $t_{MIN} + \Delta t_{FA}$ (see Figure 5b), where the setting are $\Delta t_{FB} = 30$ μs and $\Delta t_{FA} = 10$ μs, chosen according to [43, 44]. A new application of Eq. (16) on this new time window defines the actual time of arrival (see Figure 5c).

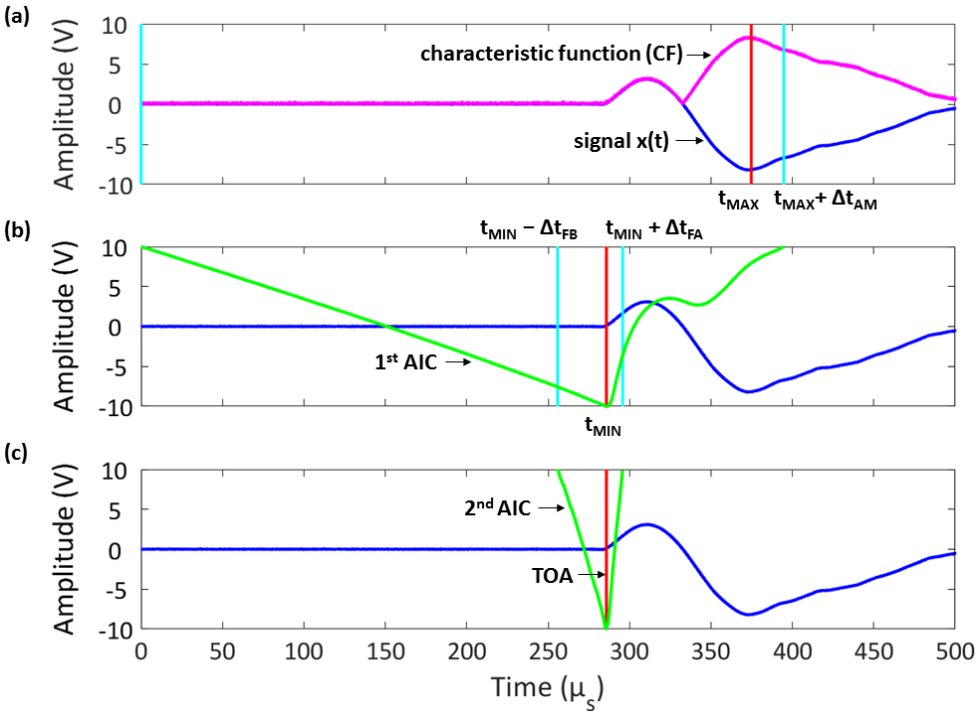

Figure 5. Visual description of CF-AIC picker: determination of the initial time window (a); estimation of the first TOA and determination of the second time window (b); estimation of the final TOA (c).

4.2 WAVE VELOCITY CALCULATION

For CFRP composites with different lay-ups, the propagating wave velocity is not constant and depends on the wave propagation direction. The angular-group velocity relationship of most aeronautical cross-ply composites is defined as "elliptical" or "quasi-elliptical", i.e. the group speed versus the propagation angle θ follows an elliptical shape [46]. Group velocities or wave fronts of elliptical shape have the advantage of requiring only two velocity measurements related to the speed in the fibre direction (V_{0°) and transverse to fibres (V_{90°). The elliptical wave velocity pattern can be described by the following equation [46]:

$$V(\theta) = \frac{V_{0^\circ}\ V_{90^\circ}}{\sqrt{(V_{0^\circ}\ sin\,\theta)^2 + (V_{90^\circ}\, cos\,\theta)^2}}. \qquad (18)$$

Since the two composite plates used are identical, an initial calibration process is necessary to confirm the assumption of "elliptical angular-group velocity pattern". Following this calibration, it was possible to evaluate the velocities related to the $N = 3$ propagation angles θ, whose values are calculated based on the fibre direction, sensor locations and the position of the acoustic source (i.e. the calculated impact). As shown in Figure 6, the angular measurements are computed counter clockwise from the longitudinal fibre direction to the line joining the acoustic source and the single receiver transducer.

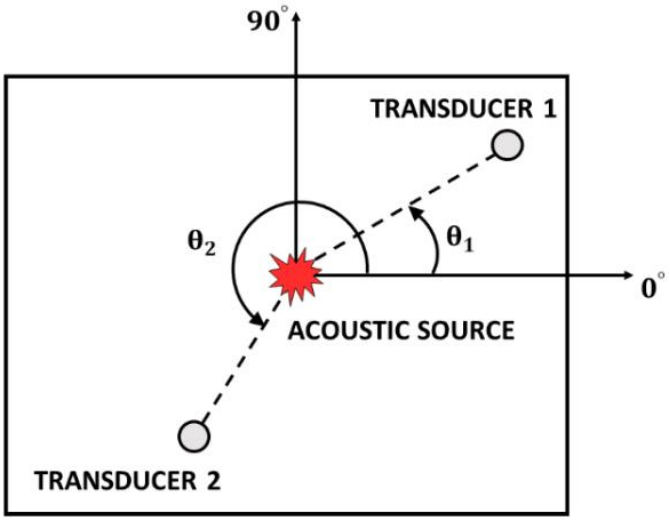

Figure 6. Reference system for the calculation of propagation angles θ.

5 EXPERIMENTAL SET-UP

Two CFRP composite plates with dimensions of $200\ \text{mm} \times 200\ \text{mm}$ were fabricated (Figure 7), each including three embedded PZT transducers for the reception of elastic waves (Figure 8a). Samples were made using four layers of unidirectional carbon/epoxy (T800/M21) prepregs. As illustrated in Figure 8b, the lay-up used was $[90^{\circ}/0^{\circ}]_{s}$ giving a plate thickness of around 1.3 mm. The PZTs were placed at the interface between the two middle layers during the lay-up process. To avoid the creation of short-circuits, the contact between the PZTs and the electrically conductive carbon fibres was prevented using an insulation

technique proposed in a previous study of the authors [24]. Specifically, the top (conductive) surface of each PZT was covered with a single layer (10 mm × 10 mm) of woven E-glass fibre fabric. Regarding to the wires soldered to the anode and the cathode of the PZTs, their free ends were directed outside the top surface of the plates by passing them through small incisions in the fibre directions of the two plies above the PZTs. In this way, fibre cutting was avoided and distortions of the internal plate structure were minimised. Plates were cured using standard autoclave process for 120 minutes at a pressure of 0.7 MPa and a temperature of 150° C with a ramp rate of 3° C per minute. After completion of the curing process, the wire ends were attached to 50 Ω Bayonet Neill-Concelman (BNC) connectors using low noise cables (RG174/U).

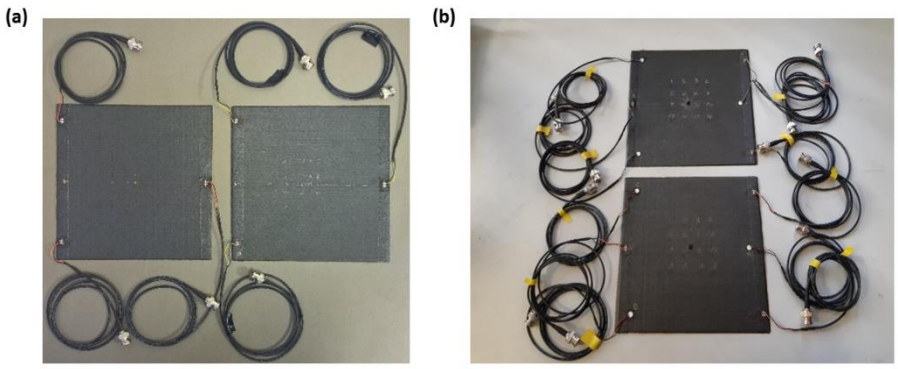

Figure 7. Manufactured CFRP composite plates with embedded PZT transducers: intact samples (a) and post-impacted samples (b).

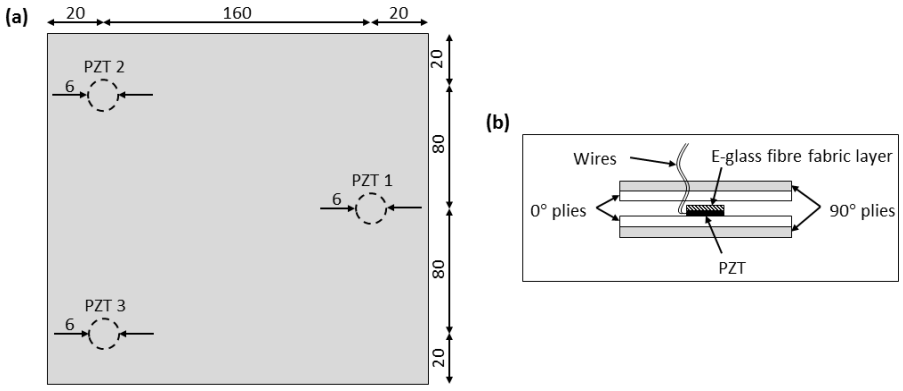

Figure 8. Positions of embedded PZTs in CFRP plate (a); lay-up of CFRP plate with embedded PZTs (b).

As reported in Section 3, for the TR process the Cartesian reference frame was chosen with the origin at the left bottom corner of the bottom CFRP plate. The monitoring area consisted of a grid arranged with equally spaced (20 mm) nodes. As shown in Figure 11, the distance between the two parallel plates was 190 mm, and each plate was fixed at the four corners. In order to validate the experimental campaign with reproducible experiments, low-velocity impact tests were performed by using an impact machine with an impactor of around 2.7 kg instrumented with a sharp tip. The impactor was drop from a height of 1000 mm above the top plate with a maximum impact energy of around 26 J. This allowed the impactor to reach an estimated mean velocity between the two plates equal to 4.2 m/s (~15 km/h). As reported in Section 3.1, the use of low-velocity impacts did not compromise the validity of the proposed SCODD system. Elastic signals were acquired using two linked four-channel oscilloscopes with 16 bits of resolution, a sampling rate of 2 MHz and an acquisition window of 0.2 sec. All algorithms were implemented by the authors using a MATLAB software code and the computational time is ~2 sec.

6 RESULTS

The results section is divided into two sub-sections: in Section 6.1 the material characterisation process for the wave velocity estimation is shown, whilst in Section 6.2 the results obtained from three different impact tests with different direction parameters are presented. The accuracy of the impact localisation method is expressed by the following formula for the location error, Ψ [30]:

$$\Psi = \sqrt{(x_{real} - x_{calculated})^2 + (y_{real} - y_{calculated})^2}\,, \tag{19}$$

where (x_{real}, y_{real}) are the coordinates of the true impact position and $(x_{calculated}, y_{calculated})$ are the coordinates of the impact location calculated by using the time reversal method.

6.1 CALIBRATION ANGULAR – GROUP VELOCITY PATTERN

A calibration process necessary to evaluate the pattern of the group wave velocity in the CFRP plate was initially carried out (Figure 9). Impacts were performed at the centre of the plate by using a hand-held instrumented hammer (sensitivity factor $= 2.215 \frac{\text{mV}}{\text{N}}$) connected to a signal conditioner manufactured by Meggitt-Endevco. Two acoustic emission transducers (S_1 and S_2) of 150 kHz central frequency were placed at a distance of 50 and 70 mm from the impact location, respectively. The distance between the centres of the two transducers was around 20 mm. The direction of the wave propagation was identified by the angle between the line joining the impact point and the two transducers and the longitudinal fibre direction (0°). Four impacts were performed at each direction, starting from 0° and proceeding counter clockwise with 15° intervals, therefore 24 directions were considered to cover all the plate. A total of 192 ($4 \times 2 \times 24$) signals were available at the end of the calibration process.

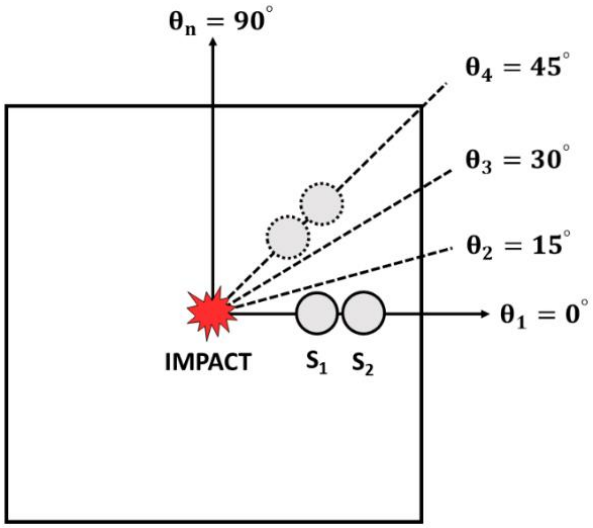

Figure 9. Experimental set-up for the material characterisation process.

Group velocities were estimated from the distance between the transducers (fixed for each direction) and the difference in TOA between the two acquired signals. TOA was calculated using the AIC picker described in Section 4.1. At each

direction, the mean velocity was calculated using the four obtained values. In Figure 10, the comparison between the experimental velocity values and the theoretical ones obtained by using Eq. (18) is shown. Good agreement between the experimentally calculated values and the elliptical pattern of the wave velocity was found, with a maximum difference of ~20 m/s.

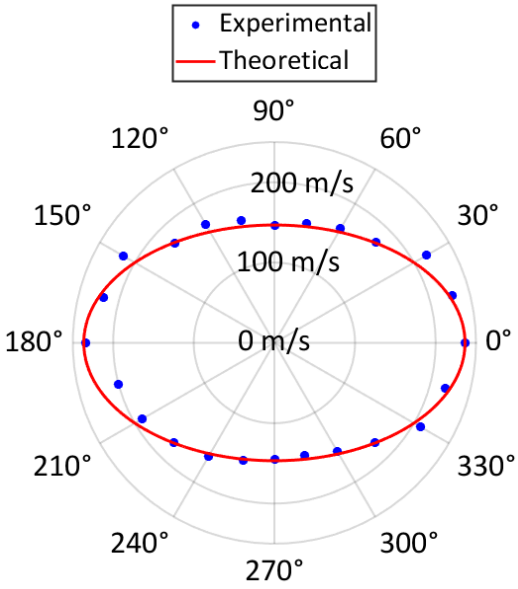

Figure 10. Comparison among the experimental wave velocity values and the theoretical ones by using Eq. (18).

6.2 SCODD TEST RESULTS

SCODD results from three different experimental impact tests are here shown. Each test was related to the two impacts on both plates. The direction of the first impact was perpendicular to the two CFRP plates, therefore an elevation angle equal to 90° was expected, whilst the other two tests revealed elevation values associated with the geometry of both detector and impactor. It should be noted that in a space environment the high velocity of a piece of debris can be considered almost constant between the two plates, whilst in the performed experimental tests, the velocity of the impactor tip changes linearly due to the gravitational field. Hence, an average

speed of the impactor between the two plates was considered for the experimental tests.

6.2.1 Test 1 – Perpendicular impact

Figure 11 shows the high accuracy of TR method for the impact localisation, with an error less than 1 mm for both plates [see Eq. (19) and Table 1]. A summary of results is reported in Table 1.

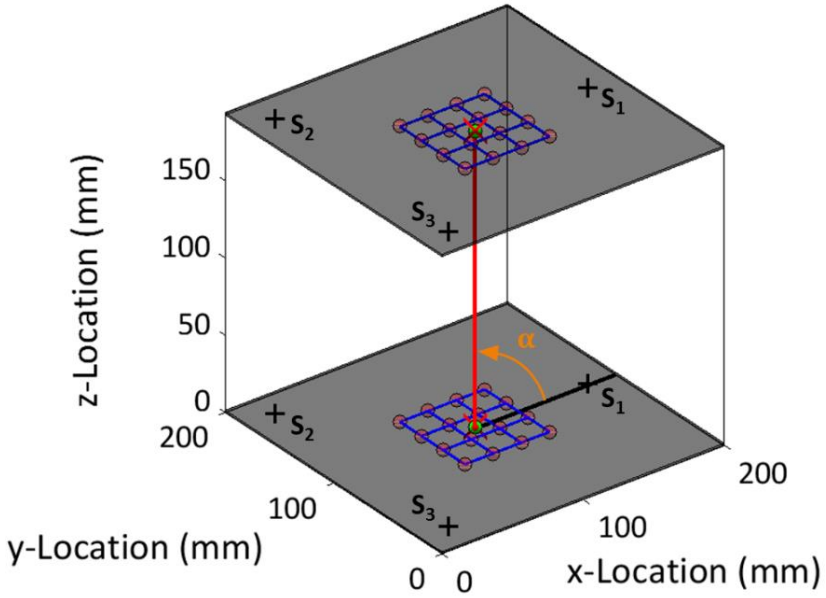

Figure 11. Test 1 – Direction estimation and localisation of the impacts on the two plates (real impact locations are shown as green circles, whilst the calculated ones are depicted with red crosses). Calibration points are shown with red circles.

As expected, the elevation angle was almost 90°. Since the direction is perpendicular to both plates, each line of the reference plane (the bottom plate) passing through the impact point was used as the reference line for the calculation of the elevation angle. In Figure 11, the *x*-axis was used as reference line. As previously stated, the azimuth angle is not defined if the elevation angle is equal to 90°. The difference between the true azimuth angle (not defined) and the calculated one presented in Table 1 is due to the presence of a small projection of $\boldsymbol{s_p}$ (not perfectly perpendicular to both plates) on the reference *xy*-plane.

Table 1. Test 1 – Direction parameters and impact localisation results.

	Top plate		Bottom plate	
	x-Coord (mm)	y-Coord (mm)	x-Coord (mm)	y-Coord (mm)
Current impact	100	100	100	100
Calculated impact	100.06	99.88	100.1	99.9
Location error Ψ (mm)	0.13		0.14	
	True		Calculated	
s_p (mm)	191.3		191.3	
Azimuth angle γ	ND		246.55°	
Elevation angle α	90°		89.96°	

The velocity values of the impacting object and the parameters necessary for their calculation are reported in Table 2. Acquired signals on both plates are depicted in Figure 12. The average value among the three calculated velocity values is around 4.35 m/s that is very similar to the mean velocity of 4.2 m/s as reported in Section 5.

Table 2. Test 1 – Velocity results.

	Transducer 1		Transducer 2		Transducer 3	
	Top plate	Bottom plate	Top plate	Bottom plate	Top plate	Bottom plate
d_{I-S} (mm)	79.94	79.9	113.26	113.22	113.09	113.21
θ_{I-S}	0.08°	0°	134.98°	135.03°	224.94°	224.96°
V_w (m/s)	236.36	236.36	176.25	176.33	176.36	176.33
Δt (s)	0.0439		0.0434		0.0446	
V_p (m/s)	4.36		4.41		4.29	

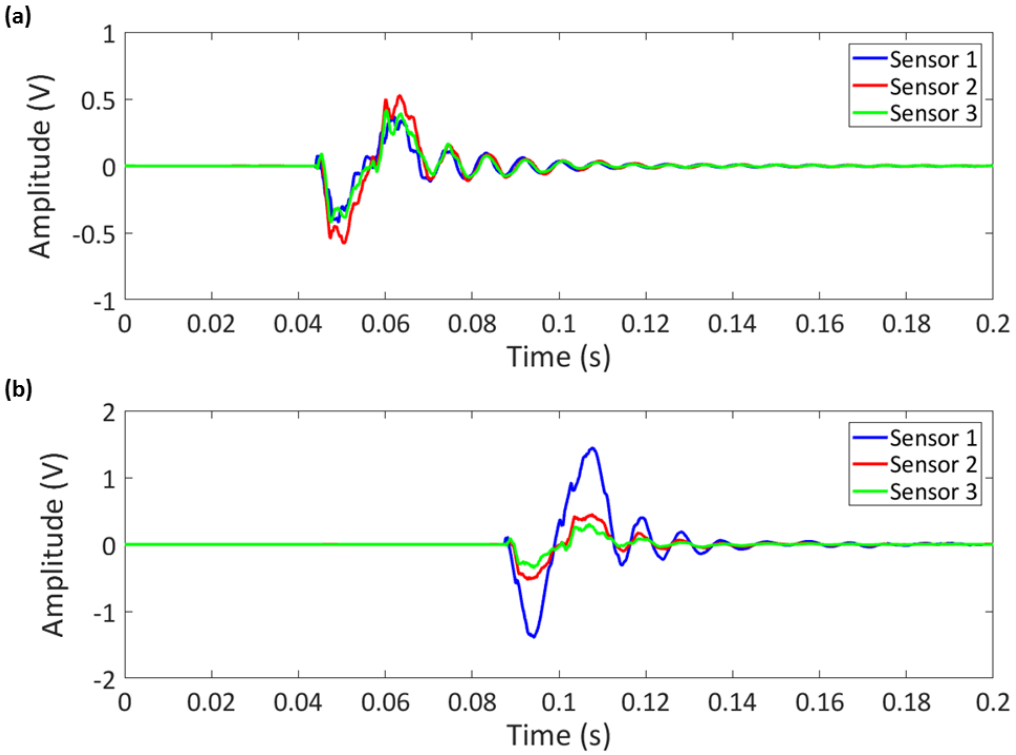

Figure 12. Test 1 – Signals acquired by transducers on the top plate (a) and on the bottom plate (b).

6.2.2 Test 2 – Skewed impact 1

The impact test 2 is represented in Figure 13, which shows the direction of impacts, azimuth and elevation angles, the true and calculated impacts and calibration points used for the TR algorithm. Experimental results are summarised in Table 3 and Table 4.

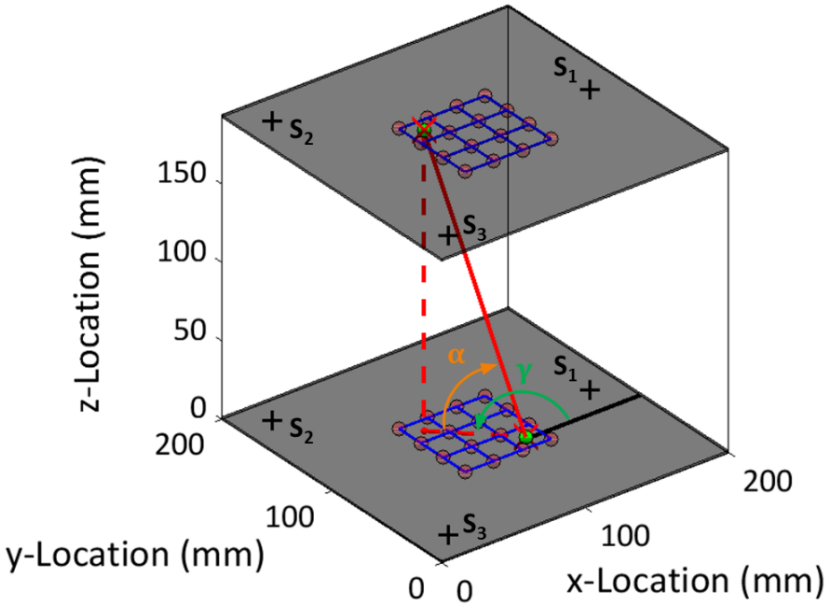

Figure 13. Test 2 – Direction estimation and localisation of the impacts on the two plates (real impact locations are shown as green circles, whilst the calculated ones are depicted with red crosses). Calibration points are shown with red circles.

Table 3. Test 2 – Direction parameters and impact localisation results.

	Top plate		Bottom plate	
	x-Coord (mm)	y-Coord (mm)	x-Coord (mm)	y-Coord (mm)
Current impact	80	120	120	80
Calculated impact	79.68	119.99	120	80.01
Location error Ψ (mm)	0.32		0.01	
	True		Calculated	
s_p (mm)	200		199.5	
Azimuth angle γ	135°		135.24°	
Elevation angle α	74°		73.47°	

Table 4. Test 2 – Velocity results.

	Transducer 1		Transducer 2		Transducer 3	
	Top plate	Bottom plate	Top plate	Bottom plate	Top plate	Bottom plate
d_{I-S} (mm)	102.3	63.24	84.63	141.41	116.45	116.62
θ_{I-S}	348.73°	18.42°	134.84°	135°	239.17°	210.97°
V_w (m/s)	229.47	219.52	176.06	176.28	160.21	198.17
Δt (s)	0.0472		0.0481		0.0479	
V_p (m/s)	4.21		4.18		4.15	

As in Test 1, the calculated velocities are comparable with the mean velocity between real impacts occurred on the two plates.

6.2.3 Test 3 – Skewed impact 2

Results from the third impact test are presented in Figure 14, Table 5 and Table 6. Impactor velocities are very similar to the values obtained in the previous Test 2. This is because impacts in Tests 2 and 3 occurred in symmetrical positions on both plates. Therefore elevation values are the same, whereas the azimuth angle in Test 3 is phased of 180^0 with respect to Test 2. As before, the obtained velocities are comparable to the real mean velocity between the two impacts.

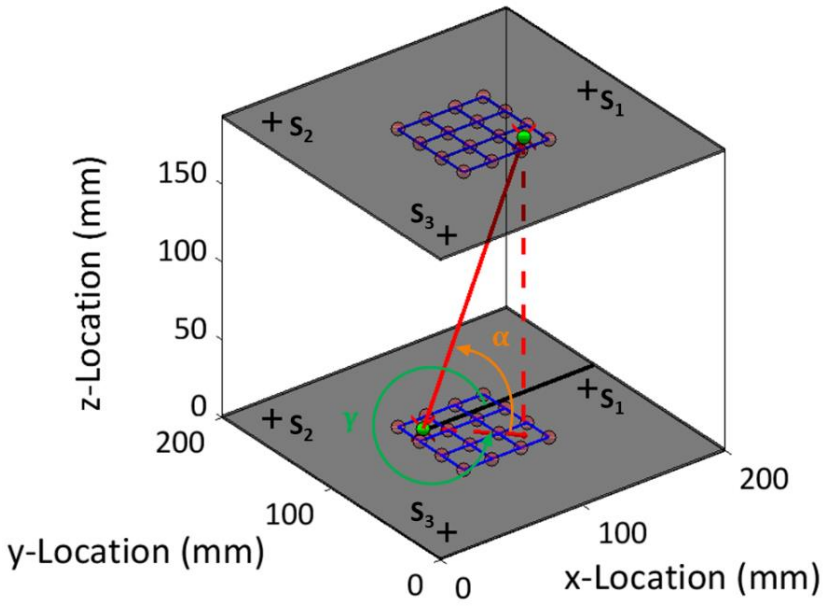

Figure 14. Test 3 – Direction estimation and localisation of the impacts on the two plates (real impact locations are shown as green circles, whilst the calculated ones are depicted with red crosses). Calibration points are shown with red circles.

Table 5. Test 3 – Direction parameters and impact localisation results.

	Top plate		Bottom plate	
	x-Coordinate (mm)	y-Coordinate (mm)	x-Coordinate (mm)	y-Coordinate (mm)
Current impact	120	80	80	120
Calculated impact	120.24	80.38	80.05	119.98
Location error Ψ (mm)	0.45		0.05	
	True		Calculated	
s_p (mm)	200		199.4	
Azimuth angle γ	315°		315.42°	
Elevation angle α	74°		73.57°	

Table 6. Test 3 – Velocity results.

	Transducer 1		Transducer 2		Transducer 3	
	Top plate	Bottom plate	Top plate	Bottom plate	Top plate	Bottom plate
d_{I-S} (mm)	62.9	101.92	141.32	84.9	117.02	116.63
θ_{I-S}	18.18°	348.69°	135.18°	135.02°	211.06°	239.01°
V_w (m/s)	219.9	229.43	176.52	176.3	198.01	160.36
Δt (s)	0.0471		0.0475		0.0474	
V_p (m/s)	4.25		4.17		4.21	

7 CONCLUSIONS

This paper presented the experimental results to demonstrate the proof of concept of a novel *in-situ* and lightweight smart composite orbital debris detector (SCODD) for the localisation of space debris impacts and the estimation of debris particles' direction and velocity. The SCODD system consisted of two fixed parallel CFPR composite plates instrumented with three embedded piezoelectric transducers. The coordinates of impact locations on both plates were calculated by processing the measured acoustic emissions with the time reversal method. The difference in arrival times between signals acquired by two transducers at the same positions on both plates was used to compute the velocity of the particle. The Akaike Information Criterion picker was employed to determine the arrival times with high accuracy. For the estimation of the space debris velocity, a calibration process was initially performed to evaluate the angular-group velocity elliptical pattern of elastic waves propagating into the plates. A number of experimental tests with impacts applied at different directions was then performed using the SCODD system. Results indicated accurate calculation of the impact directions and velocities, thus demonstrating the effectiveness of the proposed debris detection system for future Earth satellites by reducing the risk of collision and enhancing the orbital lifetime.

ACKNOWLEDGEMENTS

This paper has been funded by the EXTREME project of the European Union's Horizon 2020 research and innovation programme under grant agreement No. 636549.

REFERENCES

1. Tonetti, S., Cornara, S., Faenza, M., Verberne, O., Langener, T., & de Miguel, G. V. (2018). Active Debris Removal and Space Debris Mitigation using Hybrid Propulsion Solutions. In *Stardust Final Conference* (pp. 163-180). Springer, Cham.
2. Pelton, J. N. (2013). *Space debris and other threats from outer space*. New York: Springer.
3. Mespoulet, J., Héreil, P. L., Abdulhamid, H., Deconinck, P., & Puillet, C. (2017). Experimental study of hypervelocity impacts on space shields above 8 km/s. *Procedia Engineering*, *204*, 508-515.
4. Liu, M., Su, Z., Zhang, Q., & Long, R. (2016). Modeling hypervelocity-impact-induced shock waves for characterizing orbital debris-produced damage. *Journal of Applied Mechanics*, *83*(8), 081010.
5. Liu, M., Wang, Q., Zhang, Q., Long, R., & Su, Z. (2018). Characterizing hypervelocity (> 2.5 km/s)-impact-engendered damage in shielding structures using in-situ acoustic emission: Simulation and experiment. *International Journal of Impact Engineering*, *111*, 273-284.
6. Christiansen, E. L., Nagy, K., Lear, D. M., & Prior, T. G. (2009). Space station MMOD shielding. *Acta Astronautica*, *65*(7-8), 921-929.
7. Porfilio, M., Piergentili, F., & Graziani, F. (2004). First optical space debris detection campaign in Italy. *Advances in Space Research*, *34*(5), 921-926.
8. Lederer, S. M., Stansbery, E. G., Cowardin, H. M., Hickson, P., Pace, L. F., Abercromby, K. J., & Alliss, R. J. (2013). The NASA meter class autonomous telescope: Ascension island. *National Aeronautics and Space administration Houston TX Lyndon B Johnson Space Center*.
9. Cooke, W., Matney, M., Moorhead, A. V., & Vavrin, A. (2017). A Comparison of Damaging Meteoroid and Orbital Debris Fluxes in Earth Orbit. In *7th European Conference on Space Debris; 18-21 Apr. 2017; Darmstadt; Germany*.
10. Matney, M. J. (2017). Algorithms for the Computation of Debris Risk. In *7th European*

Conference on Space Debris; 18-21 Apr. 2017; Darmstadt; Germany.

11. Krisko, P. H., Flegel, S., Matney, M. J., Jarkey, D. R., & Braun, V. (2015). ORDEM 3.0 and MASTER-2009 modeled debris population comparison. *Acta Astronautica*, *113*, 204-211.
12. Benvenuto, R., Lavagna, M., Schlotterer, M., & Theil, S. (2017). Experimental setup and tests' results for uncooperative objects capture and manoeuvring with robotic arm. In *7th European Conference on Space Debris; 18-21 Apr. 2017; Darmstadt; Germany.*
13. Astromaterials Research and Exploration Science. Hypervelocity Impact Technology: Shield Development Basic Concepts. National Aeronautics and Space Administration.
14. Palla, C., Kingston, J., & Hobbs, S. (2017). Development of commercial drag-augmentation systems for small satellites. In *7th European Conference on Space Debris; 18-21 Apr. 2017; Darmstadt; Germany.*
15. Axthelm. R., Klotz, B., Retat, I., & Schlossstein, U. (2017). Net Capture Mechanism for Debris Removal Demonstration Mission. In *7th European Conference on Space Debris; 18-21 Apr. 2017; Darmstadt; Germany.*
16. Burchell, M. J., Standen, S., Cole, M. J., Corsaro, R. D., Giovane, F., Liou, J. C., & Stansbery, E. (2011). Acoustic response of aluminium and Duroid plates to hypervelocity impacts. *International Journal of Impact Engineering*, *38*(6), 426-433.
17. Burchell, M. J., Corsaro, R., Giovane, F., Cole, M., Sadilek, A., Price, M. C., & Liou, J. C. (2013). A New Cosmic Dust Detector with a Novel Method Using a Resistive Grid Sensitive to Hypervelocity Impacts. *Procedia Engineering*, *58*, 68-76.
18. Bauer, W., Romberg, O., Wiedemann, C., Drolshagen, G., & Vörsmann, P. (2014). Development of in-situ space debris detector. *Advances in Space Research*, *54*(9), 1858-1869.
19. Forli, O. (1990). In orbit in-service inspection. *ESA, Space Applications of Advanced Structural Materials p 157-161(SEE N 91-11812 03-24)*.
20. Schäfer, F., & Janovsky, R. (2007). Impact sensor network for detection of hypervelocity impacts on spacecraft. *Acta Astronautica*, *61*(10), 901-911.
21. Graziani, F., Porfilio, M., & Santoni, F. (2005) An in situ impact sensor on board a UNISAT microsatellite for monitoring the microparticles environment. *http://techrepots. larc. nasa. gov*.
22. Kobayashi, M., Krüger, H., Senshu, H., Wada, K., Okudaira, O., Sasaki, S., & Kimura, H. (2018). In situ observations of dust particles in Martian dust belts using a large-sensitive-area dust sensor. *Planetary and Space Science*, *156*, 41-46.

23. Corsaro, R. D., Giovane, F., Liou, J. C., Burchell, M. J., Cole, M. J., Williams, E. G., & Anderson, C. R. (2016). Characterization of space dust using acoustic impact detection. *The Journal of the Acoustical Society of America*, *140*(2), 1429-1438.

24. Andreades, C., Mahmoodi, P., & Ciampa, F. (2018). Characterisation of Smart CFRP Composites with Embedded PZT Transducers for Nonlinear Ultrasonic Applications. *Composite Structures*.

25. Ciampa, F., & Meo, M. (2012). Impact detection in anisotropic materials using a time reversal approach. *Structural Health Monitoring*, *11*(1), 43-49.

26. Ciampa, F., & Meo, M. (2014). Impact localization on a composite tail rotor blade using an inverse filtering approach. *Journal of Intelligent Material Systems and Structures*, *25*(15), 1950-1958.

27. Ciampa, F., Boccardi S., & Meo, M. (2016). Factors affecting the imaging of the impact location with inverse filtering and diffuse wave fields. *Journal of Intelligent Material Systems and Structures*, *27*(11), 1523-1533.

28. De Simone, M. E., Ciampa, F., & Meo, M. (2019). A hierarchical method for the impact force reconstruction in composite structures. *Smart Materials and Structures*, *28*(8).

29. De Simone, M. E., Ciampa, F., & Meo, M. (2019). A hierarchical impact force reconstruction method for Aerospace composites. In *Key Engineering Materials* (Vol. 812, pp. 17-24). Trans Tech Publications Ltd.

30. De Simone, M. E., Ciampa, F., Boccardi, S., & Meo, M. (2017). Impact source localisation in aerospace composite structures. *Smart Materials and Structures*, *26*(12).

31. Meo, M., Zumpano, G., Piggott, M., & Marengo, G. (2005). Impact identification on a sandwich plate from wave propagation responses. *Composite structures*, *71*(3-4), 302-306.

32. Ciampa, F., & Meo, M. (2010). Acoustic emission source localization and velocity determination of the fundamental mode A_0 using wavelet analysis and a Newton-based optimization technique. *Smart Materials and Structures*, *19*(4), 045027.

33. Ciampa, F., & Meo, M. (2010). A new algorithm for acoustic emission localization and flexural group velocity determination in anisotropic structures. *Composites Part A: Applied Science and Manufacturing*, *41*(12), 1777-1786.

34. Ciampa, F., Meo, M., & Barbieri, E. (2012). Impact localization in composite structures of arbitrary cross section. *Structural Health Monitoring*, *11*(6), 643-655.

35. Kundu, T. (2014). Acoustic source localization. *Ultrasonics*, *54*(1), 25-38.

36. Chen, C., Li, Y., & Yuan, F. G. (2012). Impact source identification in finite isotropic plates

using a time-reversal method: experimental study. *Smart Materials and Structures*, *21*(10), 105025.

37. Xu, L., Wang, Y., Cai, Y., Wu, Z., & Peng, W. (2016). Determination of impact events on a plate-like composite structure. *The Aeronautical Journal*, *120*(1228), 984-1004.

38. Akaike, H. (1973). Information theory and an extension of the maximum likelihood principle. In: BN Petrov, F Csaki, editors, *Second international symposium on information theory*, Springer-Verlag, 267-281.

39. Akaike, H. (1974). Markovian representation of stochastic processes and its application to the analysis of autoregressive moving average processes. *Annals of the Institute of Statistical Mathematics*, *26*(1), 363-387.

40. Akaike, H. (1974). A new look at the statistical model identification. *IEEE transactions on automatic control*, *19*(6), 716-723.

41. Kitagawa, G., & Akaike, H. (1978). A procedure for the modeling of non-stationary time series. *Annals of the Institute of Statistical Mathematics*, *30*(1), 351-363.

42. Maeda, N. (1985). A method for reading and checking phase times in auto-processing system of seismic wave data. *Zisin*, *38*(3), 365-379.

43. Sedlak, P., Hirose, Y., Khan, S. A., Enoki, M., & Sikula, J. (2009). New automatic localization technique of acoustic emission signals in thin metal plates. *Ultrasonics*, *49*(2), 254-262.

44. Sedlak, P., Hirose, Y., & Enoki, M. (2013). Acoustic emission localization in thin multi-layer plates using first-arrival determination. *Mechanical Systems and Signal Processing*, *36*(2), 636-649.

45. Allen, R. (1982). Automatic phase pickers: Their present use and future prospects. *Bulletin of the Seismological Society of America*, *72*(6B), S225-S242.

46. Paget, C. A., Atherton, K., & O'Brien, E. (2003, September). Triangulation algorithm for damage location in aeronautical composite structures. In *Proceedings of the 4th International Workshop on Structural Health Monitoring (F. Chang, ed.), (Stanford, CA, USA)* (pp. 363-370).

Chapter 7

Signal power method for the impact localisation in composites

In previous Chapters of this research work, two impact localisation method were illustrated. Each of them presents some peculiar characteristics and it is suitable for both isotropic and composite structural components.

The linearised impact localisation method (see Chapter 3) provides the coordinates of a low-velocity impact without a-priori knowledge of the mechanical properties of the material, including the wave speed, with the only hypothesis of not strongly inhomogeneous composite structures. No particular assumptions are required for isotropic structures. Furthermore, a particular configuration of four very closed to each other piezoelectric transducers is fundamental for the application of the algorithm.

Time reversal method (see Chapter 4 and Chapter 5) is suitable for most of aeronautical structures due to the presence of an initial calibration process, necessary for extracting information about the components under investigation. Despite the fundamental hypothesis of linear relation between the impact force and the structural responses, the method is able to furnish the impact location with high

accuracy also in case of real complex aeronautical composite structures, where at least material nonlinearities need to be taken in account.

The following publication provides an impact localisation algorithm in a very general situation where:

- composite components with unknown mechanical properties are considered (many of the methods presented in Chapter 2 cannot be applied);
- a set of transducers are located far from each other on the structure surface or inside the specimen (the linearised impact localisation method cannot be applied);
- a “structural” baseline of the component is not available (time reversal method cannot be applied).

The proposed method is based on the power of the acquired signal due to a low-velocity impact in a pre-determined time window including the first wave packets. A composite plate with embedded transducer is considered. The aim is to calculate the impact coordinates by a centre-of-gravity method involving the power distribution over the entire sample, calculated by a radial basis function approach able to interpolate the available power data related to the embedded transducer locations.

The results obtained after two experimental campaigns, the first performed by an instrumented impact hammer and the second by a small free-drop tower, showed the validity of the method able to identify the impact area, that is a circle having a radius of around 3-4 cm centred on the true impact point.

The Statement of Authorship Form and the paper can be found next.

This declaration concerns the article entitled:	
Acoustic emission localisation in composites using the signal power method and embedded transducers	
Publication status (tick one)	
Draft manuscript	
Submitted	
In review	
Accepted	
Published	✓
Candidate's contribution to the paper (detailed, and also given as a percentage)	
The candidate contributed to/ considerably contributed to/predominantly executed the…	
Formulation of ideas:	100% I proposed the entire idea, the hypothesis, the methodology approach and the experimental tests.
Design of methodology:	100% I designed all the algorithms used in the method and the experimental tests to be performed.
Experimental work:	50% All the experimental equipment and tests were provided by Dresden team. I performed the post-processing of the data and evaluated the algorithm results with the support of Stefano Cuomo, a new PhD student in Prof Meo's group. My supervisors helped me in results interpretation.

Presentation of data in journal format:	90% I decided structure, wrote all drafts, prepared all figures. Supervisors provided feedback on drafts and helped with submission, responses to reviews and publication process.

Statement from Candidate			
This paper reports on original research I conducted during the period of my Higher Degree by Research candidature.			
Signed	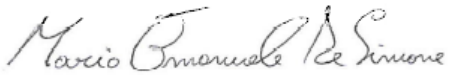	**Date**	26/06/2019

Acoustic emission localisation in composites using the signal power method and embedded transducers

Mario Emanuele DE SIMONE[a], Stefano CUOMO[a], Francesco CIAMPA[b], Michele MEO[a]*, Sandro NITSCHKE[c], Andreas HORNIG[c], Niels MODLER[c]

[a]Department of Mechanical Engineering, University of Bath, Bath, BA2 7AY, UK

[b]Department of Mechanical Engineering Sciences, University of Surrey, Guildford, GU2 7XH, UK

[c]Technische Universität Dresden, Institute of Lightweight Engineering and Polymer Technology, Holbeinstraße 3, 01307 Dresden, Germany

* corresponding author: m.meo@bath.ac.uk

Keywords: Impact localisation, radial basis functions, signal power method, composite materials, embedded transducers.

ABSTRACT

This work proposes a novel technique for the localisation of low-velocity impacts in composites without a-priori knowledge of the mechanical properties nor the speed of propagating waves, thus overcoming current limitations of existing impact localisation methods. The proposed algorithm is based on the estimation of the power of acoustic emissions generated by impacts on a composite plate instrumented with embedded piezo-transducers. The signal power values calculated at sparse sensor locations are interpolated over the sample by using radial basis function networks. The impact coordinates on the specimen surface are estimated by a centre-of-gravity method based on the interpolated power values. Experimental tests were performed by using both an instrumented impact hammer and a drop tower. The results obtained showed the validity of the presented approach, which was able to identify the impact locations with high level of accuracy.

1 INTRODUCTION

Low-velocity impact localisation in composite structures is currently a main concern for the aerospace engineering sector, as it is well known that such a class of materials are dramatically affected by out-of-plane impulsive loads. Indeed, despite their valuable in-plane mechanical properties, composite materials have low resistance towards low velocity impacts (LVI). Barely visible impact damage (BVID) caused by minimum energy impacts, could lead to a detriment of mechanical properties of the structures with possible catastrophic consequences. In this context, a technique capable to detect and localise impacts would make components and structures inspection faster with time savings in maintenance and operations.

Several impact identification approaches have been proposed in literature. Early works are based on the triangulation technique [1] and are limited to isotropic structures, homogeneous materials and known wave speed. Ciampa and Meo [2] introduced a modified version of the triangulation technique in isotropic materials without prior knowledge of the wave speed. Kundu et al. [3, 4] proposed an algorithm based on the minimisation of an error function, which was capable of locating the impact source in isotropic and anisotropic plate instrumented with four sensors. However, their algorithm required the knowledge of the direction dependence of the wave speed. Ciampa and Meo [5, 6] developed a technique, using six sensors, capable of localising the impact location in anisotropic plate without prior knowledge of the mechanical properties nor the wave velocity, by solving a set of nonlinear equations using a combination of local and global optimisation methods. De Simone and Ciampa [7] developed an impact localisation method suitable for both isotropic and composite samples, which also required no prior knowledge of the wave speed propagating in the test samples. Their method relies on an optimal configuration of four piezo transducers, which allows linearisation of well-known nonlinear system of equations for the estimation of the impact location. The Akaike information criterion (AIC) is used for the estimation of the time of arrival (TOA) of the elastic waves generated by the impact source.

Another approach able to identify the location of an impact event is the time reversal method, where impact localisation is achieved by measuring the structural response on a set of calibration points on the specimen and cross-correlating these recorded signals with the signal coming from an actual impact event [8-10]. The "impact cell" is estimated as the one with the maximum correlation coefficient, averaged among its corner points, and then the actual impact location is evaluated by a centre-of-gravity method [11, 12].

This paper proposed a new impact localisation algorithm based on the estimation of the signal power of measured elastic waves. The novelty of the proposed impact localisation system is its intrinsic capability to pinpoint the impact location without the knowledge of the wave velocity, whilst minimising the number of receiver sensors using radial basis functions (RBF) networks. A sparse array of piezo-sensors embedded in a composite plate were used to record acoustic emissions caused by the impact event and to estimate the signal power values. The RBF approach was specifically employed to interpolate the power of acquired signals over the surface of the test sample. The impact location was finally estimated by a centre-of-gravity method, involving all the power values and their spatial coordinates. As further remarks, this technique needs no material properties information, as well as wave speed dependency knowledge, neither a baseline calculated after a calibration process. It should be noted that the presented impact localisation method is suitable when a high number of receiving sensors is present on the structure for monitoring the impact events.

2 SIGNAL POWER METHOD

As described in the Introduction section, the main goal of this research work is the localisation of acoustic emissions sources in composite specimens when only the information of signals recorded after an impact event by a sparse array of N piezoelectric transducers is available. Furthermore, the piezo sensors are embedded inside the composite structure.

A signal power method was applied to overcome current limitations of existing impact localisation methods, in a similar way to [13]. Indeed, when a structure has abundant sensors for monitoring impact events, the signal power due to impact loading can provide a good estimation for the impact location.

The proposed algorithm is divided in three parts: the first one (see Section 2.1) consists of calculating the power values related to the acquired signals in a given time window. In the second part (see Section 2.2), an interpolation process performed by using the radial basis function (RBF) approach is achieved in order to evaluate a power distribution over the entire considered sample. The third part (see Section 2.3) provides the localisation of the impact event, which is achieved by the centre-of-gravity method involving the interpolated power values and their corresponding spatial coordinates on the specimen surface.

2.1 SIGNAL POWER CALCULATION

If a generic time signal $s(t)$ is considered, it is well known that its energy, in a given time window, can be defined as:

$$E(t) = \int_{t_0}^{t_f} |s(t)|^2 \, dt \,, \tag{1}$$

where t_0 and t_f represent respectively the initial and final time of the considered time window.

The power of the same signal is defined as the mean of the energy value calculated by Eq. (1) over the time window length, identified as $t_f - t_0$:

$$P(t) = \frac{1}{t_f - t_0} \int_{t_0}^{t_f} |s(t)|^2 \, dt \,, \tag{2}$$

Once recorded the signals due to the impact event, Eq. (2) is applied in order to obtain *N* power values corresponding to the *N* piezo sensor locations. In this research work, only the first wave packet of the recorded signals was considered in the power calculation, as it is possible to eliminate signal ambiguities (e.g. the

wave-reflections) considering a time window that includes only the first wave packets.

2.2 RADIAL BASIS FUNCTION INTERPOLATION

After the calculation of power value at each sensor location in the test sample, Park et al. [13] obtained a smooth power distribution by interpolation, so that the interpolating surface satisfied the bi-harmonic equation and therefore had minimum curvature. In this work, signal power values were used as input of the radial basis function (RBF) approach. Particularly, power values associated to an arbitrary set of *M* points over the sample surface were obtained by the knowledge of the *N* available power values, calculated as described in Section 2.1. The used RBF interpolation method is explained in detail in [14, 15].

In some recent works the authors demonstrated that hierarchical radial basis functions (RBFs) provide high accuracy in the data reconstruction when information related to a point on the structure is not available [11, 12]. In the proposed paper, the unknown data are the power values related to the *M* points on the sample surface, whose known spatial coordinates are the inputs of the RBF interpolation method, in addition to the known *N* power values to be interpolated and related to the sensor locations. The power value at each point on the sample was calculated by using the following augmented RBF interpolation considering a two-dimensional approach:

$$P(x_i, y_i) = \sum_{j=1}^{N} \lambda_j \, \phi\left(\sqrt{\left(x_i - x_j\right)^2 + \left(y_i - y_j\right)^2}\right) + \gamma_o + \gamma_1 x_i + \gamma_2 y_i \,, \quad 1 \le i \le M \,, \tag{3}$$

where x_i and y_i are coordinates of the i^{th} point of the arbitrary set of *M* points over the sample surface, x_j and y_j are coordinates of the j^{th} calibration point (where the power value necessary for the interpolation is known), λ_j and γ_k are the expansion coefficients and $\phi(\cdot)$ is a suitable radial basis function. The expansion coefficients were calculated as shown below, as solutions of a linear system of equations:

$$\begin{bmatrix} \lambda_1 \\ \vdots \\ \lambda_N \\ \gamma_1 \\ \gamma_2 \\ \gamma_o \end{bmatrix} = \begin{bmatrix} \phi_{1,1} & \dots & \phi_{1,N} & x_1 & y_1 & 1 \\ \vdots & \ddots & \vdots & \vdots & \vdots & \vdots \\ \phi_{N,1} & \dots & \phi_{N,N} & x_N & y_N & 1 \\ x_1 & \dots & x_N & 0 & 0 & 0 \\ y_1 & \dots & y_N & 0 & 0 & 0 \\ 1 & \dots & 1 & 0 & 0 & 0 \end{bmatrix}^{-1} \begin{bmatrix} P_1 \\ \vdots \\ P_N \\ 0 \\ 0 \\ 0 \end{bmatrix}, \quad (4)$$

where $P_1, \dots P_N$ are the power values at N transducer locations. As performed in other research works [11, 12] the thin plate spline (TPS), whose kernel is $\phi(\cdot) = (\cdot)^2 \, ln(\cdot)$, was used as radial basis function for its peculiar characteristics [16]. Once obtained the expansion coefficient values, they were substituted into Eq. (3) in order to calculate the power value at each point of the set *M*. The result of this process was the power distribution over the considered sample (see Figure 7).

2.3 IMPACT LOCALISATION

Once estimated the signal power values, the location of the impact event was estimated by a centre-of-gravity method [11, 12], involving the power values and the relative spatial coordinates [13]:

$$x_I = \frac{\sum_{i=1}^{M+N} x_i \, P_i}{\sum_{i=1}^{M+N} P_i}, \qquad y_I = \frac{\sum_{i=1}^{M+N} y_i \, P_i}{\sum_{i=1}^{M+N} P_i}, \quad (5)$$

where the calculation was performed considering the data from both the *N* calibration points and the arbitrary set of *M* points.

3 EXPERIMENTAL SET-UP

The investigated specimen panel, with dimensions 300 mm × 300 mm and cured thickness without piezo sensors equal to 1.52 mm, consists of 12 layers (0.11mm ply thickness) of Hexply 8552 UD prepreg material and one sensing layer (SL). The panel is manufactured within a vacuum press at 7 bar mould pressure and a two-step thermal curing cycle. The first ramp is from room temperature to 110°C, holding that temperature for one hour. The second ramp is to heat the panel to 180°C

and holds it for two hours after cooling it back to room temperature. The lay-up sequence is as follows: $[0_2/90_2/0_2]_S$.

The SL-layer is placed between play 10 and 11 and consists of two glass-fibre mats (each 30 g/m^2 and 0.1mm dry thickness) to isolate the 16 individual placed piezo ceramic elements. Each individual sensing element has a size of $10\ \text{mm} \times 10\ \text{mm}$ and a thickness of 0.2 mm. Each sensing element is in enclosed within a double-sided polyamide carrier on which the electrode structure is screen-printed. Total thickness of the sensing element with polyamide carrier foils is 0.4 mm. Additionally two thin copper wires are connected on the screen-printed electrodes and peer out of the carrier foils at the other end to realise a soldered connection (see Figure 1a). To connect the sensing elements with the data acquisition system additional soldering terminals are placed at the outer corners of the panels, which are connected with the sensing elements and are further isolated with polyimide adhesive tape (see Figure 1b and c). To ensure the easy accessibility to the soldering terminals after the manufacturing process the top pre-preg layers are cut out beforehand (see Figure 1d and e).

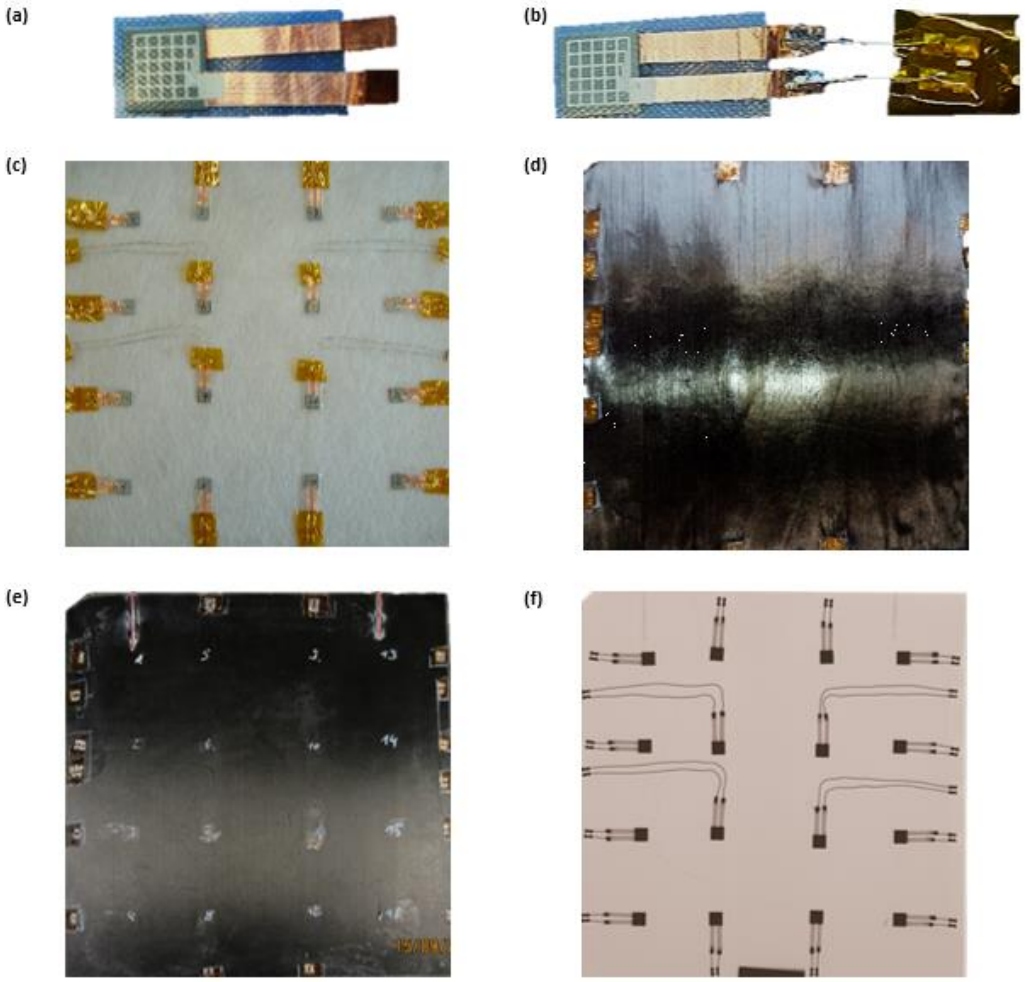

Figure 1. Steps of CFRP panel specimen manufacturing with integrated sensor elements: sensor preparation (a and b); sensor positioning and integration (c); pre-preg stacking (d); consolidated panel specimen (e); computed tomography scan (f).

The CFRP specimen considered for the experimental tests with the spatial coordinates of the used embedded transducers are shown in Figure 2:

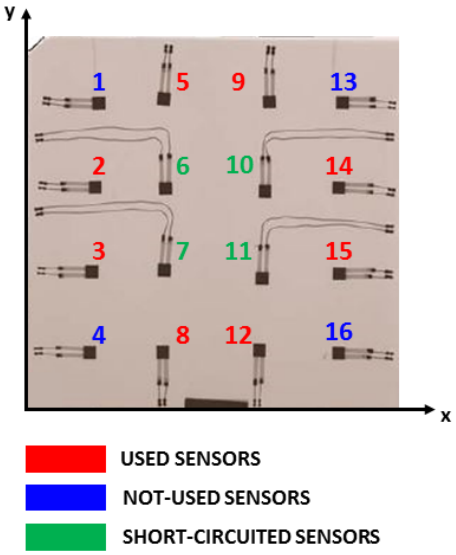

	x-Coordinate (mm)	y-Coordinate (mm)
SENSOR 2	53.7	176.8
SENSOR 3	51.9	109.6
SENSOR 5	107.8	246.1
SENSOR 8	108.7	46.8
SENSOR 9	190.5	244.9
SENSOR 12	185.1	49.2
SENSOR 14	246.7	179.2
SENSOR 15	248.2	111.4

Figure 2. CFRP specimen with embedded sensors and their spatial coordinates.

It should be noted that only eight sensors are used for the tests.

To validate the described algorithms, experimental impact tests were performed by using:

- a hand-held instrumented impact hammer (see Figure 3);
- a small free-drop tower (see Figure 4).

The signals were acquired with a sampling rate of 2 MHz.

Two different sets of experimental tests were performed by using the instrumented impact hammer, the first one on the direction of sensor positions, whose maximum impact force was around 19 N (see Figure 3a), and the second at the centres of the cells identified by four sensors, whose maximum impact force was around 16 N (see Figure 3b).

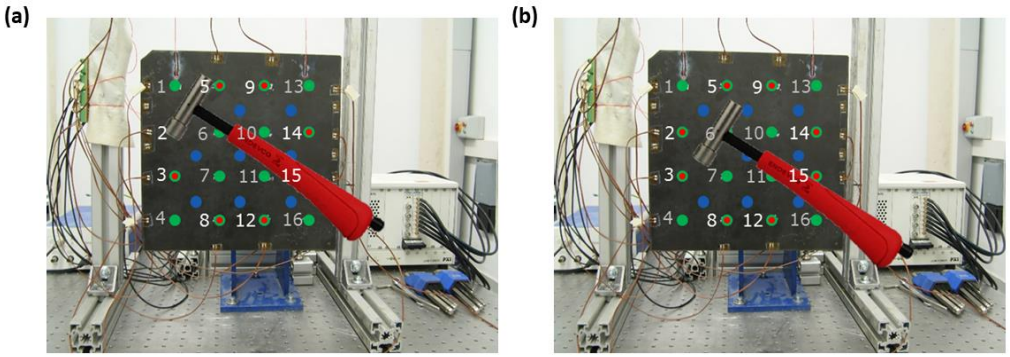

Figure 3. Experimental set-up 1 – Impact tests by instrumented hammer: impacts on the direction of sensor locations (a) and impacts between the sensors (b).

The free-drop tower consists of a steel impactor, whose weight is around 2 kg, arranged with two different heads: a 16 mm wide hemispheric head and a 35 mm cylindrical head (see Figure 4).

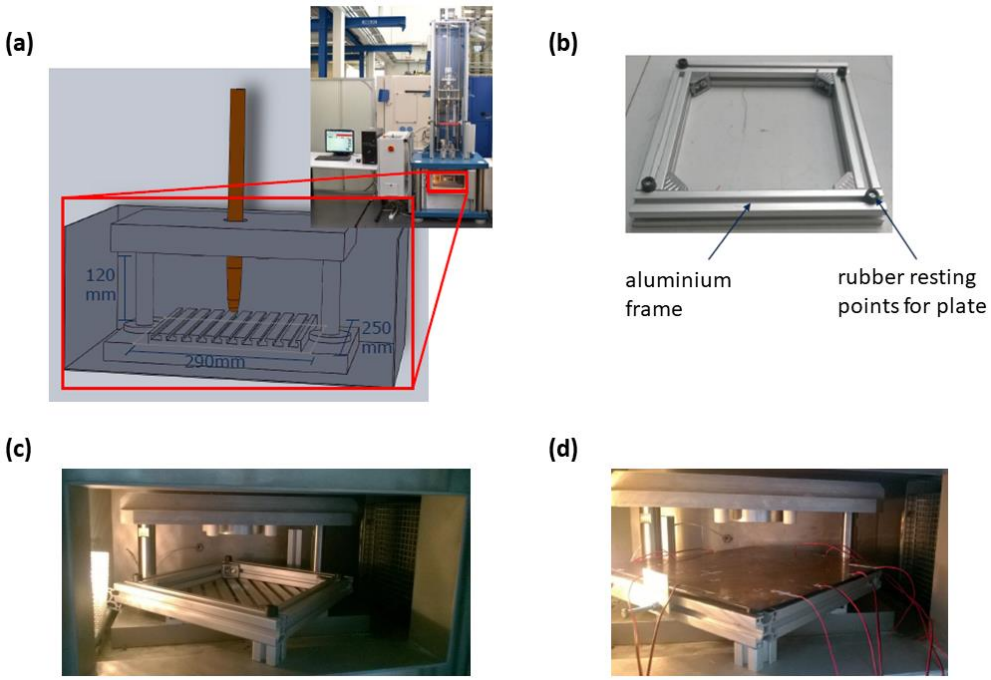

Figure 4. Experimental set-up 2 – Impact tests by free-drop tower: zoom on the testing chamber with dimensions (a); aluminum frame (b); aluminum frame in test chamber (c); aluminum frame with plate specimen in test chamber (d).

Due to limited testing area inside the testing chamber, there was just one way to place the specimen plate, and it is shown in Figure 5:

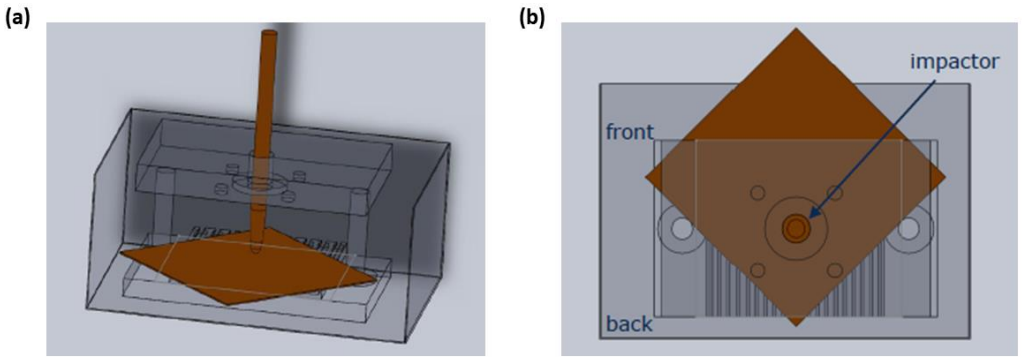

Figure 5. Test specimen located inside the testing chamber of free-drop tower: front view (a) and top view (b).

Multiple impact tests from different heights were performed at a single impact point of the specimen, all depicted in Figure 9, Figure 10 and Table 2. After each impact, an ultrasonic scan of the sample was executed (see Figure 10).

4 RESULTS

The results section is divided into two sub-sections: the first one concerns experimental tests generated by the instrumented hammer, whilst in the second one the impacts are obtained by the drop tower. In both cases, the accuracy of the impact localisation algorithm is expressed by the following formula for the location error Ψ [7]:

$$\Psi = \sqrt{(x_{real} - x_{calculated})^2 + (y_{real} - y_{calculated})^2}\,, \tag{6}$$

where (x_{real}, y_{real}) are the coordinates of the true impact position and $(x_{calculated}, y_{calculated})$ are the coordinates of the calculated impact location. In all the performed experimental tests, the arbitrary set of points discussed in Sections 2.2 and 2.3 consists of 61×61 equally spaced (5 mm) points over the sample surface. For this reason, data coming from $61 \times 61 + 8$ points are considered in Eq. (5) for the calculation of impact coordinates.

4.1 IMPACTS GENERATED BY INSTRUMENTED HAMMER

In Figure 6 and Figure 7, an impact between sensors 2,3,6,7 was considered. It should be noted that sensors 6 and 7 were not used in the experimental tests (see Figure 2). As exposed in Section 2.1, only the initial part of the recorded signals were considered for the power calculation algorithm, indeed Figure 6b depicts some acquired signals due to the described impact event with the chosen time window. The coordinates of the true impact and the calculated one are reported in Table 1 with the location error Ψ.

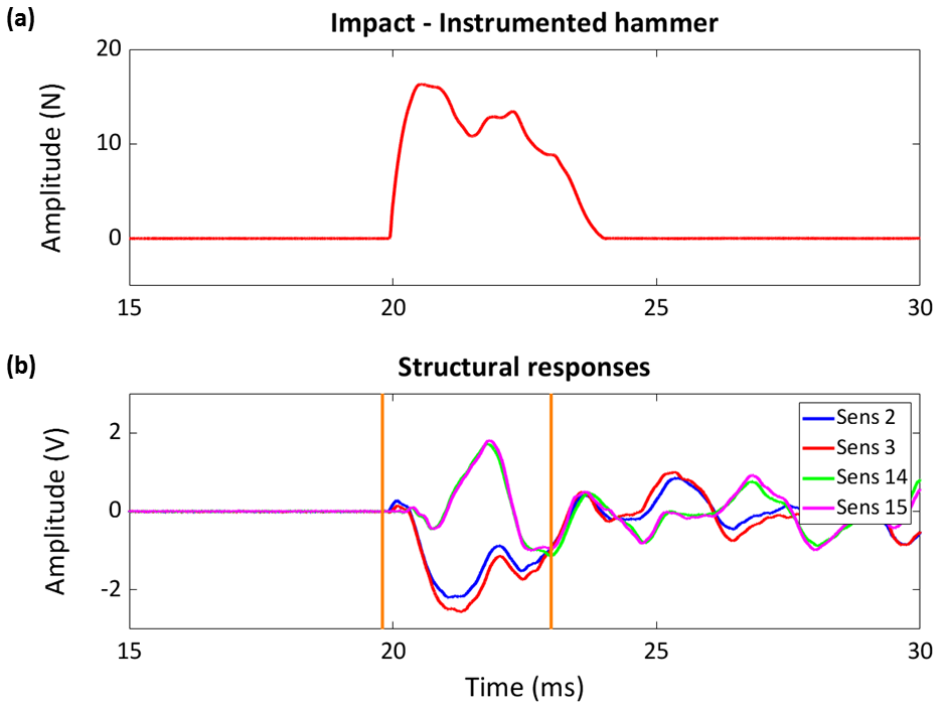

Figure 6. Impact between sensors 2,3,6,7: input signal generated by instrumented impact hammer (a) and structural responses at sensors 2,3,14,15 (b).

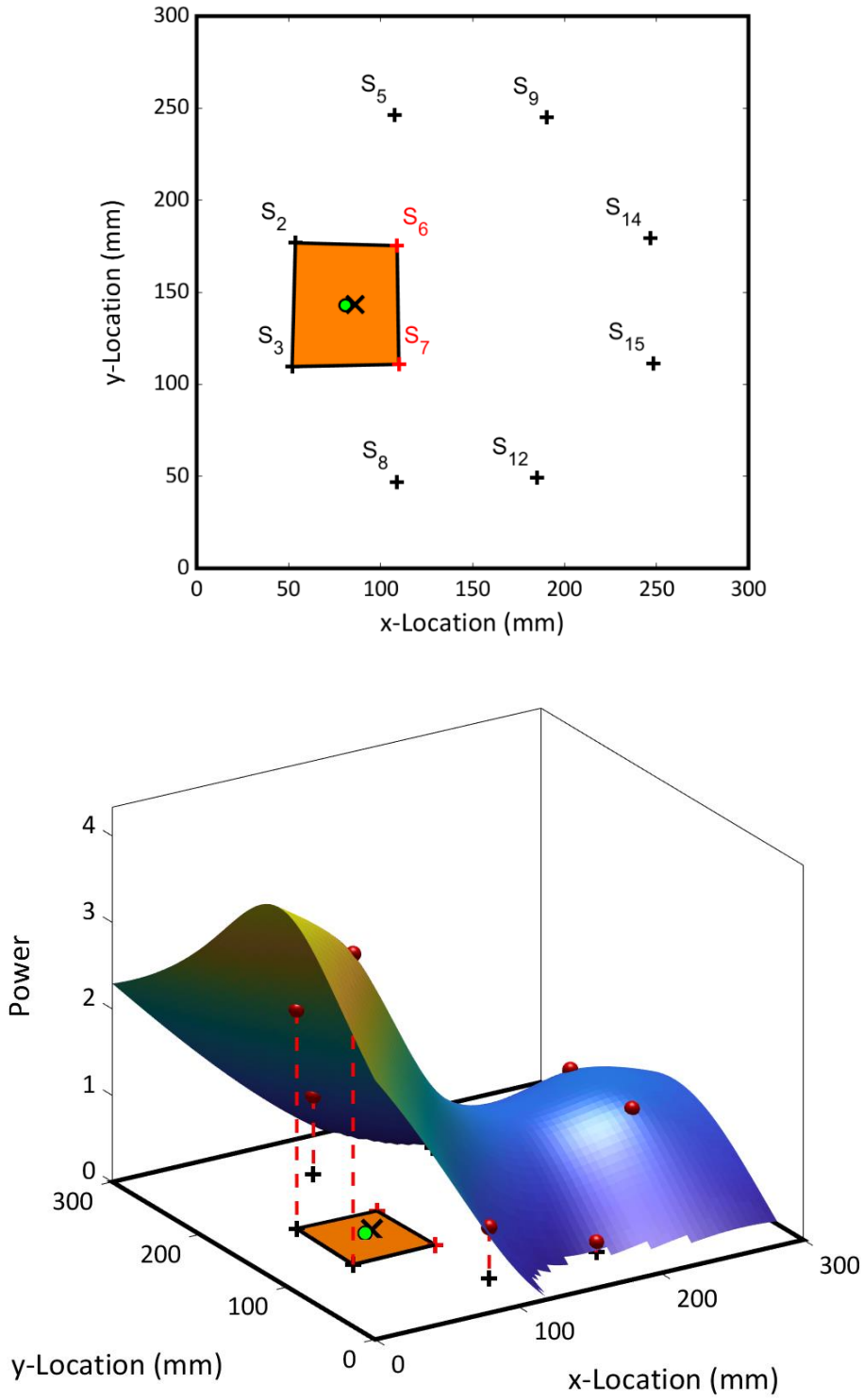

Figure 7. Impact between sensors 2,3,6,7: impact localisation on a 2D plate (top) and representation of the power distribution over the sample obtained by the RBF interpolation method (bottom). The real impact location is shown as a green circle, whilst the calculated one is depicted with a black cross.

Figure 8 and Table 1 show some of the results obtained by using the instrumented impact hammer. In Figure 8 the transducer locations are not reported for clarity. As reported in Table 1, the maximum location error is around 30 mm, therefore the presented method is able to localise the impact event with high accuracy. Furthermore, considering the dependency between the impact localisation results and the considered time window for the recorded signals (see Section 2.1), it should be noted that the obtained results could also be improved with a different choice of time window width.

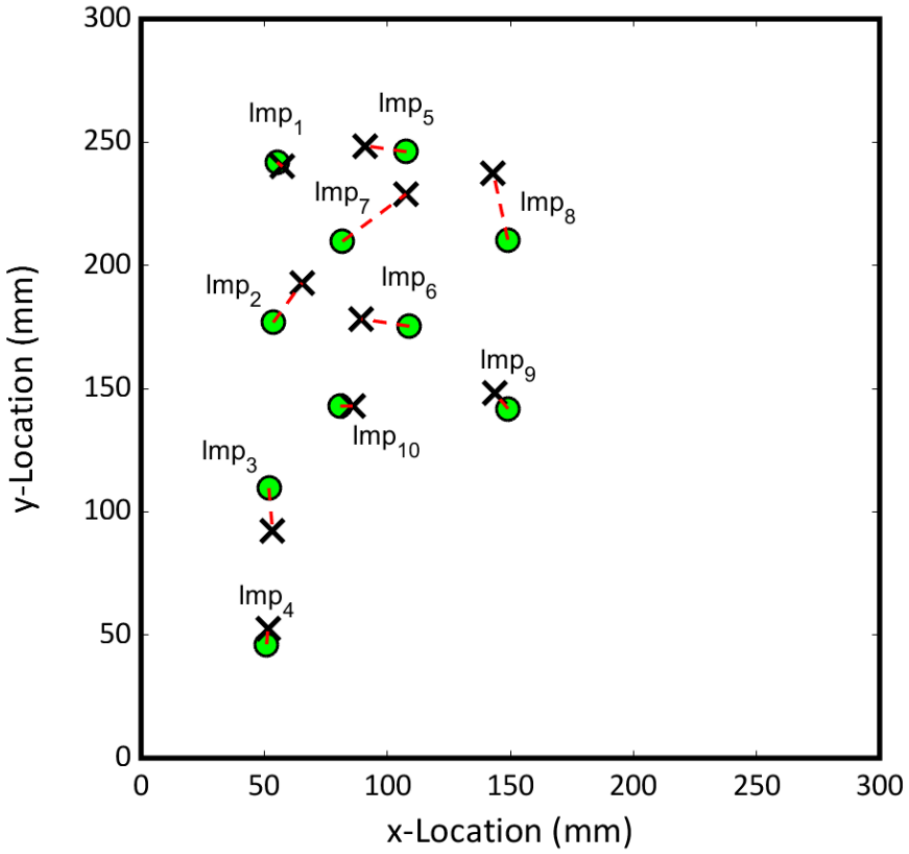

Figure 8. Experimental tests by instrumented hammer: impact localisation results. The real impact locations are shown as a green circle, whilst the calculated ones are depicted with a black cross. The red dotted lines link the true impacts with the calculated ones.

Table 1. Experimental tests by instrumented hammer: impact localisation results.

	x-Coord (mm, real)	y-Coord (mm, real)	x-Coord calc (mm, calc)	y-Coord (mm, calc)	Loc err Ψ (mm)
Impact 1	55.20	241.80	57.49	240.13	2.83
Impact 2	53.70	176.80	65.40	192.96	19.95
Impact 3	51.90	109.60	53.41	92.25	17.41
Impact 4	51	46.20	51.49	52.48	6.30
Impact 5	107.80	246.10	91.05	248.51	16.92
Impact 6	109	175.30	89.48	178.21	19.74
Impact 7	81.81	209.73	107.64	228.94	32.19
Impact 8	148.98	210.39	143.08	237.41	27.65
Impact 9	149.09	141.78	143.77	147.98	8.17
Impact 10	80.93	142.87	86.08	142.87	5.17

4.2 IMPACTS GENERATED BY INSTRUMENTED HAMMER

Figure 9 shows impact results related to a single impact area whose diameter was around 30 mm. Impact test details are reported in Table 2. It should be noted that location error Ψ was calculated considering the centre coordinates of the impact area as the true impact location ($x_{true} = 197.2$ mm, $y_{true} = 101$ mm).

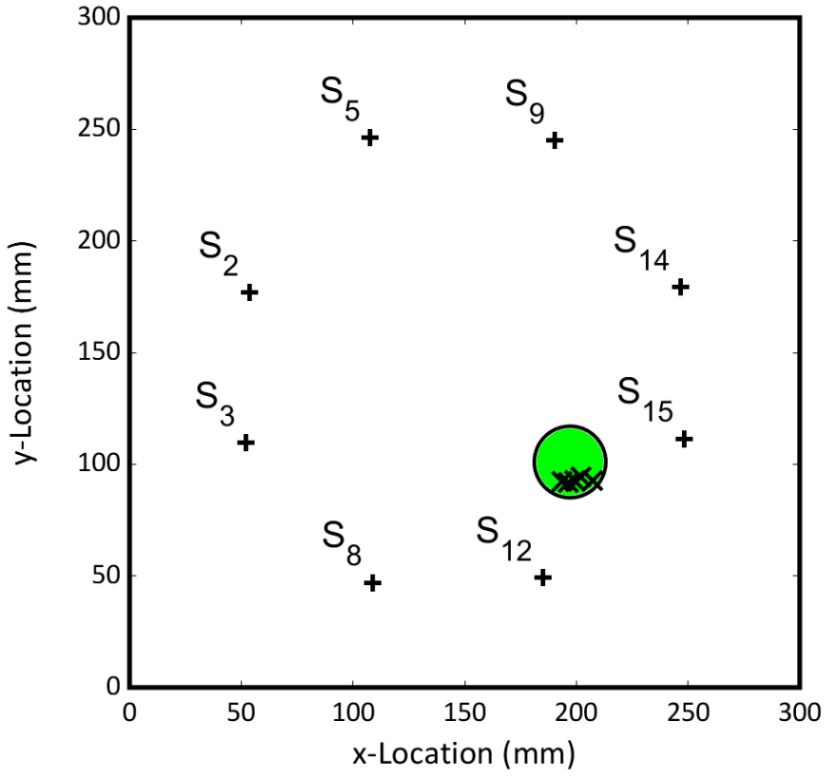

Figure 9. Experimental tests by drop tower: impact localisation results. The real impact area is shown as a green circle, whilst the calculated impacts are depicted with a black cross.

Table 2. Experimental tests by drop tower: impact localisation results.

	Impact Height	Impactor head	x-Coord (mm, calc)	y-Coord calc (mm, calc)	Loc err Ψ (mm)
Impact 1	400	16mm hemisphere	193.43	92.10	9.67
Impact 2	400	16mm hemisphere	199.16	92.79	8.44
Impact 3	400	16mm hemisphere	199.78	92.17	9.20
Impact 4	370	35mm cylinder	207.48	92.72	13.20
Impact 5	500	35mm cylinder	202.24	94.23	8.44
Impact 6	500	35mm cylinder	196.31	91.99	9.05

Also in the case of impact tests performed by using a drop tower, the presented results confirmed the high accuracy of the presented algorithm in the prediction of impact events. Figure 10 shows the ultrasonic scans achieved before the impact tests (reference scan) and after the Impact 6. The impact location depicted in Figure 10b coincides with the centre of the impact area showed in Figure 9.

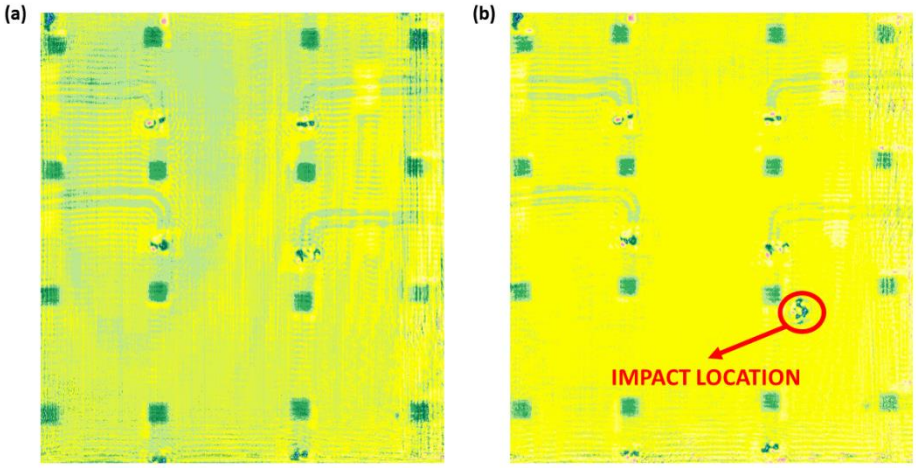

Figure 10. Ultrasonic scans: reference scan before testing (a) and scan after Impact 6 (b).

5 CONCLUSIONS

An impact localisation method suitable for composite specimens arranged with a sparse array of sensors was developed and presented. The proposed algorithm is based on the power values of the first wave packets of the recorded signals due to an impact event. The calculated power values are then interpolated in an arbitrary set of points in order to obtain an improved power distribution over the entire sample. The impact coordinates are calculated by a centre-of-gravity method involving all the power values and their spatial coordinates. Numerous experimental tests were performed on a CFRP plate arranged with embedded transducers, by using both an instrumented impact hammer and a small free-drop tower. The experimental test campaign confirmed the validity of the presented approach, able to estimate the coordinates of the impact event with a negligible impact location error.

ACKNOWLEDGEMENTS

This paper has been funded by the EXTREME project of the European Union's Horizon 2020 research and innovation programme under grant agreement No. 636549.

REFERENCES

1. Tobias, A. (1976). Acoustic-emission source location in two dimensions by an array of three sensors. *Non-destructive testing*, *9*(1), 9-12.
2. Ciampa, F., & Meo, M. (2010). Acoustic emission source localization and velocity determination of the fundamental mode A0 using wavelet analysis and a Newton-based optimization technique. *Smart Materials and Structures*, *19*(4), 045027.
3. Kundu, T., Das, S., & Jata, K. V. (2007). Point of impact prediction in isotropic and anisotropic plates from the acoustic emission data. *The Journal of the Acoustical Society of America*, *122*(4), 2057-2066.
4. Kundu, T., Das, S., Martin, S. A., & Jata, K. V. (2008). Locating point of impact in anisotropic fiber reinforced composite plates. *Ultrasonics*, *48*(3), 193-201.
5. Ciampa, F., & Meo, M. (2010). A new algorithm for acoustic emission localization and flexural group velocity determination in anisotropic structures. *Composites Part A: Applied Science and Manufacturing*, *41*(12), 1777-1786.
6. Ciampa, F., Meo, M., & Barbieri, E. (2012). Impact localization in composite structures of arbitrary cross section. *Structural Health Monitoring*, *11*(6), 643-655.
7. De Simone, M. E., Ciampa, F., Boccardi, S., & Meo, M. (2017). Impact source localisation in aerospace composite structures. *Smart Materials and Structures*, *26*(12).
8. Ciampa, F., & Meo, M. (2012). Impact detection in anisotropic materials using a time reversal approach. *Structural Health Monitoring*, *11*(1), 43-49.
9. Ciampa, F., & Meo, M. (2014). Impact localization on a composite tail rotor blade using an inverse filtering approach. *Journal of Intelligent Material Systems and Structures*, *25*(15), 1950-1958.
10. Ciampa, F., Boccardi, S., & Meo, M. (2016). Factors affecting the imaging of the impact location with inverse filtering and diffuse wave fields. *Journal of Intelligent Material Systems and Structures*, *27*(11), 1523-1533.

11. De Simone, M. E., Ciampa, F., & Meo, M. (2019). A hierarchical method for the impact force reconstruction in composite structures. *Smart Materials and Structures*, *28*(8).

12. De Simone, M. E., Ciampa, F., & Meo, M. (2019). A hierarchical impact force reconstruction method for Aerospace composites. In *Key Engineering Materials* (Vol. 812, pp. 17-24). Trans Tech Publications Ltd.

13. Park, J., Ha, S., & Chang, F. K. (2009). Monitoring impact events using a system-identification method. *AIAA journal*, *47*(9), 2011-2021.

14. Wright, G. B. (2003). Radial basis function interpolation: numerical and analytical developments. University of Colorado, Boulder, Doctoral dissertation.

15. Ciampa, F., Pickering, S. G., Scarselli, G., & Meo, M. (2017). Nonlinear imaging of damage in composite structures using sparse ultrasonic sensor arrays. *Structural Control and Health Monitoring*, *24*(5), e1911.

16. Bookstein, F. L. (1989). Principal warps: Thin-plate splines and the decomposition of deformations. *IEEE Transactions on pattern analysis and machine intelligence*, *11*(6), 567-585.

Chapter 8

Conclusions

The principal aim of the presented thesis was the development of structural health monitoring (SHM) systems for the localisation of acoustic emission source due to low-velocity impact events and for the reconstruction of impact load history in typical aerospace isotropic and composite components.

Nowadays, studies and research on both described topics are necessary for numerous reasons; the principal one is to avoid catastrophic consequences to the vehicle caused by undetected cracks. The application of such SHM systems allows a faster, safer and inexpensive structural check on aircraft and spacecraft, thanks to the inspection of the only potentially dangerous areas, that are the zones where multiple and/or critical impacts occurred during a flight or space mission.

All the research work is based on the development of passive SHM techniques, able to detect the signals emitted by a low-velocity impact event, through an array of piezoelectric transducers fixed on the specimen surface or embedded into the structure.

Three methods deputed to the localisation of an impact event on isotropic and composite structures were analysed, developed and improved in this research work: (i) the linearised algorithm, (ii) the time reversal method, (iii) the signal power method.

Despite the peculiar differences between the developed algorithms, the three approaches are able to determine the location of an impact event, in terms of bidimensional coordinates, with reasonable accuracy, identified by location error values variable from 1-2 mm for the time reversal method to 30 mm for the signal power method.

Obviously, it is fundamental to recognise the cases where a method is more suitable than another. Indeed, the signal power method was developed for the localisation of an impact event on a composite specimen arranged with a set of far from each other integrated ceramic piezo sensors, without the knowledge of the mechanical properties of the material, neither a baseline obtained by a calibration process.

Differently to the described situation, the use of a particular configuration of four surface-bonded piezoelectric transducers, arranged very close to each other, was the starting point for the linearised impact localisation algorithm, whose fundamental hypothesis consisted of the same wave velocity, due to an impact event, experienced by the sensors. The necessary accuracy of the order of microseconds in calculation of time of arrival of recorded signals was obtained by using Akaike Information Criterion (AIC) pickers.

The time reversal method represents a well-known approach, used in this research work for the calibration process performed as first step. Indeed, information related not only to structural responses but also to impact histories can be used to calculate the transfer functions in frequency domain at calibration points. These functions are then interpolated by using the radial basis functions (RBFs), in order to calculate the unknown transfer function and impact time history at the impact point, whose location was previously determined by time reversal method with a maximum location error less than 2-3 mm.

As anticipated, the second main topic of this research work, consisting of the reconstruction of the impact load history, was achieved by using RBF interpolation approach, whose results were compared with a shape function (SF) method. The method developed by the author was able to reconstruct the actual impact force with an error less than the error related to the shape function method.

In order to validate the proposed methodologies, a number of experimental impact tests were performed on isotropic and composite aerospace structures (e.g. plates and complex wing stringer-skin panels), arranged with different configuration of surface-bonded or embedded piezoelectric transducers detecting low-velocity impacts performed by a hand-held instrumented impact hammer and a small free-drop tower.

The results showed the accuracy, reliability and robustness of the developed methods, confirmed by the error functions that demonstrated the negligible differences between the actual impact conditions and the calculated ones.

Furthermore, a proof of concept for a space debris detector involving some of the described algorithms was proposed. The presented detector, named SCODD ("Smart Composite Orbital Debris Detector"), consists of two thin parallel carbon fibre reinforced plastic (CFRP) composite plates, each instrumented with three piezoelectric transducers embedded into the laminate. The developed algorithm was able to estimate both directions and velocities of a low-velocity "object", as demonstrated by the results obtained by using a free-drop impactor in the experimental campaign. The results demonstrated the effectiveness of the proposed detection system for future Earth satellites, especially in monitoring of orbital debris and micrometeoroids particles.

8.1 Future Works

The presented thesis work exposed several methods and algorithms that achieved accurate results in impact localisation and force reconstruction in isotropic and composite structures. The next step could be to continue the verification and validation of the used approaches on different and complex aerospace structures, considering also the presence of damage and strong geometric nonlinear effects. For example, it was shown the effectiveness of the developed impact force reconstruction method, also when small nonlinear effects are present. However, it could be very interesting to understand if and how the presence of a damage,

generated by the impact, could affect the validity of the approach. Certainly, the finite element (FE) analysis would be extremely helpful in the testing process.
This further experimental campaign would allow the creation of SHM devices suitable for industries and acting in real time on full-scale, operational aircraft and spacecraft. An idea could be to integrate all the system in a single embedded device, able to collect and process the data coming from the transducers located on the structure surface or embedded into it. With regards to the smart composite orbital debris detector, it is necessary to continue the experimental tests considering hypervelocity impacts (HVIs), in order to validate the developed method with impact energies similar to what occur in a real space environment.

8.2 PhD Activities

During the PhD programme a number of scientific papers has been published in international peer-reviewed journals and a number of oral sessions has been presented at international conferences.

Peer-reviewed Journals (published order):

1. De Simone, M. E., Ciampa, F., Boccardi, S., & Meo, M. (2017). Impact source localisation in aerospace composite structures. *Smart Materials and Structures*, *26*(12).

2. De Simone M. E., Andreades, C., Mohamad Hilmi, M. H., Meo, M., & Ciampa, F. (2019). Proof of concept for a smart composite orbital debris detector. *Acta Astronautica*, *160*, 499-508.

3. De Simone, M. E., Ciampa, F., & Meo, M. (2019). A hierarchical method for the impact force reconstruction in composite structures. *Smart Materials and Structures*, *28*(8).

Conference Papers (published order):

1. De Simone, M. E., Boccardi, S., Ciampa, F., & Meo, M. (2016). A linearised impact localisation algorithm for the health monitoring of aerospace components. In *8th European Workshop on Structural Health Monitoring, EWSHM 2016* (pp. 1773-1782). NDT. net.

2. De Simone, M. E., Ciampa, F., & Meo, M. (2017). A structural health monitoring technique for the reconstruction of impact forces in aerospace components. In *11th International Workshop on Structural Health Monitoring 2017: Real-Time Material State Awareness and Data-Driven Safety Assurance, IWSHM 2017: Real-Time Material State Awareness and Data-Driven Safety Assurance* (pp. 2154-2161). DEStech Publications.

3. De Simone, M. E., Cuomo, S., Ciampa, F., Meo, M., Nitschke, S., Hornig, A., & Modler, N. (2019, April). *Acoustic emission localisation in composites using the signal power method and embedded transducers. In Nondestructive Characterization and Monitoring of Advanced Materials, Aerospace, Civil Infrastructure, and Transportation XIII* (Vol. 10971, p. 109711O). International Society for Optics and Photonics.

4. De Simone, M. E., Ciampa, F., & Meo, M. (2019). A hierarchical impact force reconstruction method for Aerospace composites. In *Key Engineering Materials* (Vol. 812, pp. 17-24). Trans Tech Publications Ltd.

5. De Simone, M. E., Andreades, C., Meo, M., & Ciampa, F. (2019). Smart composite detector of orbital debris and micrometeoroids particles. *Materials Today: Proceedings* (Accepted manuscript).

6. Cuomo, S., De Simone, M. E., Andreades, C., Ciampa, F., & Meo, M. (2019). Machine learning for impact detection on composite structures. *Materials Today: Proceedings* (Accepted manuscript).

International Conferences (speaker, chronological order):

1. 8th European Workshop on Structural Health Monitoring, EWSHM 2016.

   July 5-8, 2016, Bilbao, Spain.

2. 11th International Workshop on Structural Health Monitoring 2017: Real-Time Material State Awareness and Data-Driven Safety Assurance, IWSH 2017.

   September 12-14, 2017, Stanford University, Stanford, USA.

3. 1st International Workshop on Dynamic Response of Composite Materials, IWDRC 2017.

   September 27-28, 2017, Taormina, Italy.

4. 1st World Conference on Advanced Materials for Defense, AuxDefense 2018.

   September 3-4, 2018, Lisbon, Portugal.

5. 12th International Conference on Composite Science and Technology, ICCST 2019

   May 8-10, 2019, Sorrento, Italy.

Moreover, several technical meetings on Structural Health Monitoring systems for impact localisation and impact force reconstruction with Airbus personnel at the University of Bath and in Bristol has been attended.

The research work I conducted during PhD period has been funded by the EXTREME project of the European Union's Horizon 2020 research and innovation programme under grant agreement No. 636549.

References

1. Balageas, D., Fritzen, C. P., & Güemes, A. (Eds.). (2010). *Structural health monitoring* (Vol. 90). John Wiley & Sons.
2. Nicolais, L., Meo, M., & Milella, E. (Eds.). (2011). *Composite materials: a vision for the future*. Springer Science & Business Media.
3. Ciampa, F. (2012). *Structural health monitoring systems for impacted isotropic and anisotropic structures* (Doctoral dissertation, University of Bath).
4. MATLAB (2018), ver. R2018b, MathWorks.
5. Kundu, T. (2014). Acoustic source localization. *Ultrasonics*, *54*(1), 25-38.
6. Tobias, A. (1976). Acoustic-emission source location in two dimensions by an array of three sensors. *Non-destructive testing*, *9*(1), 9-12.
7. McLaskey, G. C., Glaser, S. D., & Grosse, C. U. (2010). Beamforming array techniques for acoustic emission monitoring of large concrete structures. *Journal of Sound and Vibration*, *329*(12), 2384-2394.
8. He, T., Pan, Q., Liu, Y., Liu, X., & Hu, D. (2012). Near-field beamforming analysis for acoustic emission source localization. *Ultrasonics*, *52*(5), 587-592.

9. Liang, D., Yuan, S. F., & Liu, M. L. (2013). Distributed coordination algorithm for impact location of preciseness and real-time on composite structures. *Measurement*, *46*(1), 527-536.

10. Kundu, T., Das, S., & Jata, K. V. (2007). Point of impact prediction in isotropic and anisotropic plates from the acoustic emission data. *The Journal of the Acoustical Society of America*, *122*(4), 2057-2066.

11. Kundu, T., Das, S., Martin, S. A., & Jata, K. V. (2008). Locating point of impact in anisotropic fiber reinforced composite plates. *Ultrasonics*, *48*(3), 193-201.

12. Meo, M., Zumpano, G., Piggott, M., & Marengo, G. (2005). Impact identification on a sandwich plate from wave propagation responses. *Composite structures*, *71*(3-4), 302-306.

13. Salehian, A. (2003). Identifying the location of a sudden damage in composite laminates using wavelet approach. MSc thesis. Worcester Polytechnic Institute, 2003.

14. Kundu, T. (2012, July). A new technique for acoustic source localization in an anisotropic plate without knowing its material properties. In *6th European Workshop on Structural Health Monitoring* (pp. 3-6).

15. Kundu, T., Nakatani, H., & Takeda, N. (2012). Acoustic source localization in anisotropic plates. *Ultrasonics*, *52*(6), 740-746.

16. Ciampa, F., & Meo, M. (2010). Acoustic emission source localization and velocity determination of the fundamental mode A_0 using wavelet analysis and a Newton-based optimization technique. *Smart Materials and Structures*, *19*(4), 045027.

17. Ciampa, F., & Meo, M. (2010). A new algorithm for acoustic emission localization and flexural group velocity determination in anisotropic structures. *Composites Part A: Applied Science and Manufacturing*, *41*(12), 1777-1786.

18. Ciampa, F., Meo, M., & Barbieri, E. (2012). Impact localization in composite structures of arbitrary cross section. *Structural Health Monitoring*, *11*(6), 643-655.

19. Ziola, S. M., & Gorman, M. R. (1991). Source location in thin plates using cross-correlation. *The Journal of the Acoustical Society of America*, *90*(5), 2551-2556.

20. Kosel, T., Grabec, I., & Kosel, F. (2003). Intelligent location of simultaneously active acoustic emission sources: Part I. *Aircraft Engineering and Aerospace Technology*, *75*(1), 11-17.

21. Ciampa, F., & Meo, M. (2012). Impact detection in anisotropic materials using a time reversal approach. *Structural Health Monitoring*, *11*(1), 43-49.

22. Ciampa, F., & Meo, M. (2014). Impact localization on a composite tail rotor blade using an inverse filtering approach. *Journal of Intelligent Material Systems and Structures*, *25*(15), 1950-1958.

23. Ciampa, F., Boccardi, S., & Meo, M. (2016). Factors affecting the imaging of the impact location with inverse filtering and diffuse wave fields. *Journal of Intelligent Material Systems and Structures*, *27*(11), 1523-1533.

24. Tong, C., & Kennett, B. L. (1996). Automatic seismic event recognition and later phase identification for broadband seismograms. *Bulletin of the Seismological Society of America*, *86*(6), 1896-1909.

25. Mallat, S. (1999). *A wavelet tour of signal processing*. Elsevier.

26. Teolis, A., & Benedetto, J. J. (1998). *Computational signal processing with wavelets* (Vol. 182). Boston, MA, USA: Birkhäuser.

27. Titchmarsh, E. C. (1948). *Introduction to the theory of Fourier integrals* (Vol. 950, p. 8). Oxford: Clarendon Press.

28. King, F. W. (2009). *Hilbert transforms* (Vol. 2). Cambridge: Cambridge University Press.

29. Ulrich, T. J. (2006). Envelope calculation from the Hilbert transform. *Los Alamos Nat. Lab., Los Alamos, NM, USA, Tech. Rep*.

30. Sedlak, P., Hirose, Y., Khan, S. A., Enoki, M., & Sikula, J. (2009). New automatic localization technique of acoustic emission signals in thin metal plates. *Ultrasonics*, *49*(2), 254-262.

31. Allen, R. (1982). Automatic phase pickers: Their present use and future prospects. *Bulletin of the Seismological Society of America*, *72*(6B), S225-S242.

32. Wright, G. B. (2003). *Radial basis function interpolation: numerical and analytical developments*. (Doctoral dissertation, University of Colorado, Boulder).